

**School of Science
Department of Imaging and Applied Physics
Centre for Marine Science and Technology**

**Modelling of Underwater Acoustic Propagation over Elastic,
Range-Dependent Seabeds**

Matthew Walter Koessler

**This thesis is presented for the Degree of
Doctor of Philosophy
of
Curtin University**

March 2016

DECLARATION

To the best of my knowledge and belief this thesis contains no material previously published by any other person except where due acknowledgment has been made.

This thesis contains no material which has been accepted for the award of any other degree or diploma in any university.

Matthew Koessler

Date: 21/03/2016

ABSTRACT

The seabed found in the offshore environment around Australia are characterised by cemented and/or semi-cemented calcarenite with very little unconsolidated overburden. For underwater acoustic propagation modelling, calcarenite is considered to be solid rock and is treated as an elastic material because of this cementation. In the seabed, the occurrence of alternating thin and thick calcarenite layers can significantly affect underwater sound propagation. Until recently the combination of modelling range dependent bathymetric variations with a layered seabed of calcarenite has proved to be difficult. Recent research has shown that it is possible to obtain accurate results for these types of range dependent environments using a new parabolic equation method. However, accurate results are obtained at the expense of long computational runtimes. This thesis aims to determine if an alternate propagation modelling approach based on adiabatic seismoacoustic (acousto-elastic) normal modes is suitable for modelling range dependent propagation over thin and thick layers of calcarenite. The goal is to produce an accurate and efficient alternative modelling method.

A propagation model based on adiabatic seismoacoustic normal modes with ORCA (SANMO) was derived from a coupled mode theory that was initially developed for seismic interface wave modelling. An elastic wedge was used as a formal benchmark to test SANMO's applicability to range dependent propagation over an elastic bottom. The benchmarking exercise consisted of comparing the output from SANMO to two other seismoacoustic parabolic equation models, RAMSGEO and LAYROTVARS, for the wedge environment. Different treatments of the elastic bottom were considered including a halfspace, an elastic false bottom, and an attenuating Airy halfspace with gradients in the compressional and shear attenuation coefficients. The adiabatic mode model was able to produce consistent results for the sound field in the water column with the use of a standard halfspace and an attenuating Airy halfspace representation of the elastic bottom.

Using LAYROTVARS and SANMO, the transmission loss of signals from a seismic source were modelled considering propagation over a layered calcarenite seafloor with range dependent bathymetry. A broad band of low frequencies from 2 Hz to

100 Hz was considered. For one scenario, the total required time for LAYROTVARS was up to 7 days to perform the calculations accurately. When SANMO was used, accurate results could also be achieved; however, for the same scenario the required calculations took only 2.5 hours to complete.

The modelling results were then compared to previously un-analysed measurements. The measurements consisted of signals from a nearby seismic survey recorded on an autonomous seafloor recorder in Bass Strait Australia. A modelled source spectrum was then combined with the transmission loss results to calculate the synthetic sound exposure levels. These synthetic sound exposure levels were then compared to the sound exposure levels computed from recorded signals. The comparison between measured and synthetic sound exposure levels was initially inconsistent. However, upon increasing the shear wave speed in the elastic bottom and re-modelling the transmission loss a better fit was achieved.

The practical importance of this work is the computational efficiency of SANMO balanced with the required accuracy for practical modelling scenarios. Compared to LAYROTVARS, differences between the propagation models of a few dB could be achieved for the considered environments. However, the multi-day run-time of LAYROTVARS compared to multi-hour runtime of SANMO suggests that SANMO is better suited for practical use.

I. CONTENTS

DECLARATION	III
ABSTRACT	V
I. CONTENTS	VII
II. List of Figures	XI
III. List of Tables	XVII
IV. Acknowledgements	XIX
V. Symbols and Abbreviations	XXI
CHAPTER 1 Introduction	1
1.1 Motivation	1
1.2 Introduction to Underwater Acoustic Propagation Modelling	1
1.2.1 Numerical Approaches for Handling Range Dependence with Elastic Bottoms	3
1.3 Propagation Modelling Applied to Australia's Continental Shelf Environment	5
1.4 Thesis Organisation	7
CHAPTER 2 Acoustic and Elastic Wave Propagation Theory	9
2.1 Governing Equations for Acoustic Waves	9
2.2 Governing Equation for Elastic Waves	10
2.3 Normal Modes of the Shallow Water Ocean Waveguide	12
2.3.1 The Elastic Pekeris Waveguide	18
2.4 Summary Remarks	20
CHAPTER 3 Acoustic Propagation over Australian Seafloors	23
3.1 Introduction	23
3.2 Australian Continental Shelf Regional Geology	23
3.3 Geoacoustic models for a Calcarenite Seafloor	25
3.4 Sound Reflection from Calcareous Seafloors	27
3.5 Sea Bottom Effect on the Propagation of Normal Modes	32
3.6 Summary	40

CHAPTER 4 Seismoacoustic Adiabatic Normal Modes	43
4.1 Introduction	43
4.2 Normal Modes for Environments with Elastic Bottoms	43
4.2.1 Description of the Seismoacoustic Adiabatic Normal Mode Algorithm	46
4.3 Numerical Examples of Single Frequency Benchmarks	47
4.3.1 Acoustical Society of America's (ASA) Elastic Wedge	47
4.3.2 Range Independent Benchmarking Results (FLAT)	48
4.3.3 Range Dependent Benchmarking Results (UP)	56
4.3.4 Range Dependent Benchmarking Results (DOWN)	63
4.4 Discussion: Different Elastic Bottom Representations	65
4.5 Summary	70
CHAPTER 5 Numerical Modelling of Bass Strait Data	73
5.1 Modelling of Broadband Low Frequency Propagation over a Range Dependent Layered Elastic Seabed	73
5.1.1 Range Dependent Broadband Low Frequency Propagation over Layered Elastic Seabeds with Gradually Varying Bathymetry	77
5.1.2 Range Dependent Broadband Low Frequency Propagation over Layered Elastic Seabeds with Rapidly Varying Bathymetry	84
5.1.3 Influence of Mode Coupling on the Water Column Acoustic Field	88
5.1.4 Computational Cost	95
5.2 Model Predictions and Measured Data Comparison	97
5.2.1 Calculation of the Sound Exposure Level	99
5.3 Discussion: An Assessment of the Modelling Methods for Propagation over a Range Dependent Layered Elastic Seabed	108
5.4 Summary	109
5.4.1 Numerical Results	109
5.4.2 SEL Measurements and Simulated SEL	110
CHAPTER 6 Conclusions and Further Research Avenues	111
6.1 Conclusions	111
6.1.1 Seismoacoustic Adiabatic Normal Modes in the Elastic Wedge Environment	111
6.1.2 Modelling Range Dependent Propagation over Layered Elastic Seafloors	111
6.2 Future Research Opportunities	113

References	115
Appendix A Functional Form of the Adiabatic Approximation	125
Appendix B Acoustic Single-Scatter Mode Coupling Algorithm	129

X

II. List of Figures

Figure 2.1: A diagram of a generalised ocean acoustic waveguide. The depths z_s , h , and H denote the source depth, depth of the seafloor, and the top of the bottom halfspace respectively. The SSP denotes the continuously varying Sound Speed Profile (SSP) in the water column.....	13
Figure 2.2: A Schematic representation of contour integration in the complex plane when the Pekeris cut is used. The black dots represent the location of the poles of the Green's function.....	15
Figure 2.3: A schematic representation of the ocean acoustic waveguide showing the reflection geometry that produces acoustic propagation as normal modes.....	17
Figure 3.1. Approximate geographical extent of calcarenite seafloors defined from studies investigating Australian seafloor geology and the shallow water acoustic propagation characteristics.....	24
Figure 3.2: From the geotechnical report commissioned by Fugro (2004) showing the piezocone penetrometer profile to a maximum depth of 100 m below the seafloor. <i>Left Panel:</i> A plot the net resistance from a piston piezocone test. <i>Right Panel:</i> Tabulated values of net resistance and a lithology description from Fugro (2004).	27
Figure 3.3: Comparison of plane wave reflection coefficients from calcarenite and sand bottoms where θ refers to the grazing angle. The geoacoustic parameters used to represent the bottom are given in Table 3.1.	28
Figure 3.4: Plane wave reflection coefficient magnitude for the scenarios presented in Table 3.2. The black curve in the top panel corresponds to the halfspace scenario which does not depend on frequency; the other colour curves corresponds to the frequencies: 10 Hz – blue, 20 Hz – green, 50 Hz – red, 100 Hz – cyan, 200 Hz – magenta, and 500 Hz – orange. (A) Calcareous Bottom (B) Thin Cap-rock Layer – Calcareous Bottom (C) Thin Sand Layer – Calcareous Bottom (D) Calcareous Bottom – Sedimentary Basement.....	31
Figure 3.5: The magnitude (<i>Top Panel</i>) and phase (<i>Bottom Panel</i>) of the reflection coefficient and locations of modal components from Equation (11) and Equation (12), the modal components move from right to left as the frequency increases from 20 Hz to 30 Hz. Each mode is colour coded, blue – mode 1, green – mode 2, red – mode three, and cyan – mode four.....	35
Figure 3.6: Wavenumber trajectories in the complex plane from 1 Hz to 100 Hz for the first 5 modes; low attenuating mods are found near the critical frequencies (indicated by vertical solid black lines) of the waveguide. Each mode is colour coded, blue – mode 1, green – mode 2, red – mode three, cyan – mode four, and magenta mode – five.....	37
Figure 3.7: Figures excerpt from Fan et al. (2009) that show low frequency broadband transmission loss. The low loss peaks are seen near the critical frequencies in both experimental data (<i>left</i>) and model predictions (<i>right</i>).	38

Figure 4.1: Transmission loss (TL) at a depth of 30 metres for the flat bottom waveguide (FLAT) validation scenario predicted using propagation models OASES as benchmarks for SANMO	49
Figure 4.2: Transmission loss comparison between OASES and SANMO at receiver depth of 230 metres. The panels starting from the top shows the transmission loss from vertical and horizontal particle velocities and vertical and horizontal normal seismic stresses.....	51
Figure 4.3: The real (<i>Left Panel</i>) and imaginary (<i>Right Panel</i>) parts of the mode function for mode 4.....	52
Figure 4.4: A schematic for the false bottom configuration used by all the propagation models for the FLAT case.	53
Figure 4.5: <i>Top Panel</i> : Transmission loss at a depth of 30 metres for the flat bottom waveguide (FLAT) validation scenario predicted using propagation models, OASES as benchmarks for LAYROTVARS, RAMSGEO, and SANMO. <i>Bottom Panel</i> : Transmission loss at a depth of 230 metres for the flat bottom waveguide (FLAT) validation scenario.	54
Figure 4.6: Cross-section of TL for the FLAT case with a false bottom.	55
Figure 4.7: Cross-sections of TL for the FLAT case with a halfspace representation of the seabed.....	56
Figure 4.8: (<i>Top Panel</i>) Transmission loss slice at a receiver depth of 30 metres for the upslope (UP) validation scenario with a false bottom using propagation models LAYROTVARS and RAMSGEO as benchmarks for SANMO. (<i>Bottom Panel</i>) Difference between SANMO and LAYROTVARS (red curve) and SANMO and RAMSGEO (magenta curve) at a receiver depth of 30 metres as a function of range from the source.	58
Figure 4.9: Cross-section of TL for the UP case with a false bottom.	59
Figure 4.10: A schematic for the attenuating Airy halfspace configuration used by SANMO.	60
Figure 4.11: (<i>Top Panel</i>) Transmission loss slice at a receiver depth of 30 metres for the upslope (UP) validation scenario with an attenuating Airy halfspace using propagation models LAYROTVARS and RAMSGEO as benchmarks for SANMO. (<i>Bottom Panel</i>) Difference between SANMO and LAYROTVARS (red curve) and SANMO and RAMSGEO (magenta curve) at a receiver depth of 30 metres as a function of range from the source.	62
Figure 4.12: Cross-sections of TL for the UP case showing PE results (<i>Top Panels</i>), SANMO's results with standard halfspace representation of the bottom (<i>Bottom Left Panel</i>), and SANMO's results with an attenuating Airy halfspace (<i>Bottom Right Panel</i>).	63

Figure 4.13: (<i>Top Panel</i>) Transmission loss slice at a receiver depth of 30 metres for the downslope (DOWN) validation scenario with an attenuating Airy halfspace using propagation models LAYROTVARS and RAMSGEO as benchmarks for SANMO. (<i>Bottom Panel</i>) Difference between SANMO and LAYROTVARS (red curve) and SANMO and RAMSGEO (magenta curve) at a receiver depth of 30 metres as a function of range from the source	64
Figure 4.14: Cross-sections of TL for the DOWN case with an attenuating Airy halfspace	65
Figure 4.15: The real part of the mode function for a halfspace bottom (blue), false bottom (red), and attenuating Airy halfspace (green). (<i>Left Panel</i>) The real part of mode 2. (<i>Right Panel</i>) The real part of mode 3	66
Figure 4.16: Transmission loss cross-sections for upslope propagation with a fluid seabed. <i>Top Panel</i> : Adiabatic modes with a fluid halfspace bottom. <i>Middle Panel</i> : Adiabatic modes with a false bottom. <i>Bottom Panel</i> : Coupled modes with a false bottom.....	68
Figure 4.17: Transmission loss cross-sections for downslope propagation with a fluid seabed. <i>Top Panel</i> : Adiabatic modes with a fluid halfspace bottom. <i>Middle Panel</i> : Adiabatic modes with a false bottom. <i>Bottom Panel</i> : Coupled modes with a false bottom.....	69
Figure 5.1: <i>Top Panel</i> : A topography and bathymetry of Australia in which the study region in western Bass Strait is indicated by the red square (Whiteway, 2009). <i>Bottom Panel</i> : The approximate locations of the 100 m geotechnical borehole and locations of autonomous underwater sound recorders in relation to the two seismic surveys discussed in this chapter; Survey 1 corresponds to the results of (Duncan et al., 2013) and Survey 2 corresponds to an earlier survey	75
Figure 5.2: Water column sounds speed profile for modelling Bass Strait range dependent scenarios from Duncan et al. (2013)	77
Figure 5.3: Bathymetry profiles from Geoscience Australia (Whiteway, 2009) for Bathymetry 1 and Bathymetry 2	78
Figure 5.4: Comparison of the transmission loss versus frequency predicted by SANMO and LAYROTVARS at a depth of 7 m and range of 40 km for Bathymetry 1	79
Figure 5.5: A comparison plot from SANMO (bottom panel) and LAYROTVARS (top panel) showing a broadband transmission loss cross-section at a source depth of 7 m and a source-to-receiver range of 40 km for Bathymetry 1	80
Figure 5.6: Modal attenuation coefficient for Bathymetry 1, Mode 1 – 5 at a frequency of 23 Hz	81
Figure 5.7: Comparison of the transmission loss versus frequency predicted by SANMO and LAYROTVARS at a depth of 7 m and range of 40 km for Bathymetry 2	82

Figure 5.8: Single frequency transmission loss slices for Bathymetry 2, showing transmission loss range slices at a depth of 7 metres and 30 metres (<i>top left</i> and <i>top right</i>) at a frequency of 21 Hz, Depth slices at ranges of 20 and 59 kilometres (<i>bottom left</i>), and an additional range slice at a depth of 30 metres at a frequency of 75 Hz. The brown lines in the <i>bottom left</i> panels represent the seafloor interface.....	83
Figure 5.9: Bathymetry profiles from Geoscience Australia (Whiteway, 2009) for Bathymetries 3 to 5.....	84
Figure 5.10: <i>Left Panels</i> : Broadband transmission loss slices for Bathymetries 3 – 5 (<i>top – bottom</i>) at a receiver depth of 6 m. <i>Right Panels</i> : Broadband transmission loss slices for Bathymetries 3 – 5 (<i>top – bottom</i>) at a receiver depth of 75 m. The transmission loss are plotted at a receiver range of 20 km for all the plots.....	85
Figure 5.11: Single frequency transmission loss slices for Bathymetry 5. <i>Left Panels</i> : LAYROTVARS (<i>top</i>) and SANMO (<i>bottom</i>) at a frequency of 21 Hz. <i>Right Panels</i> : LAYROTVARS (<i>top</i>) and SANMO (<i>bottom</i>) at a frequency of 75 Hz.	86
Figure 5.12: Single frequency transmission loss slices for Bathymetry 5 showing transmission loss range slices at a depth of 6 m and 30 m (<i>top left</i> and <i>top right</i>) at a frequency of 21 Hz. Depth slices at ranges of 11 km and 23 km (<i>bottom left</i>), and an additional range slice at a depth of 30 m at a frequency of 75 Hz. The brown lines in the <i>bottom left</i> panels represent the seafloor.....	87
Figure 5.13: <i>Top Panel</i> : Transmission loss cross-section at 21 Hz for Bathymetry 5 from LAYROTVARS. <i>Bottom Panel</i> : same from acoustic coupled modes and ORCA.....	91
Figure 5.14: <i>Left Panel</i> : Transmission loss plot at 21 Hz for Bathymetry 5 from LAYROTVARS and acoustic coupled modes with ORCA at a receiver depth of 6 m. <i>Right Panel</i> : same at a receiver depth of 30 m.....	92
Figure 5.15: Transmission loss cross-sections at 29 Hz for Bathymetry 1 from SANMO (<i>Top Panel</i>), Acoustic Coupled Modes with ORCA (<i>Middle Panel</i>), and LAYROTVARS (<i>Bottom Panel</i>).....	94
Figure 5.16: Processing time in hours to compute transmission loss for all frequencies for each propagation track.....	96
Figure 5.17: Processing time in hours as a function of frequency to compute transmission loss for all frequencies for propagation bathymetry 2.....	97
Figure 5.18: A detailed map of survey 2, showing the locations of the hydrophone and the sail tracks from the seismic survey. The track numbering corresponds to the range dependent bathymetry scenarios discussed in section 5.1.....	98
Figure 5.19: Energy Spectral Density calculated from the signals recorded from track 3 (Bathymetry 3) showing the low frequency peaks in acoustic energy associated with propagation over a calcarenite seabed.....	99

Figure 5.20: The source spectrum from CMST's airgun array model that was used to compute the synthetic SELs. This spectrum represents an equivalent point source of the airgun array at one metre from the source centre.	101
Figure 5.21: A comparison of modelled SEL cross-sections using the source spectrum in Figure 5.20 combined with the transmission loss from LAYROTVARS and SANMO. The black dotted lines define the seafloor and the calcarenite cap-rock layer.	102
Figure 5.22: SELs computed from measured data and synthetic SELs obtained using the airgun array model source spectrum with SANMO and LAYROTVARS models.	104
Figure 5.23: SELs computed from measured data and new synthetic SELs (Track 5) obtained using the airgun array model source spectrum with SANMO and LAYROTVARS models (dashed lines) and the previous synthetic SELs in Figure 5.22.	106
Figure 5.24: SELs computed from measured data and synthetic SELs obtained using the airgun array model source spectrum with SANMO and the updated geoacoustic profile.	107
Figure B.1: TL for benchmark case ASA UP. <i>Left Panels</i> : TL at 25Hz, 50Hz, and 100Hz from RAMGEO. <i>Right Panels</i> : TL at 25Hz, 50Hz, ad 100Hz from ORCA with coupled modes	133
Figure B.2: TL for benchmark case ASA DOWN. <i>Left Panels</i> : TL at 25Hz, 50Hz, and 100Hz from RAMGEO. <i>Right Panels</i> : TL at 25Hz, 50Hz, and 100Hz from ORCA with coupled modes	134
Figure B.3: Transmission loss (TL) slice at a receiver depth of 30 metres for the upslope and downslope validation scenarios <i>Left Panels</i> : TL at 25Hz, 50Hz, and 100Hz for the upslope scenario from ORCA with coupled modes (blue curve) and RAMGEO (red curve). <i>Right Panels</i> : TL at 25Hz, 50Hz, and 100Hz for downslope scenario from ORCA with coupled modes (blue curve) and RAMGEO (red curve).	135

III. List of Tables

Table V.1: List of Symbols and Abbreviations.....	XXI
Table 1.1: Tabulated summary of the three most common propagation model types used for shallow water, low frequency sound propagation modelling and their applicability to model acoustic and seismoacoustic environment types.....	5
Table 3.1: Nominal geoacoustic properties for calcarenite and for sand from Duncan et al (2009)'s paper on the effects of a calcarenite seafloor on underwater acoustic propagation	26
Table 3.2: Geoacoustic parameters for the reflection coefficient analysis of layered calcarenite seafloors.....	30
Table 4.1: Geoacoustic properties for the ASA Elastic Wedge proposed by (Chin-Bing et al., 1993) at the ASA's second parabolic equations workshop.....	48
Table 4.2: Propagation model parameters for three benchmark cases of SANMO ...	48
Table 4.3: References for the propagation models used for benchmark comparisons of the adiabatic seismoacoustic normal mode method.....	49
Table 5.1: Geoacoustic Properties for the Layered Calcarenite Bottom proposed by Duncan et al. (2013)	76
Table B.1: Geoacoustic properties for the ASA Fluid Wedge proposed by Jensen and Ferla (1990).....	132
Table B.2: Propagation model parameters for two benchmark cases	132

IV. Acknowledgements

Most importantly I would like to acknowledge and sincerely thank Carmen Smith, Barbara Koessler, and Michael Koessler for their unwavering love, support, and encouragement from the very beginning of this journey to its conclusion. To my family and friends in Canada, Australia, and Europe, you have all helped me in reaching one of my life's goals, for this I am eternally grateful.

I would like to acknowledge and especially thank my supervisors for their steadfast support and guidance during the research process and through production of this thesis. To Dr. Alec Duncan and Prof. Alexander Gavrilov for your combined wisdom, keen insight, and patience; I could not have had a better pair of mentors. To Dr. Ross Chapman for recommendation to pursue a PhD overseas, and to Dr. Christine Erbe for the opportunity to do so. I would like to acknowledge and especially thank Dr. Jon Collis from Boulder School of Mines for providing the seismoacoustic parabolic equation model, which has been instrumental for this thesis work.

To the students, staff, and academics at Curtin University's Centre for Marine Science and Technology, you have all made this experience an enjoyable one. Finally, to the academics and staff at the UVic acoustics lab who have always been welcoming when I show up for impromptu visits.

This project has been funded by Chevron through the Western Australian Energy Research Alliance (WA:ERA) within the scope of the “Maine Noise” project (PDEP AES II-P2SR-68). Santos Energy supplied the navigation data used in Chapter 5.

Thank you all.

V. Symbols and Abbreviations

Table V.1: List of Symbols and Abbreviations

α_p	Compressional wave attenuation
α_s	Shear wave attenuation
Δ	Far-field cubic dilatation
θ	Grazing angle
λ	Wavelength
ρ	Bulk density
Φ	Compressional wave displacement potential
$\bar{\varphi}_m$	Normalised compressional wave displacement potential mode function
$\vec{\Psi}$	Vector shear wave displacement potential
Ψ	Scalar shear wave displacement potential
$\bar{\psi}_m$	Normalised shear wave displacement potential mode function
ω	Angular Frequency
c_p	Compressional wave speed
c_s	Shear wave speed
BLI	Branch Line Integral
CM+ORCA	Coupled Modes with ORCA
dB	Decibel
ESD	Energy Spectral Density
LAYROTVARS	A PE propagation model
NM	Normal Mode model
$P(r, z)$	Acoustic Pressure in Cylindrical Coordinates
PE	Parabolic Equation model
RAMSGEO	A PE propagation model
OASES	A WNI propagation model
ORCA	A NM propagation model
$R(\theta)$	Reflection Coefficient as a function of grazing angle
SANMO	Seismoacoustic Normal Modes with ORCA

SEL	Sound Exposure Level
SSP	Sound Speed Profile
TL	Transmission loss
$TL: \sigma_{zz}$	Transmission loss based on vertical normal stress
$TL: \sigma_{rr}$	Transmission loss based on radial normal stress
$TL: v_z$	Transmission loss based on vertical particle velocity
$TL: v_r$	Transmission loss based on horizontal particle velocity
WNI	Wavenumber Integration model
ZRX	Receiver Depth

CHAPTER 1 Introduction

1.1 Motivation

Predictive underwater noise modelling is often required as part of the regulatory approval process for marine industrial operations. In Australia, acoustic noise modelling is used as part of the process that assesses the potential environmental impacts of noise from operations that take place offshore within the country's exclusive economic zone. A physics based modelling method is used to predict the sound levels in the ocean produced by different types of noise sources. Accurate modelling methods are required to make the best possible assessment of the potential impacts of noise on the fauna in the marine habitat. Current noise modelling techniques attempt to accurately predict the source characteristics and the environmental effects of acoustic energy that propagates into and through the ocean. To make a prediction of acoustic levels, modelling is usually split into two parts. One part focuses on accurately modelling levels near the source the other focuses on the interaction of signals with the environment over longer ranges. The focus of this work is on the latter. The purpose of this thesis is to investigate the feasibility of using seismoacoustic propagation models, which are also known as acousto-elastic propagation models, to model sound propagation in the ocean over range dependent layered elastic seabed environments that are typical of the Australian continental shelf.

1.2 Introduction to Underwater Acoustic Propagation Modelling

In underwater acoustics, the sub discipline of sound propagation modelling has seen significant improvements over the last fifty years with the continued improvement of numerical computing. Modelling of underwater sound requires a quantitative analysis of the propagation from a source through the water column and the seafloor. A sound propagation model relates environmental parameters to the physics involved in acoustic propagation. Propagation model are then implemented as computer algorithms that take environmental variables as input parameters and returns a numerical result for the acoustic field. Research on numerical sound propagation

modelling methods and techniques has steadily improved the ability of numerical models to make accurate acoustic field predictions. This has made it possible to model increasingly complex environments; however, there are limits to how complex the environmental model can be.

When discussing a sound propagation model's ability to model various environments, modelling methods are generally classified as either range independent (RI), range dependent (RD), or 3-D models (Etter, 2013). Jensen (1982) and Etter (2013) further classify propagation models based on their applicability to model shallow water or deep water environments at low or high acoustic frequencies. The discussion here is focused on low frequency acoustic propagation in shallow water environments. For continental shelf environments with water depths less than 200 metres and frequencies below 500 Hz there is sufficient interaction with the sea bottom such that the environment may be considered as a shallow water environment.

As discussed in Etter (2013) sound propagation models based on WaveNumber Integration (WNI) models, also referred to as fast-field models, Normal Modes (NM) models, and Parabolic Equation (PE) models have been conventionally used to model shallow water, low frequency sound propagation. Generally WNI and NM models are considered to be range independent models and PE range dependent models. Currently, the state of the art in sound propagation modelling is focused on 3-D propagation modelling. For shallow water environments, 3-D acoustic models based on coupled NM (Ballard, 2012; Ballard et al., 2015) and PE (Sturm, 2005; Lin et al., 2012) modelling methods exist. A general discussion and associated literature on 3-D underwater sound propagation modelling can be found in Katsnelson et al. (2012).

In shallow water environments by definition, acoustic signals interact strongly with the seafloor, thus the type of the seafloor sediments can have a significant effect on the sound field in the water column. Seafloor sediments can be considered as fluid, elastic, or poro-elastic materials (Jackson & Richardson, 2007). Realistically sediments should be modelled as porous elastic materials where grain to grain contact forms a matrix in-between which is interstitial fluid (Biot, 1956; Stoll, 1977).

However, the physics associated with acoustic waves interacting with poro-elastic materials is complex and the parameterisation associated with the physical theory poses difficulties in both independently and accurately measuring all the parameters needed to describe the material (Holland & Brunson, 1988). So the bulk properties of seafloor sediments have commonly been used to describe the acoustic interaction with the seafloor (Hamilton, 1980). To good approximation, unconsolidated seafloor sediments have been treated and modelled as a fluid material and solid rock has been treated and modelled as an elastic material (Hamilton, 1980, 1982).

Here the focus will be on the interaction of acoustic waves in the ocean with a solid elastic seabed in range independent and range dependent environments. Generally WNI, NM, and PE models are able to model most types of range dependent fluid bottoms and WNI and PE have been shown to be capable of modelling elastic bottoms. Several range dependent seismoacoustic propagation models have been established and tested (Goh et al., 1997). However, there are some environments that cause efficiency, stability, and/or accuracy problems for range dependent seismoacoustic propagation models. Therefore, the further development and improvement of underwater acoustic range dependent seismoacoustic propagation models is still an active area of research. Seismoacoustic propagation models have also been called acoustic-elastic models; however, the term seismoacoustic is favoured here because of its extensive use in the most recent body of published literature.

1.2.1 Numerical Approaches for Handling Range Dependence with Elastic Bottoms

The modelling of range dependent seismoacoustic propagation has been carried out using WNI and PE methods, and to a much lesser extent with NM methods. The most common of these methods is the seismoacoustic PE method (Collins, 1989a). Following the first articles describing the seismoacoustic PE method (Greene, 1985; Collins, 1989a; Wetton & Brooke, 1990) for underwater acoustic applications, several improvements and modifications have been made to acoustic and seismoacoustic PE methods. Some examples of these are: energy conservation corrections (Collins, 1993a; Collins & Siegmann, 1999), rotated coordinate

mappings (Outing et al., 2006; Collis et al., 2009), and single-scatter approximations (Küsel et al., 2007; Collis et al., 2008; Metzler et al., 2012). Most of these improvements were first applied to acoustic PEs first then applied to seismoacoustic PEs. The current generation of seismoacoustic PE models may apply one or a combination of these modifications in their numerical routines and thus have been shown to be capable of providing accurate solutions to many seismoacoustic problems (Collins & Siegmann, 2015). WNI has traditionally been used for range independent modelling (Schmidt & Tango, 1986) but has been extended to range dependent acoustic applications (Schmidt et al., 1995) and seismoacoustic applications (Goh & Schmidt, 1996).

Normal modes have been used extensively for range dependent acoustic propagation modelling in underwater environments (Pierce, 1965; Evans, 1983; Godin, 2003; Jensen et al., 2011a), as well as for range dependent seismic wave propagation in purely elastic media (Kennett, 1984a; Maupin, 1988). Some work has been conducted on developing seismoacoustic range dependent normal mode methods (Arvelo, 1990; Odom et al., 1996; Tindle & Zhang, 1997; Dahl et al., 2015); however, the amount of published literature appears to be substantially less than that of PE or WNI. Table 1.1 describes the applicability of these three propagation model types for acoustic and seismoacoustic propagation based on this discussion.

Table 1.1: Tabulated summary of the three most common propagation model types used for shallow water, low frequency sound propagation modelling and their applicability to model acoustic and seismoacoustic environment types.

	Shallow Water Environments					
	Acoustic			Seismoacoustic		
Model Type	RI	RD	3-D	RI	RD	3-D
Wavenumber Integration						
Normal Mode						
Parabolic Equations						
Symbol Key for Table 1.1:						
	Applicable modelling method that is widely used and tested.					
	Applicable modelling method currently that may or may not be available for general use. There may also be limitations due to numerical accuracy and/or excessive execution time.					
	Applicable modelling method, demonstrated in proof of concept.					
	Currently not a readily applicable method, further research and development is required.					

Table 1.1 is of a similar style and format to that presented in Jensen (1982) and Etter (2013), but the focus here is on shallow water modelling methods rather than the wider classes discussed in the already cited sources.

1.3 Propagation Modelling Applied to Australia's Continental Shelf Environment

In Australia large portions of the continental shelf and upper slope are characterised by small amounts of unconsolidated sediments or alternating thin cemented sediment and semi-cemented sediment layers or sedimentary rock (Bird, 1979; James & Bone, 2011). Until recently, range dependent seismoacoustic sound propagation models have not been able to reliably model the combination of range dependent bathymetry

and elastic seabed layering that is characteristic of these environments. Duncan et al. (2013) were able to obtain realistic numerical predictions by using a rotated variable, single-scatter seismoacoustic PE model discussed in Collis et al. (2008). However, in a subsequent paper Collis and Metzler (2014) stated that, to obtain the numerically stable results presented in Duncan et al. (2013), a fine computational grid was required even at low frequencies. In conjunction with a large modelling domain, this resulted in a significant computational cost.

Considering Table 1.1, the modelling approach that is followed in this thesis is to consider the normal mode method for range dependent seismoacoustic propagation modelling. The motivations for using the normal mode method are:

- There are computationally efficient numerical algorithms that are readily available and are suitable for computing range independent seismoacoustic normal modes.
- There is a large basis of literature for both underwater acoustic and seismic propagation modelling that can be drawn upon for the theoretical development of a new propagation model.
- In the purely acoustic case, mode coupling methods have been used to extend normal modes to range dependent environments but they are usually subject to high computational cost. However, single-scatter (Porter et al., 1991) and adiabatic (Porter, 1994) approximations to coupled mode methods have been shown to be more computationally efficient. In the seismoacoustic case similar approaches may be efficient as well.
- Furthermore, a range dependent seismoacoustic normal mode model could be of use for benchmarking seismoacoustic propagation models (Collins & Siegmann, 2015), in a similar way that range-dependent benchmark testing was conducted for purely acoustic models by Jensen and Ferla (1990).

The aim of this work is to investigate the capability of normal mode method to model seismoacoustic propagation over range dependent layered seafloors, specifically addressing the computational cost of performing calculations for the types of environments discussed here.

1.4 Thesis Organisation

The organisation of this thesis is as follows:

- Chapter 2 is devoted to an introduction of the acoustic and elastic wave propagation theory and the normal mode propagation modelling method, summarising the required theoretical and mathematical information that is required herein.
- Chapter 3 discusses the Australian shallow environment and its effects on propagation of normal modes.
- Chapter 4 discusses the development of a range dependent seismoacoustic propagation model based on normal modes and provides a comparison with two seismoacoustic PE propagation models.
- Chapter 5 presents experimental data recorded from an offshore seismic survey operating in Bass Strait Australia. These data are compared with modelled results using a seismoacoustic PE and seismoacoustic normal mode predictions.
- Chapter 6 concludes the thesis with a summary and discusses further avenues for research.

CHAPTER 2 Acoustic and Elastic Wave Propagation Theory

The starting point for underwater sound propagation theory is the wave equation, the solutions of which are generally complex exponential functions that evolve in time and space. To simplify the mathematics, the time dimension is usually eliminated through a Fourier transform applied to the wave equation which results in the Helmholtz wave equation for propagation at a single frequency (Jensen et al., 2011a). Generally a given sound propagation model seeks to provide solutions to the Helmholtz equation subject to boundary conditions, that represent the interactions of the acoustic or seismic wave fields at boundaries between different media within the environment.

2.1 Governing Equations for Acoustic Waves

The generalized form of the homogeneous Helmholtz acoustic wave equation for pressure is,

$$[\nabla^2 + k^2]P(\vec{r}) = 0 \quad (2.1)$$

where k is the wavenumber, ∇^2 is the Laplacian operator, and $P(\vec{r})$ is the acoustic pressure. Here it is assumed that the material density, ρ is constant within the fluid. The wavenumber is defined by the ratio of the angular frequency ω to the sound speed in the fluid c ,

$$k = \frac{\omega}{c}. \quad (2.2)$$

The acoustic field can also be described in-terms of particle displacement $\vec{u}(\vec{r})$ and a displacement potential $\Phi(\vec{r})$ where,

$$\vec{u}(\vec{r}) = \nabla\Phi(\vec{r}). \quad (2.3)$$

The displacement potential also satisfies a Helmholtz wave equation (Jensen et al., 2011a) and the acoustic pressure can then be related to the displacement potential through Hooke's Law resulting in,

$$P(\vec{r}) = -\rho c^2 \nabla^2 \Phi(\vec{r}). \quad (2.4)$$

Since Equation (2.4) satisfies the Helmholtz wave equation for the displacement potential the acoustic pressure can be related to the displacement potential by,

$$P(\vec{r}) = \omega^2 \rho \Phi(\vec{r}) \quad (2.5)$$

The relationship between the displacement potential and pressure becomes more relevant when considering seismoacoustic wave propagation. For acoustic waves in

cylindrical coordinates and a axially symmetrical environment, the θ dependence can be removed by a spatial Fourier transform and the pressure can be written as $P(r, z)$. The wavenumber can then be decomposed into a common representation consisting of vertical and radial components,

$$k^2 = \gamma^2 + k_r^2 \quad (2.6)$$

where γ and k_r denote the vertical and radial components. These are common equations in underwater acoustic propagation modelling and can be found in standard textbooks on underwater acoustics such as Officer (1958) or Jensen et al. (2011a).

2.2 Governing Equation for Elastic Waves

For a homogeneous and isotropic elastic material, seismic wave propagation is usually described in-terms of displacements and stresses. The displacement vector \vec{u} , which generally has three components all of which individually depend on three spatial coordinates, can be written as

$$\vec{u} = [u_x, u_y, u_z]^T = [u_r, u_\theta, u_z]^T \quad (2.7)$$

in Cartesian or Cylindrical coordinates, where $u_x = u_x(x, y, z), \dots$ and $u_r = u_r(r, \theta, z), \dots$ etc. The generalised Fourier transformed wave equation for elastic wave propagation in-terms of \vec{u} is

$$-\rho\omega^2 \vec{u} = (\lambda_\ell + \mu)\nabla(\nabla \cdot \vec{u}) + \mu\nabla^2 \vec{u} \quad (2.8)$$

where λ_ℓ and μ are Lamé parameters that are related to the compressibility and rigidity of an elastic material (Aki & Richards, 1980; Ben-Menahem & Singh, 1981).

For a fluid $\mu = 0$ and Equation (2.8) reduces to Equation (2.1) above.

For elastic waves, the displacement vector \vec{u} can be related to a scalar potential for volume compression and a vector potential for shear rotation, and the displacement vector can be written as,

$$\vec{u} = \nabla\Phi(r, \theta, z) + \nabla \times \vec{\Psi}(r, \theta, z). \quad (2.9)$$

For vertically polarised plane waves, in Cylindrical coordinates and axially symmetrical environment the vector potential $\vec{\Psi}$ can be reduced to a scalar quantity

(Ewing et al., 1957). The components of the displacement vector can then be written as (Schmidt & Tango, 1986),

$$u_z = \partial_z \Phi(r, z) + k_r^2 \Psi(r, z) \quad (2.10)$$

and

$$u_r = \partial_r \Phi(r, z) + \partial_r \partial_z \Psi(r, z) \quad (2.11)$$

where the partial derivatives are written in a short hand form, i.e. ∂_z refers to the partial derivative with respect to z . Each scalar potential also satisfies their individual wave equation (Aki & Richards, 1980). The un-forced Helmholtz wave equations can be written as,

$$[\nabla^2 + k_p^2] \Phi(r, z) = \left[\nabla^2 + \frac{\rho \omega^2}{\lambda_\ell + 2\mu} \right] \Phi(r, z) = 0 \quad (2.12)$$

and

$$[\nabla^2 + k_s^2] \Psi(r, z) = \left[\nabla^2 + \frac{\rho \omega^2}{\mu} \right] \Psi(r, z) = 0 \quad (2.13)$$

where $k_p = \frac{\omega}{c_p}$, $k_s = \frac{\omega}{c_s}$, c_p is the compressional wave speed, and c_s is the shear wave speed. Now $\Phi(r, z)$ and $\Psi(r, z)$ are scalar potentials that respectively describe the propagation of compressional and shear waves. From Equation (2.12) and Equation (2.13) the Lamé parameters can be related to the seismic wave speeds,

$$\lambda_\ell = \rho(c_p^2 - 2c_s^2) \quad (2.14)$$

and

$$\mu = \rho c_s^2. \quad (2.15)$$

For far-field propagation in Cylindrical or Cartesian coordinates, Hooke's Law can be written in a tensor form (Aki & Richards, 1980; Ben-Menahem & Singh, 1981), which relates displacements and stresses in a small differential element,

$$-\omega^2 \rho u_j = \partial_i \sigma_{ij}. \quad (2.16)$$

Here the indices correspond to spatial coordinates and follow the summation convention where repeated indices implies summation (Aki & Richards, 1980). They correspond to displacement in the j^{th} direction from stress acting on the i^{th} face of a small differential element. The stress σ_{ij} is defined through a stress-strain relationship and for a linear isotropic elastic material this can be written as

$$\sigma_{ij} = \lambda_\ell \delta_{ij} e_{kk} + 2\mu e_{ij} \quad (2.17)$$

where e_{ij} and e_{kk} are strains defined by

$$e_{ij} = \frac{1}{2}(\partial_i u_j + \partial_j u_i). \quad (2.18)$$

Each stress component then can be related to displacements in Cylindrical coordinates and for an axially symmetrical environment they can then be written as,

$$\sigma_{rr} = \lambda_\ell \Delta + 2\mu \partial_r u_r, \quad (2.19)$$

$$\sigma_{rz} = \sigma_{zr} = \mu(\partial_r u_z + \partial_z u_r), \quad (2.20)$$

and

$$\sigma_{zz} = \lambda_\ell \Delta + 2\mu \partial_z u_z \quad (2.21)$$

where Δ is the cubic dilatation (Kolsky, 1963). For modelling purposes, a far-field approximation is assumed (i.e. $\vec{k} \cdot \vec{r} \gg 1$ where \vec{k} is a wavenumber vector that points in the direction of propagation) and a simple form of the cubic dilatation can be written as

$$\Delta = \partial_r u_r + \partial_z u_z. \quad (2.22)$$

In a homogeneous material the dilatation is directly related to the displacement potential by

$$\Delta = -k_p^2 \Phi(r, z) \quad (2.23)$$

which can be obtained by considering and rearranging Equation (2.12) and Equation (2.22).

2.3 Normal Modes of the Shallow Water Ocean Waveguide

The work of Pekeris (1948) is often cited as the theoretical foundation for modelling shallow water sound propagation from point sources; he is also usually credited with introducing normal mode propagation theory, see Chapter 5 in Jensen et al. (2011a). Subsequent authors (Boyles, 1984; Brekhovskikh & Godin, 1990, 1992; Frisk, 1994; Jensen et al., 2011a; Hovem, 2012; Katsnelson et al., 2012) have produced works that provides a good foundation for normal mode theory used in shallow water and deep water acoustic propagation modelling. Here the discussion is focused on normal mode solution that follows closely to the derivations of Bucker (1970), Frisk (1994), Westwood and Koch (1998), and Hovem (2012).

The underwater acoustic waveguide is usually modelled as a fluid layer containing a point source, bound from the bottom by fluid and/or solid layers, and bound from the

top by a pressure release surface. Figure 2.1 shows a diagram of this type of waveguide.

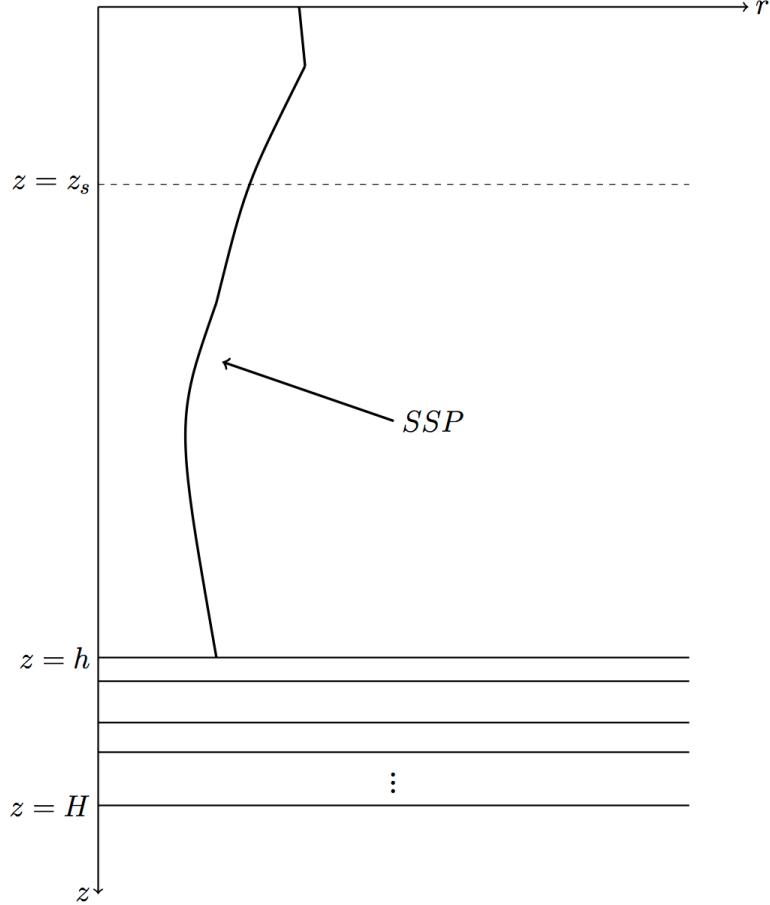


Figure 2.1: A diagram of a generalised ocean acoustic waveguide. The depths z_s , h , and H denote the source depth, depth of the seafloor, and the top of the bottom halfspace respectively. The SSP denotes the continuously varying Sound Speed Profile (SSP) in the water column.

Acoustic pressure in the frequency domain for a propagating wave in a waveguide that is axially symmetric can be written in Cylindrical coordinates as (Boyles, 1984; Frisk, 1994; Jensen et al., 2011a)

$$P(r, z) = \frac{1}{2} \int G(k_r, z, z_s) k_r H_0^1(k_r r) dk_r \quad (2.24)$$

where $G(k_r, z, z_s)$ is the depth dependent Green's function, k_r is the horizontal wavenumber and $H_0^1(k_r r)$ is the Hankel function of the first kind (Abramowitz & Stegun, 1965). The depth dependent Green's function can be defined in the form (Westwood & Koch, 1998)

$$G = \frac{\varphi(z)_+ + \varphi(z)_-}{W(z_s, k_r)} \quad (2.25)$$

where $\varphi(z)_+$ and $\varphi(z)_-$ are depth dependent solutions above and below the source and $W(z_s, k_r)$ is the Wronskian evaluated at the source depth.

There are two methods for solving Equation (2.24) (Jensen et al., 2011a; Hovem, 2012; Katsnelson et al., 2012). The Hankel transform can be evaluated by directly integrating the Greens function kernel, or the integral can be evaluated with Cauchy's residue theorem and contour integration. The first approach results in the wavenumber integration method and the latter results in the normal mode method.

For contour integrals of a complex variable, Cauchy's residue theorem states that the contour integral in the complex plane is equal to the sum of the residues within the closed contour (Arfken, 1970; Brown et al., 1996). The residue theorem takes the form

$$\oint F(\zeta) d\zeta = 2\pi i \sum_m \text{Res}(F, \zeta_m). \quad (2.26)$$

Furthermore, if $F(\zeta)$ is of the form $F(\zeta) = \frac{g(\zeta)}{h(\zeta)}$ where g is a continuous function and h is a differentiable function then the residues $\text{Res}(F, \zeta_m) = \frac{g(\zeta_m)}{h'(\zeta_m)}$ (Brown et al., 1996), and the residue sum can be written as

$$2\pi i \sum_m \text{Res}(F, \zeta_m) = 2\pi i \sum_m \frac{g(\zeta_m)}{h'(\zeta_m)}. \quad (2.27)$$

Figure 2.2 shows a schematic of the contour integration process in the complex plane, highlighting the branch line integral (BLI) and C_∞ sections of the contour. The two wavenumbers k_1 and k_2 labelled on Figure 2.2 are associated with the minimum wave speed in the water column and the wave speed in the bottom halfspace. For a layered structure over a halfspace, the integration contour must deform around the point where $k_r = k_2$ shown in Figure 2.2, this is because of a discontinuity in $G(k_r, z, z_s)$ associated with the radiation condition at infinity (Jensen et al., 2011a). The deformation of the integration contour around k_2 is usually referred to as a "branch cut". In Figure 2.2 the Pekeris branch cut is shown (Westwood & Koch, 1998; Jensen et al., 2011a) where BLI and C_∞ denote the Branch Line Integral and the semi-circle at infinity to close the contour.

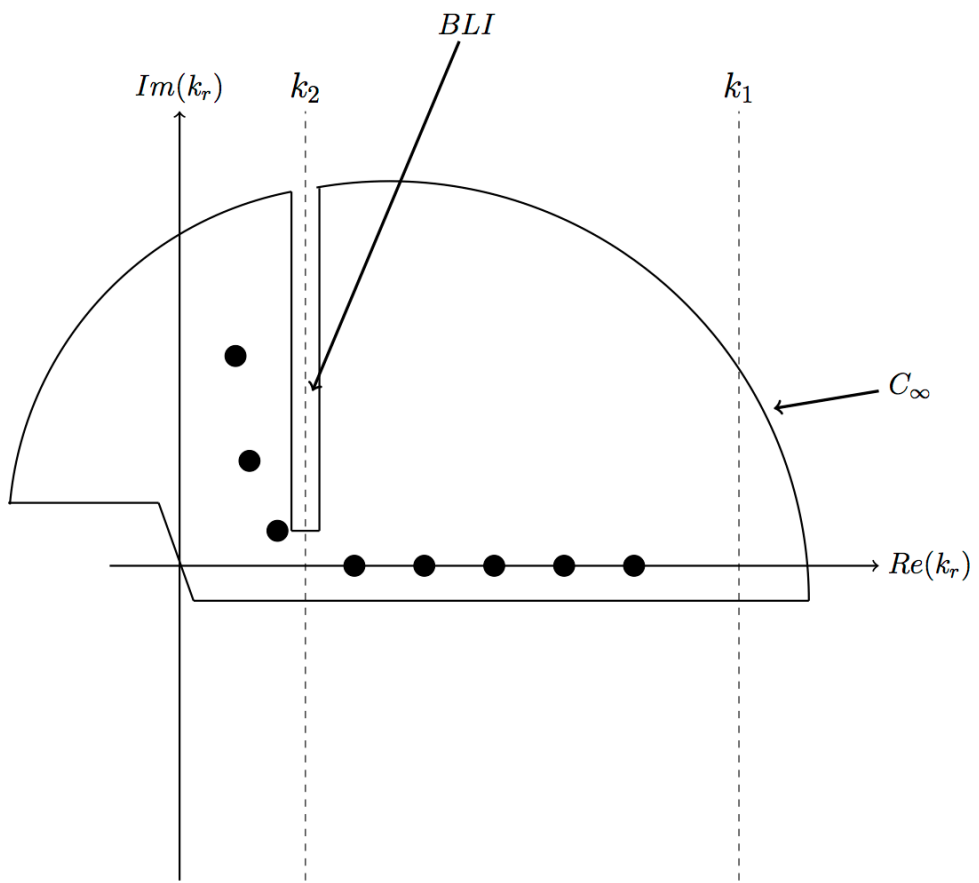


Figure 2.2: A Schematic representation of contour integration in the complex plane when the Pekeris cut is used. The black dots represent the location of the poles of the Green's function.

Applying contour integration to the problem of evaluating Equation (2.24), the contour integral can be decomposed into three terms shown below in Equation (2.28),

$$\begin{aligned}
& \frac{1}{2} \oint G(k_r, z, z_s) k_r H_0^1(k_r r) dk_r \\
&= \frac{1}{2} \int_{-\infty}^{\infty} G(k_r, z, z_s) k_r H_0^1(k_r r) dk_r \\
&+ \frac{1}{2} \int_{C_\infty} G(k_r, z, z_s) k_r H_0^1(k_r r) dk_r \\
&\quad + BLI.
\end{aligned} \tag{2.28}$$

The term associated with C_∞ equals zero because the Hankel function decays to 0 in the limit as k_r becomes infinitely large.

When considering Equation (2.28) and Equation (2.24) together, contour integration and the residue theorem leads to a common representation of acoustic pressure in terms of normal modes given in Equation (2.29):

$$P(r, z) = 2\pi i \sum_m \left(\frac{\varphi_m(z_s) \varphi_m(z)}{\partial W(z_s, k_r) / \partial k_r} k_{r,m} H_0^1(k_{r,m} r) \right) - BLI. \tag{2.29}$$

The product of $\varphi(z)_+$ and $\varphi(z)_-$ in the Green's function have been written as $\varphi_m(z)$ and $\varphi_m(z_s)$ because they are required to match at the source depth up to an arbitrary constant (Jensen et al., 2011a; Hovem, 2012; Katsnelson et al., 2012). Most authors neglect the BLI term in normal mode analysis (Jensen et al., 2011a) because the evaluation of the integral can be difficult for complex environments and because the terms in the BLI usually decay faster than the rest of the field (Frisk, 1994).

Now the Wronskian in Equation (2.25) can also be defined in terms of upward and downward looking reflection coefficients, R_2 and R_1 shown in Figure 2.3 (Bucker, 1970; Frisk, 1994; Westwood & Koch, 1998). Several authors have noted that this definition leads to a novel method for finding modal wavenumbers $k_{r,m}$ and for computing the mode functions required by the summation in Equation (2.29). The modal wavenumbers occur at the poles of the Green's function, i.e. when $W = 0$ (Tindle & Chapman, 1994). Therefore, in terms of reflection coefficients the criterion for finding modal wavenumbers is

$$W(k_{r,m}, z_s) = 2iA\gamma_{m,z_s}(1 - R_1R_2) = 0. \quad (2.30)$$

Here the reflection coefficients are calculated in a vanishingly small layer about the source depth (Westwood & Koch, 1998). Figure 2.3 shows a schematic that is similar to generalised waveguide in Figure 2.1 but with the addition of the two reflections coefficients calculated within this vanishingly small layer (i.e. $\epsilon \rightarrow 0$).

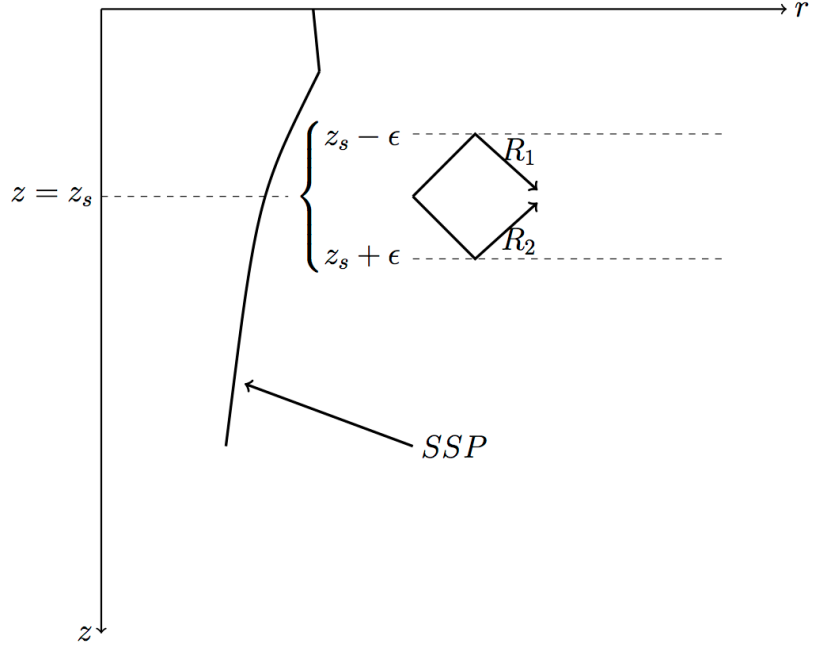


Figure 2.3: A schematic representation of the ocean acoustic waveguide showing the reflection geometry that produces acoustic propagation as normal modes.

The mode functions $\varphi_m(z)$ in Equation (2.29) are usually normalised such that the pressure can be written as,

$$P(r, z) = \frac{\pi i}{\rho_s} \sum_m \bar{\varphi}_m(z_s) \bar{\varphi}_m(z) H_0^1(k_{r,m} r). \quad (2.31)$$

The normalised mode functions $\bar{\varphi}_m$ are scaled by a quantity N_m where

$$N_m^2 = \frac{2k_{r,m}}{\rho_s \partial W(z_s, k_{r,m}) / \partial k_r}. \quad (2.32)$$

For purely fluid environments, the normalised mode functions satisfy the integral condition that

$$I_{mn} = \int_0^\infty \frac{\bar{\varphi}_m(z) \bar{\varphi}_n(z)}{\rho(z)} dz = \begin{cases} 1 & m = n \\ 0 & m \neq n \end{cases} \quad (2.33)$$

Other authors have defined normal mode normalisation N_m^2 through this integral condition rather than the Wronskian in Equation (2.32).

2.3.1 The Elastic Pekeris Waveguide

A general discussion of normal mode propagation has been presented above; however, it is useful to examine some fundamentals of the range independent normal mode problem for a fluid layer over an elastic halfspace. This is referred to as the elastic Pekeris waveguide (Press & Ewing, 1950). Rigorous treatment of the elastic Pekeris environment and other range independent seismoacoustic problems can be found in Ewing et al. (1957). Further analysis has been conducted by Ellis and Chapman (1985) and McCollom and Collis (2014) who have made full wave field predictions and developed numerical models based on the original works of Ewing et al. (1957). Some recent work has benchmarked the equations given in Press and Ewing (1950) against laboratory data (Schneiderwind et al., 2012).

For vertically polarised shear waves, the two potentials in Equation (2.12) and Equation (2.13) can be written as normal mode summations (Koch et al., 1983; Ellis & Chapman, 1985; Westwood et al., 1996):

$$\Phi(r, z) = \sum_m \varphi_m(z) \eta_m(r) \quad (2.34)$$

and

$$\Psi(r, z) = \sum_m \psi_m(z) \eta_m(r). \quad (2.35)$$

For the elastic Pekeris waveguide both compressional and shear mode functions satisfy their own depth separated equations:

$$\varphi_m'' + \gamma_{p,m}^2 \varphi_m = \varphi_m'' + \left(\frac{\omega^2}{c_p^2} - k_{r,m}^2 \right) \varphi_m = 0 \quad (2.36)$$

and

$$\psi_m'' + \gamma_{s,m}^2 \psi_m = \psi_m'' + \left(\frac{\omega^2}{c_s^2} - k_{r,m}^2 \right) \psi_m = 0, \quad (2.37)$$

but they share the same horizontal wavenumber and have the same range equation (Koch et al., 1983). The normal mode solution for the acoustic field in the water and the seismic field in the bottom can be written as

$$\varphi_m(z) = A_m \sin(\gamma_{p,m} z), \quad z \leq H \quad (2.38)$$

$$\varphi_m(z) = C_m e^{i\gamma_{p,m}(z-H)}, \quad z > H \quad (2.39)$$

$$\psi_m(z) = D_m e^{i\gamma_{s,m}(z-H)}, \quad z > H. \quad (2.40)$$

The amplitude coefficients are found through the appropriate boundary conditions at the horizontal interface between the fluid waveguide and elastic halfspace. The boundary conditions that need to be conserved for a fluid-solid interface or a solid-solid interface can be found in Jensen et al. (2011a). For a fluid-solid interface, three boundary conditions are required: the continuity of vertical stress, vanishing tangential stress in the fluid, and continuity of vertical displacement. These conditions are given below in the same order,

$$\begin{aligned} -P_1 &= \sigma_{zz_2} \\ 0 &= \sigma_{zr_2} \\ u_{z_1} &= u_{z_2}, \end{aligned} \quad (2.41)$$

where the subscripts x_1 and x_2 represent quantities in the fluid layer and the elastic halfspace respectively. The depth dependent parts of the stresses and displacement are related to the normalised mode functions $\bar{\varphi}_m(z)$ and $\bar{\psi}_m(z)$ by the following equations:

$$\frac{\sigma_{zz,m}}{\omega^2} = -\rho(z)\bar{\varphi}_m(z) + \frac{2k_{r,m}^2}{k_s^2} \left(\bar{\varphi}_m(z) + \frac{d\bar{\psi}_m(z)}{dz} \right), \quad (2.42)$$

$$\frac{\sigma_{zr,m}}{\mu\omega^2} = ik_{r,m} \left(2\partial_z \bar{\varphi}_m(z) + 2k_{r,m}^2 \bar{\psi}_m(z) - k_s^2 \bar{\psi}_m(z) \right), \quad (2.43)$$

and,

$$u_{z,m} = \frac{d\bar{\varphi}_m(z)}{dz} + k_{r,m}^2 \bar{\psi}_m(z). \quad (2.44)$$

The mode functions are scaled such that the normalisation integral, I_{nm} is equal to unity when m is equal to n :

$$I_{mn} = \int_0^\infty \rho(z) \left(\bar{\varphi}_m \bar{\varphi}_n + \frac{1}{2} \left(\frac{\sigma_{zr,m}}{\mu\omega^2} \bar{\psi}_n + \frac{\sigma_{zr,n}}{\mu\omega^2} \bar{\psi}_m \right) \right) dz = \begin{cases} 1 & m = n \\ 0 & m \neq n \end{cases} \quad (2.45)$$

This normalisation condition also serves to determine the last unknown amplitude A_m , such that

$$A_m = \frac{1}{\sqrt{I_{mm}}} \quad (2.46)$$

Ellis and Chapman (1985) have also shown that for the elastic Pekeris waveguide this normalisation integral is equivalent to the more general normalisation given above by the derivative of the Wronskian in Equation (2.32).

These depth separated equations and associated solutions are also valid for waveguides made of isovelocity layers (Koch et al., 1983; Hughes et al., 1990; Westwood et al., 1996), but theoretically they are not appropriate when vertical gradients in either the compressional or shear wave speeds produce continuous coupling between $\bar{\varphi}_m(z)$ and $\bar{\psi}_m(z)$ within an elastic layer. However, Vidmar and Foreman (1979) have found that neglecting continuous coupling of compressional and shear mode functions within elastic layers that contain gradients is acceptable for many applications in underwater acoustics. As such, any coupling between compressional and shear potentials through continuous wave speed gradients is neglected in the following analysis. However if this is an insufficient assumption, gradient layers could be replaced with many thin isovelocity layers to better replicate the effects of continuous coupling (Schmidt & Tango, 1986; Hall, 1995; Westwood et al., 1996).

The homogeneous range equation for both compressional and shear modes given in Equation (2.34) and (2.35) in Cylindrical coordinates is:

$$\frac{d^2\eta}{dr^2} + \frac{1}{r} \frac{d\eta}{dr} + k_r^2 \eta(r) = 0. \quad (2.47)$$

The solutions are Hankel functions (Ewing et al., 1957). When applying an asymptotic approximation to $H_0^{(1)}(k_r r)$, which is valid for far-field propagation, range solution is proportional to exponential form,

$$\eta(r) \propto \frac{e^{ik_r r}}{\sqrt{k_r r}}. \quad (2.48)$$

2.4 Summary Remarks

The purpose of this chapter is not to simply repeat known equations and theory but to provide a consistent theoretical basis that can be drawn on throughout the thesis. In particular the authors that have been cited use slightly different notation to represent

various quantities or parameters. Moreover, this becomes further complicated when considering literature from underwater acoustic propagation modelling and seismic wave propagation modelling, the results of which are important for the work considered here.

The theoretical framework for normal modes has been incorporated into various general-purpose sound propagation models that are capable of calculating the sound field in oceans with acoustic and elastic layers. ORCA (Westwood et al., 1996) and KRAKENC (Porter & Reiss, 1985) are two common sound propagation models that can be used to solve seismoacoustic normal mode problems and they have been widely used circa the last twenty years. An extensive list of other propagation models can be found in Etter (2013).

CHAPTER 3 Acoustic Propagation over Australian Seafloors

3.1 Introduction

The focus of this chapter is to link acoustic propagation phenomena that are associated with an elastic seafloor with the geological setting around Australia. In particular the discussion is focused on describing the influence of the seabed on signals that propagate in shallow water environments. The general geologic setting around continental Australia is dominated by calcareous rocks and sediments which can be found along large portions of the Australian continental shelf and slope (James & Bone, 2011). The cementation and/or partial cementation of these sediments allows the sub-bottom to support the propagation of elastic waves. It is the excitation of elastic waves in the seabed that influences the shallow water acoustic propagation characteristics and it is these characteristics that will be discussed.

3.2 Australian Continental Shelf Regional Geology

Generally, calcareous sediments and calcareous rocks characterise the seabed of the continental shelf along southern and western Australia (James & Bone, 2011). The low depositional flux of sediment along large sections of the Australian coast has allowed for significant weathering of any sediments that are deposited (Collins, 1988; James et al., 1994) and past mean sea level variations have reworked, and/or cemented the shelf and upper slope sediments. These processes are thought to have formed various layers of cemented or semi-cemented calcarenite that are present at the seafloor and within the sub-bottom (Collins, 1988; James et al., 1994). In some areas, a thin veneer of recent Quaternary sand on the order of a metre overlaying cemented and/or semi-cemented limestone can occur. However, sand thicknesses are not necessarily distributed uniformly (Gostin et al., 1988; James et al., 1994). Moreover, as the water depth increases offshore, unconsolidated sediments begin to dominate the sedimentary characteristics of the seabed environment (Feary & James, 1998; Feary et al., 2000; James et al., 2004). These factors create a distinct seabed environment on Australian continental shelf especially when compared to other

continental shelf analogues (Seibold & Berger, 1996). The uniqueness of the shelf environment discussed herein is a consequence of the little to no unconsolidated sediment cover that can occur over a large area (James & Bone, 2011).

Figure 3.1 shows a map outlining the approximate geographical extent of this style of carbonate environment; the bounds are approximate and were drawn considering literature (Bird, 1979; Gostin et al., 1988; James & Bone, 2011).

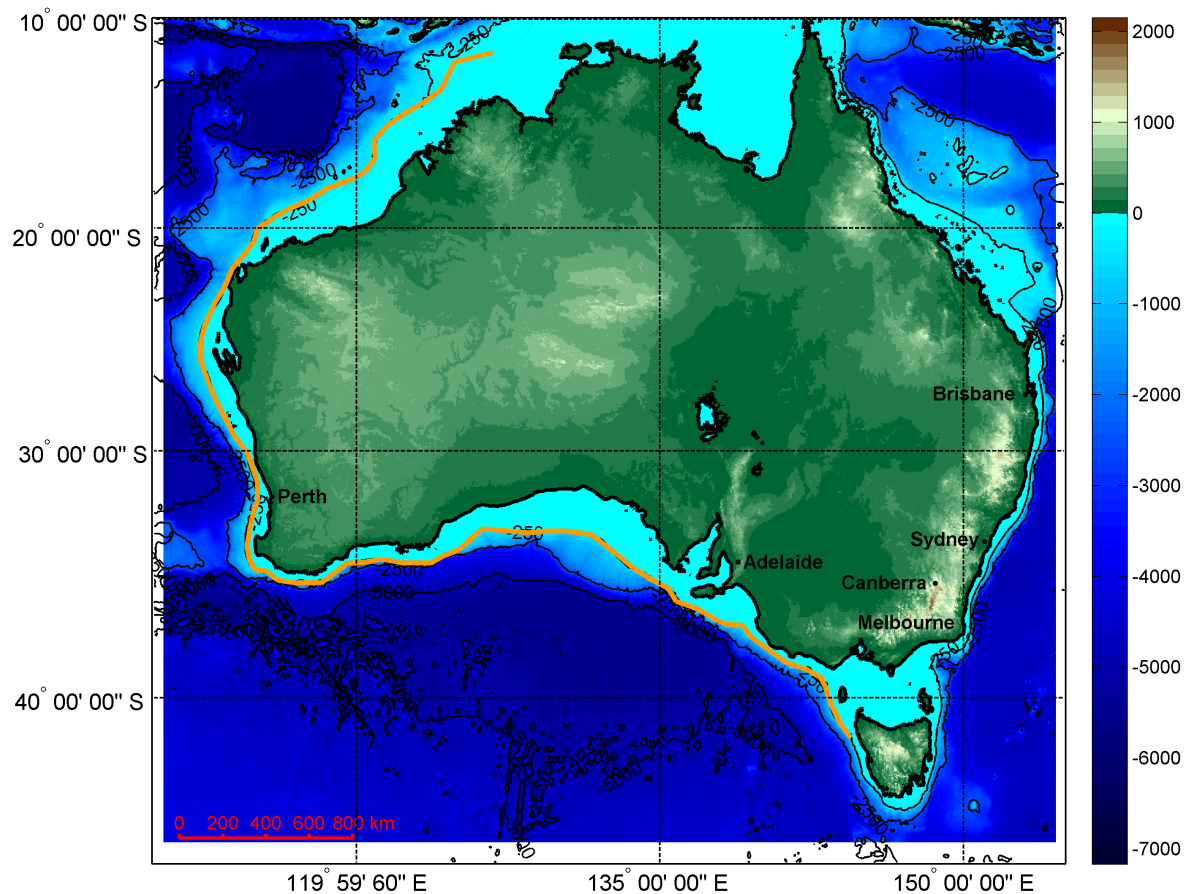


Figure 3.1. Approximate geographical extent of calcarenite seafloors defined from studies investigating Australian seafloor geology and the shallow water acoustic propagation characteristics.

There is a point to be made about the nomenclature of the seabed sediments or rock when comparing the geologic and underwater acoustic literature on the subject. Previous shallow water acoustics studies have commonly referred to the Australian carbonate seafloor as a calcarenite (Duncan et al., 2009). While this nomenclature has been used by underwater acousticians to describe the seafloor geology, it may

not be completely precise for all carbonate seabeds that occur within the bounds drawn in Figure 3.1. A calcarenite is described by Grabau (1903) as a calcareous sandstone, however further expansion of the carbonate classification schemes by Dunham (1962) and later summarised by Flugel and Munnecke (2010) add more textural and provenance information into a given carbonate rock's name. Therefore, a calcarenite may not be a precise geological description for all seabeds around the continent; moreover geologic literature may not refer to the seafloor geology as a calcarenite. The term calcarenite as applied to Australian seafloor sediment should therefore be considered as a more general name rather than a precise sedimentological definition. The precise nomenclature of carbonate seabeds found throughout Australian waters is beyond the scope of this thesis; however, it is important to bear in mind these naming conventions between disciplines

3.3 Geoacoustic models for a Calcarenite Seafloor

The cementation or partial cementation of calcarenite suggests that it has a higher shear rigidity than typical unconsolidated seafloor sediments. The compressional wave speed has been estimated to vary from 2100 m/s to 2800 m/s and the shear wave speed in calcarenite has been estimated to vary from 500 m/s to 1400 m/s (Fan et al., 2009; Duncan et al., 2013). Both the compressional and shear wave speed variations are assumed to depend on the degree of grain to grain cementation (Hamilton, 1982; Mavko et al., 2009).

In Western Australia, Duncan et al. (2008) and Fan et al. (2009) conducted geoacoustic inversion studies using simulated annealing and head wave analysis techniques applied to airgun signals recorded on a seafloor hydrophone. The results from both studies had significant uncertainties associated with the inverted parameters but in each case they indicated that there was calcarenite present at the seafloor. Duncan et al. (2008) proposed a layered geoacoustic model of sand overlying calcarenite and Fan et al. (2009) proposed a calcarenite seafloor over a deeper acoustic basement. Duncan et al. (2009) summarise these findings and specifically discuss the sound propagation effects of a calcarenite seafloor and the influence of a thin sand layer over a calcarenite bottom. Table 3.1 lists the

geoacoustic parameters of calcarenite and sand used by Duncan et al. (2009) and can be considered as an upper bound for the geoacoustic parameters of calcarenite.

Table 3.1: Nominal geoacoustic properties for calcarenite and for sand from Duncan et al (2009)'s paper on the effects of a calcarenite seafloor on underwater acoustic propagation

Material Type	ρ (g/cm ³)	c_p (m/s)	c_s (m/s)	α_p (dB/λ)	α_s (dB/λ)
Calcarenite	3.4	2800	1400	0.1	0.2
Sand	1.8	1700	0.0	0.8	0.0

Acoustic studies from Bass Strait near Tasmania indicate a third style of calcarenite seabed. Again acoustic signals from a seismic survey were recorded on a seafloor mounted hydrophone. Gavrilov et al. (2012) found that by including a hard cap-rock layer of calcarenite on top of a semi-cemented bottom produced a better match between modelled signals and measurements. Moreover, a geotechnical report from Fugro (2004) also indicates the presence of a hard layer at the seafloor from several cores drilled in Bass Strait. This report discusses the results of a downhole piezocone penetrometer profile. The piezocone penetrometer measures material resistance from a forced piston and it can be used to determine material's compaction or cementation (Beringen et al., 1982). The profile is shown in Figure 3.2 and clearly indicates a layered structure with a very hard layer followed by alternating softer and harder layers.

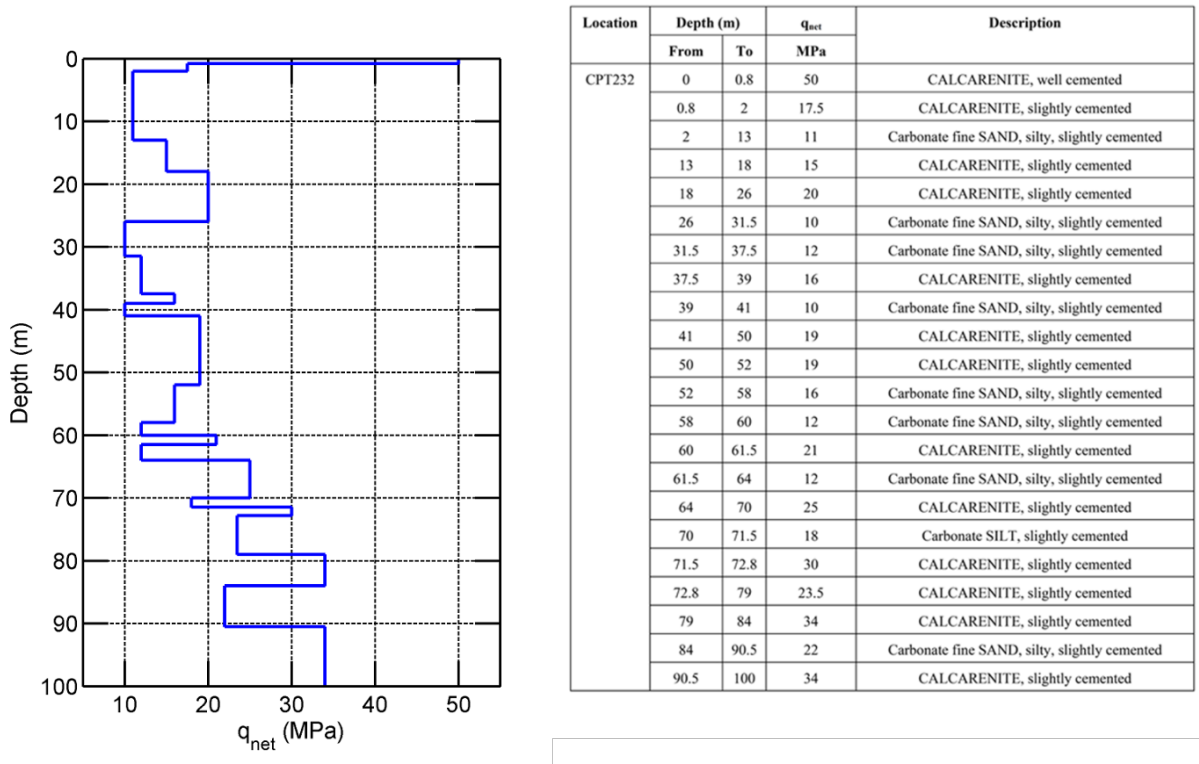


Figure 3.2: From the geotechnical report commissioned by Fugro (2004) showing the piezocone penetrometer profile to a maximum depth of 100 m below the seafloor. **Left Panel:** A plot the net resistance from a piston piezocone test. **Right Panel:** Tabulated values of net resistance and a lithology description from Fugro (2004).

The studies discussed here highlight three distinct types of seabeds. Real seabeds around the Australian continental shelf are likely to exhibit a wide variety of characteristics that are essentially combinations of the properties of the three seabeds described above. For the purposes of the work in this thesis, these three cases were considered to be sufficiently representative. In general a sedimentary basement of much harder rock should underlie all these formations. Moreover, the geoacoustic parameters discussed here for calcarenite are not comparable to that of common seabed types (Hamilton, 1980) usually considered for shallow water acoustic modelling (Katsnelson et al., 2012).

3.4 Sound Reflection from Calcareous Seafloors

Since the average shear wave speed in calcarenite is lower than the sound speed in water, the major influence of the sub-bottom shear is to introduce additional energy loss mechanism to the propagating water column sound field (Duncan et al., 2009).

The effects of an elastic halfspace composed of calcarenite can be readily examined by considering the plane wave reflection coefficient. Figure 3.3 shows the magnitude of the reflection coefficient from a halfspace of calcarenite and a halfspace of sand, the geoacoustic properties of these halfspaces are presented in Table 3.1. The reflection coefficient code BOUNCE (Porter, 2007) was used to calculate the reflection coefficient curves in Figure 3.3.

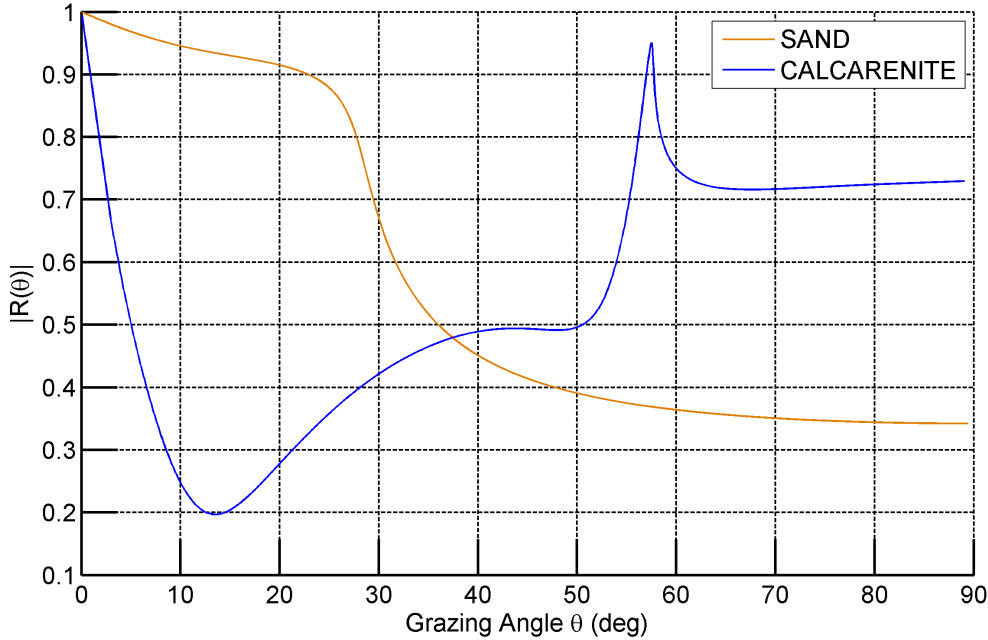


Figure 3.3: Comparison of plane wave reflection coefficients from calcarenite and sand bottoms where θ refers to the grazing angle. The geoacoustic parameters used to represent the bottom are given in Table 3.1.

Two points are evident here,

- For both geoacoustic models there is an energy loss mechanism that can be seen in the magnitude of reflection coefficient. This loss mechanism is expressed as a decrease in amplitude of $|R|$ away from unity at low grazing angles. However, because the shear wave speed in the calcarenite bottom is large, reflection from a calcarenite halfspace is subject to higher loss compared to a sand halfspace at grazing angle less than the critical angle (the critical angle is approximately 56° for the calcarenite curve and 24° for the sand curve).

- The calcarenite reflection coefficient has a sharp peak at 56° (the critical grazing angle). This means that there is a small range of grazing angles near the critical angle where a significant amount of energy is reflected back into the water column.

The inclusion of layers in the bottom introduces a frequency dependent component to the reflection coefficient amplitude, where reflected waves in the sub-bottom can interfere constructively or destructively at certain frequencies (Vidmar, 1979; Vidmar, 1980b, 1980a; Hovem & Kristensen, 1992; Chapman & Chapman, 1993; Ainslie, 1995; Clark, 2012). Seafloors around Australia realistically consist of a layered system of cemented and/or unconsolidated sediments as discussed above. So to examine the influence of a layered structure on seafloor reflected waves, the amplitude of the reflection coefficient was computed for the several different bottom configurations discussed in Section 3.3. These include a calcarenite halfspace, a thin layer of sandy sediment over calcarenite halfspace and a thin layer of cap-rock overlying a calcarenite halfspace, and a calcarenite bottom underlain by a solid reflective sedimentary basement. The geoacoustic parameters for each bottom case are tabulated in Table 3.2. Notice that the geoacoustic parameters for this calcarenite halfspace differ from Table 3.1 and from Duncan et al. (2009). The lower compressional and shear speeds in Table 3.2 would correspond to a slightly softer, slightly less cemented style of calcarenite. These values for calcarenite are consistent with literature values from Duncan and Gavrilov (2012) and Gavrilov et al. (2012). Six discrete frequencies of 10 Hz, 20 Hz, 50 Hz, 100 Hz, 200 Hz, and 500 Hz are considered to investigate the frequency dependence of reflection coefficient. Again, the reflection coefficient code BOUNCE (Porter, 2007) was used to perform the calculations and the reflection coefficient curves are presented in Figure 3.4.

Table 3.2: Geoacoustic parameters for the reflection coefficient analysis of layered calcarenite seafloors.

A: Calcarenite Bottom						
	H (m)	ρ (g/cm ³)	c_p (m/s)	c_s (m/s)	α_p (dB/λ)	α_s (dB/λ)
Calcarenite	N/A	2.0	2200	1000	0.1	0.2
B: Thin Cap-rock Layer – Calcarenite Bottom						
	H (m)	ρ (g/cm ³)	c_p (m/s)	c_s (m/s)	α_p (dB/λ)	α_s (dB/λ)
Cap-rock Layer	1	2.2	2600	1200	0.2	0.4
Calcarenite	N/A	2.0	2200	1000	0.1	0.2
C: Thin Sand Layer – Calcarenite Bottom						
	H (m)	ρ (g/cm ³)	c_p (m/s)	c_s (m/s)	α_p (dB/λ)	α_s (dB/λ)
Thin Sand Layer	1	1.8	1700	0.0	0.8	0.0
Calcarenite	N/A	2.0	2200	1000	0.1	0.2
D: Calcarerite Bottom – Sedimentary Basement						
	H (m)	ρ (g/cm ³)	c_p (m/s)	c_s (m/s)	α_p (dB/λ)	α_s (dB/λ)
Calcarerite	600	2.0	2200	1000	0.1	0.2
Sedimentary Basement	N/A	3.0	3200	1700	0.1	0.2

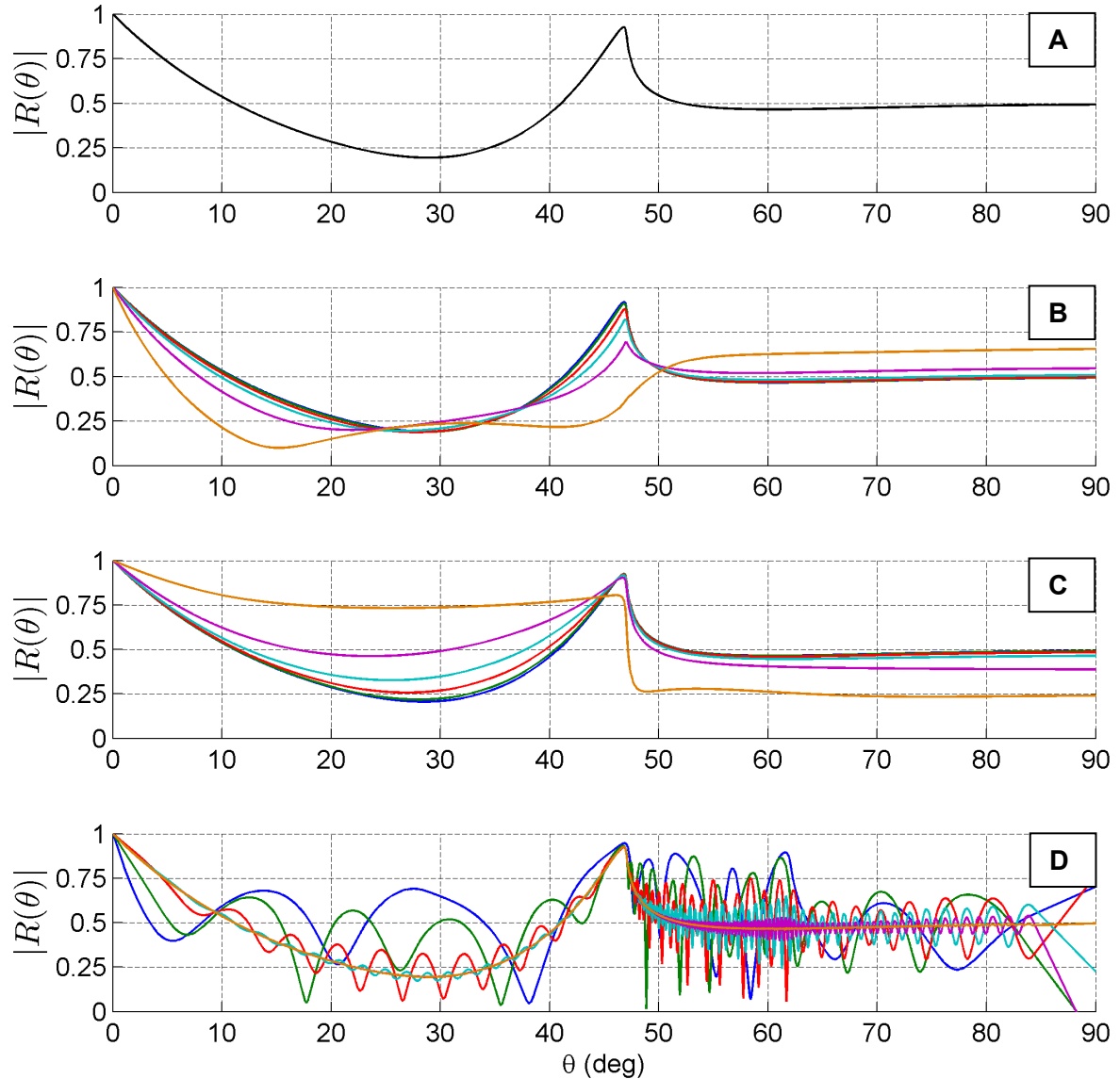


Figure 3.4: Plane wave reflection coefficient magnitude for the scenarios presented in Table 3.2. The black curve in the top panel corresponds to the halfspace scenario which does not depend on frequency; the other colour curves corresponds to the frequencies: 10 Hz – blue, 20 Hz – green, 50 Hz – red, 100 Hz – cyan, 200 Hz – magenta, and 500 Hz – orange. (A) Calcareous Basement (B) Thin Cap-rock Layer – Calcareous Basement (C) Thin Sand Layer – Calcareous Basement (D) Calcareous Basement – Sedimentary Basement.

The reflection coefficient magnitudes presented above show how different layered structures affect the reflected energy at different grazing angles and frequencies. At low frequencies the thin layers have no major effect on the reflection coefficient. However as the frequency increases the wavelength of an incident wave decreases and the reflection coefficient magnitude becomes more sensitive to the metre thick layer of sand or cap-rock. However, effect is opposite for the two thin layer cases, at

higher frequencies the sand layer generally results in a higher reflection coefficient magnitude below the critical angle, whereas the cap-rock layer exhibits a larger amount of energy loss at higher frequencies. The individual effects of the two thin layers have been discussed independently by Duncan et al. (2009) and Duncan et al. (2013) respectively.

In contrast to the thin layer scenarios the inclusion of an interface deep within the sub-bottom has a significant effect at lower frequencies. Since the thickness of the calcarenite layer is greater than both compressional and shear wavelengths, both wave types are allowed to propagate and reflect off the basement, returning energy to the water column. As the frequency increases and the wavelength decreases, a greater number of wavelengths fit into the thick calcarenite layer; therefore each propagating wave is subject to higher attenuation in the calcarenite layer both before and after reflection. Less energy is then reflected back to the seafloor interface and the reflection coefficient begins to resemble the calcarenite halfspace reflection coefficient shown in the top plot.

3.5 Sea Bottom Effect on the Propagation of Normal Modes

Since the ultimate aim of this study is to investigate the range dependent propagation of sound over calcarenite bottoms using normal modes, it is important to first consider the range independent effects of calcarenite seabeds. From the discussion above, the high shear speed and associated shear wave propagation in calcarenite adds another energy loss mechanism to acoustic waves reflected from the bottom. When the shear wave speed is less than the sound speed in water the complex parts of modal wavenumbers account for both material absorption loss and compressional to shear wave conversion in the bottom (Katsnelson et al., 2012). The analysis here considers how the reflection coefficient of a calcarenite seabed affects the modal wavenumber locations in the complex plane.

From the discussion about the plane wave reflection coefficient above and the representation of the acoustic field in terms of normal modes in Chapter 2, the modal wavenumbers $k_{r,m}$ are found when the Wronskian W , (Bucker, 1970) given below, is zero,

$$W(k_{r,m}, z_s) = A\gamma_{m,z_s}(1 - R_1R_2) = 0. \quad (3.1)$$

Here R_1 and R_2 are the reflection coefficients of upward travelling and downward travelling waves, γ_{m,z_s} is the vertical wavenumber of a compressional mode at the source depth, and A is a constant (see Figure 2.3 for a schematic). Other equally valid criteria for finding wavenumbers are $R_1R_2 = 1$ or $(1 - R_1R_2) = 0$.

From the eigenvalue criterion in Equation (3.1), the propagation of normal modes can be interpreted as constructively interfering reflected waves (Frisk, 1994). For a simple isovelocity water column over an elastic halfspace, the upward and downward reflection coefficients can be written as $R_1 = R_s e^{2i\gamma_m z_s}$ and $R_2 = R_b e^{2i\gamma_m(H-z_s)}$ (Ellis & Chapman, 1985), where H is the thickness of the waveguide and $R_s = -1$. The eigenvalue criterion of $(1 - R_1R_2) = 0$ reduces to,

$$1 + e^{2i\gamma_m H} R_b = 0. \quad (3.2)$$

In this form Equation (3.2) provides a simple link between a modal wavenumber and the bottom reflection coefficient R_b . If R_b is written in a complex exponential form,

$$R_b = |R(\theta)|e^{-i\phi(\theta)} \quad (3.3)$$

where ϕ is the phase of the reflection coefficient and $|R|$ is the magnitude. Taking a natural logarithm of Equation (3.2) yields,

$$2\gamma_m H - \phi(\theta_m) - i \ln|R(\theta_m)| - \pi(2m - 1) = 0 \quad (3.4)$$

and isolates the vertical wavenumber γ_m . Equation (3.4) directly relates the vertical modal wavenumber to the quantities of the reflection coefficient, and from γ_m using Equation (2.6), the horizontal wavenumbers, $k_{r,m}$, can be found. This approach for finding modal wavenumbers is also discussed by Tindle and Chapman (1994) and Duncan et al. (2013). The eigenvalue criterion in Equation (3.1) is also used by ORCA to find normal mode wavenumbers (Westwood et al., 1996).

By comparing Equation (3.4), to the characteristic equation for a perfectly reflecting rigid bottom (Jensen et al., 2011a),

$$2\gamma_m H - \pi(2m - 1) = 0 \quad (3.5)$$

the effect of a penetrable elastic bottom becomes apparent. Compared to the characteristic equation in a perfectly reflecting waveguide, the reflection coefficient of a penetrable bottom changes the real part of the mode by the phase factor $\phi(\theta_m)$,

and adds an imaginary component to the mode wavenumber via $\ln|R(\theta_m)|$ if attenuation or shear waves are present.

For a waveguide of constant thickness the number of propagating modes are limited by the cutoff frequency of the waveguide (Urick, 1967). Equation (3.6) gives the expression to compute the cutoff frequencies of each mode based on the water depth (H), water column wave speed (c_w), and bottom compressional wave speed (c_b),

$$f_m = \frac{\left(m - \frac{1}{2}\right)c_w}{2H\sqrt{1 - \left(\frac{c_w}{c_b}\right)^2}} \quad (3.6)$$

So at higher frequencies more wavelengths are permitted in the waveguide, which allows more modes to propagate. This equation can also be rearranged to obtain cut-off depth of a waveguide by solving for H .

Figure 3.5 shows the reflection coefficient and the corresponding mode locations for an elastic calcarenite halfspace, the parameters of which are given in Table 3.1. The waveguide is isovelocity with a water depth of 130 m. In the two panels are the magnitude and phase of the plane wave refection coefficient. The quantities that relate the reflection coefficient to the imaginary and real parts of each modal wavenumber are also plotted for mode one through to mode four. The quantities related to $|R(\theta_m)|$ and $\phi(\theta_m)$ are given in Equation (3.7) and Equation (3.8). They are plotted at grazing angles corresponding to each mode as given by Equation (3.9),

$$|R(\theta_m)| = e^{2H \left(\operatorname{Im} \left(\sqrt{k_w^2 - k_{r,m}^2} \right) \right)}, \quad (3.7)$$

$$\phi(\theta_m) = 2H \left(\operatorname{Re} \left(\sqrt{k_w^2 - k_{r,m}^2} \right) \right) - \pi(2m - 1), \quad (3.8)$$

and

$$\theta_m = \cos^{-1} \left(\frac{k_{r,m}}{k_w} \right). \quad (3.9)$$

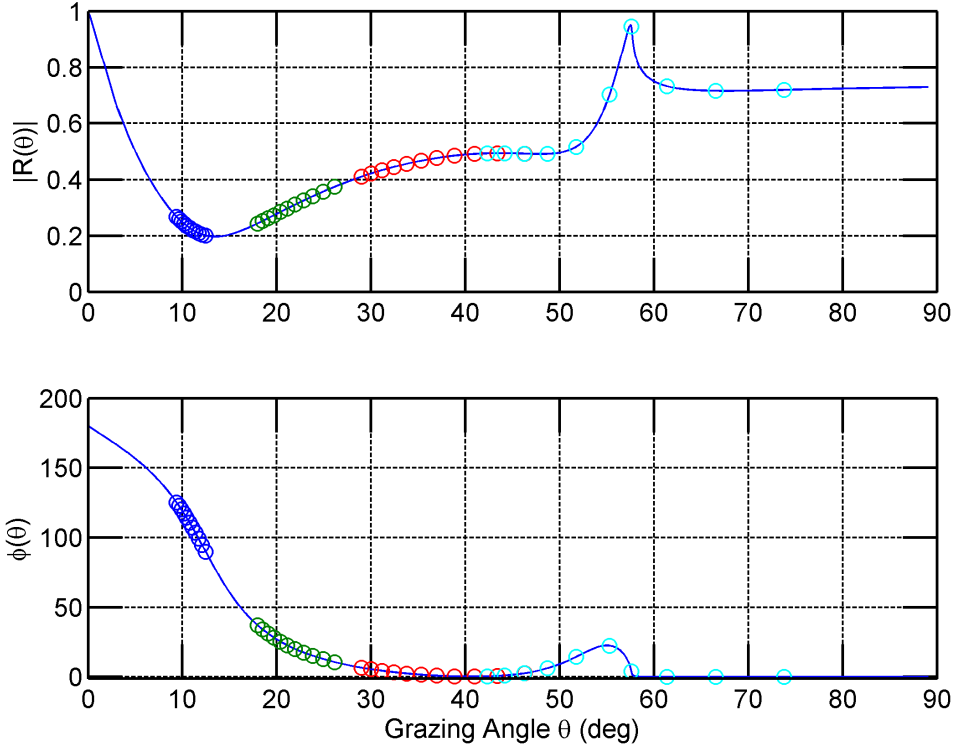


Figure 3.5: The magnitude (*Top Panel*) and phase (*Bottom Panel*) of the reflection coefficient and locations of modal components from Equation (11) and Equation (12), the modal components move from right to left as the frequency increases from 20 Hz to 30 Hz. Each mode is colour coded, blue – mode 1, green – mode 2, red – mode three, and cyan – mode four.

These modes are plotted from 20 Hz to 30 Hz in 1 Hz increments. The important feature of this plot is that it shows the modes moving from high grazing angles to low grazing angles as frequency increases. This highlights the effect that the reflection coefficient has on the real and imaginary parts of the modal wavenumbers. When considering normal modes as constructively interfering rays at a specific grazing angle, the magnitude of the reflection coefficient controls the amplitude of a reflected ray at that angle; therefore, the reflection coefficient controls the amplitude of a given normal mode propagating at a specific grazing angle. As such, the modal attenuation coefficient (i.e. the imaginary part) is directly related to the amount of amplitude loss given by the reflection coefficient whereas the real part of the modal wavenumber is related to the phase of the reflection coefficient. Referring back to Figure 3.5, as the frequency increases mode four passes near the critical grazing angle is subject to a much lower loss due to bottom reflection coefficient. This figure illustrates that at specific frequencies close to the cutoff frequency a single

mode will propagate at a grazing angle where a minimum amount of energy transferred to shear waves in the sub-bottom. All other modes will be subject to high attenuation coefficients.

Figure 3.6 shows the modal wavenumber trajectories in the complex plane as frequencies increase from 1 Hz to 100 Hz incremented at 0.25 Hz. The modal attenuation (imaginary part) of each mode is reported in dB/km . The vertical black lines are plotted at the wavenumbers that correspond to the bottom compressional sound speed at cutoff frequencies from Equation (3.6) and represent the compressional wave branch cut at that frequency. Each modal wavenumber moves from left to right as the frequency increases, transitioning past the compressional wave branch cut at the cutoff frequency. As mode one through five pass by the branch cut, the modal attenuation drops. Thus, for a broadband signal propagating over a calcarenite bottom the component of the sound field that propagates as normal modes (i.e. not the part of the field associated with the branch line integral) should be dominated by modes that propagate at frequencies just before and just after the cutoff frequency and at angles close to the critical angle.

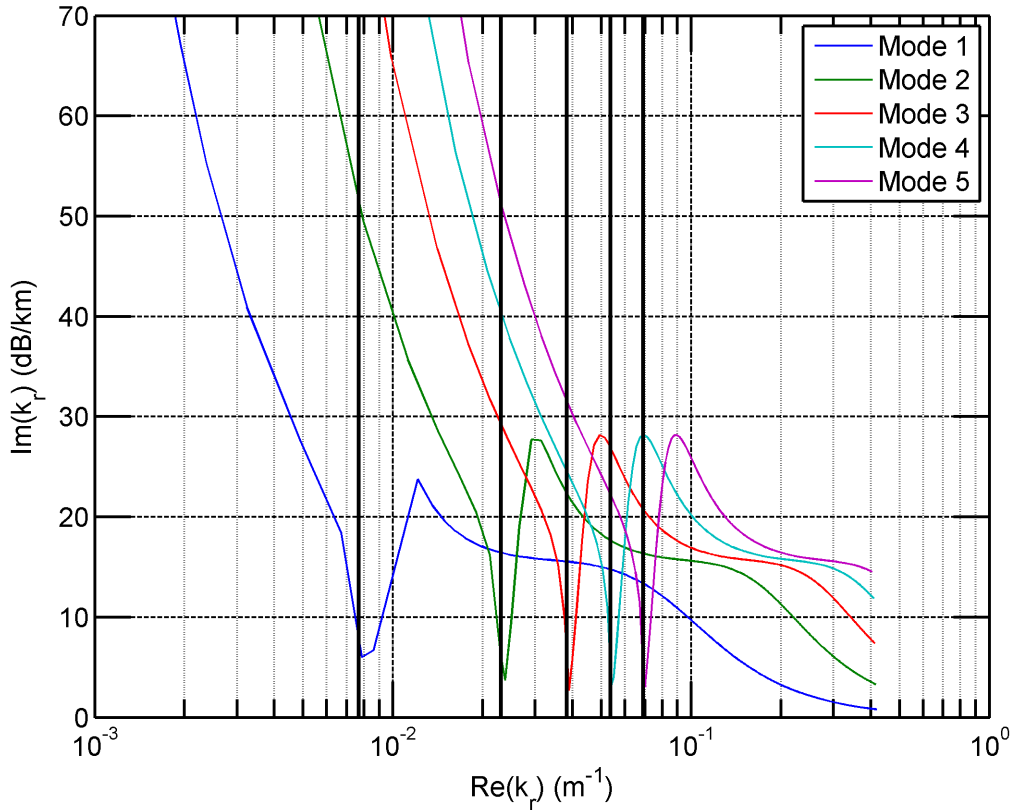


Figure 3.6: Wavenumber trajectories in the complex plane from 1 Hz to 100 Hz for the first 5 modes; low attenuating mods are found near the critical frequencies (indicated by vertical solid black lines) of the waveguide. Each mode is colour coded, blue – mode 1, green – mode 2, red – mode three, cyan – mode four, and magenta mode – five.

For a calcarenite halfspace, modes with low attenuation near the critical frequencies produce low loss peaks in broadband transmission loss. An example of this is shown below in Figure 3.7, which is an excerpt from Fan et al. (2009). This plot shows that the phenomenon of low loss peaks is present both in measured data and in those predicted by a propagation model. These peaks can be thought of as acting like a series of parallel bandpass filters, only allowing narrow bands of frequencies to propagate at the low end of the frequency range. This effect reduces at higher frequencies when attenuation is included in the bottom as shown below in Figure 3.7.

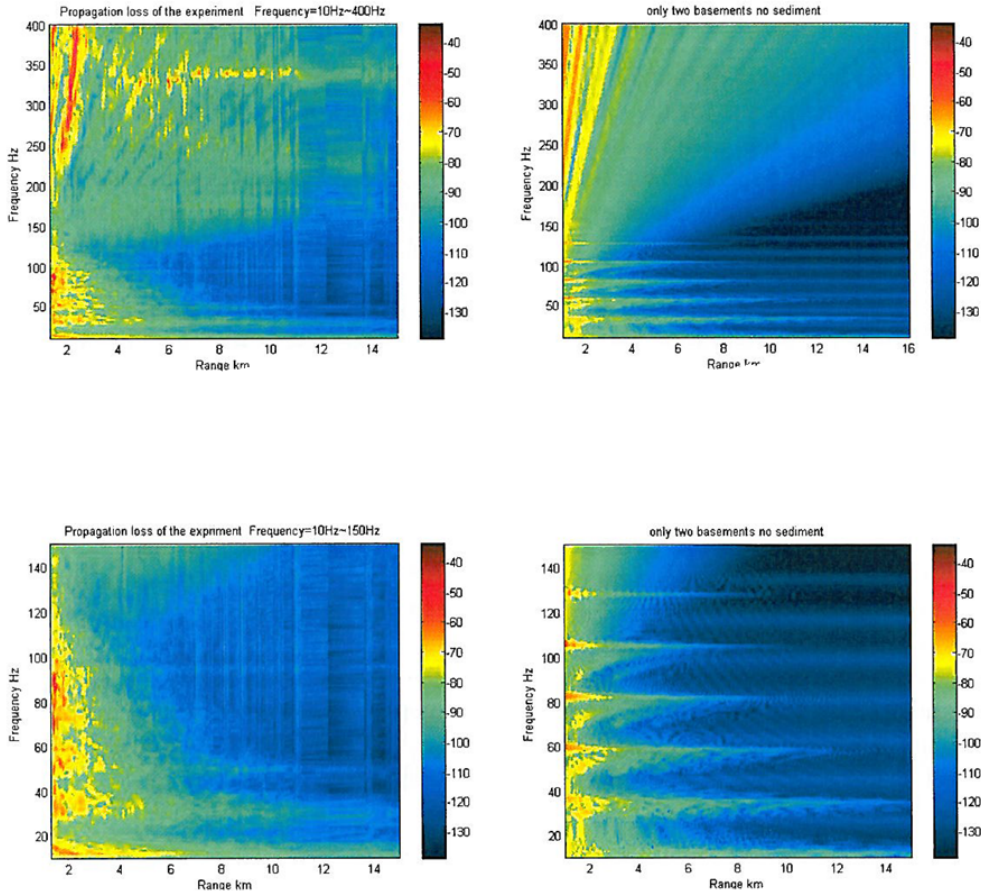


Figure 3.7: Figures excerpt from Fan et al. (2009) that show low frequency broadband transmission loss. The low loss peaks are seen near the critical frequencies in both experimental data (*left*) and model predictions (*right*).

Up to now the analysis has focused on a halfspace representation of calcarenite; however, as discussed above in Section 3.3, literature suggests that realistic seabeds contain a layered configuration of calcarenite. Using the same geoacoustic parameters from Table 3.2, the first five modes for the thin sand layer and thin cap-rock scenarios were calculated using the reflection coefficients shown in Figure 3.4 and the root finding method described in Equation (3.4). The trajectories were calculated from 1 to 100 Hz incremented at 0.25 Hz. The results are plotted in Figure 3.8 below.

Comparing these two cases, the change in modal attenuation with frequency leads to the same interpretation as the reflection coefficient analysis illustrated in Figure 3.3. The case of overlying cap-rock introduces more attenuation at higher frequencies. The overlying sand layer does not affect modal attenuation at the low end of the

frequency range but reduces attenuation at higher frequencies. This can be explained through the link between the magnitude of the reflection coefficient and the modal wavenumber attenuation described by Equation (3.3) and Equation (3.9).

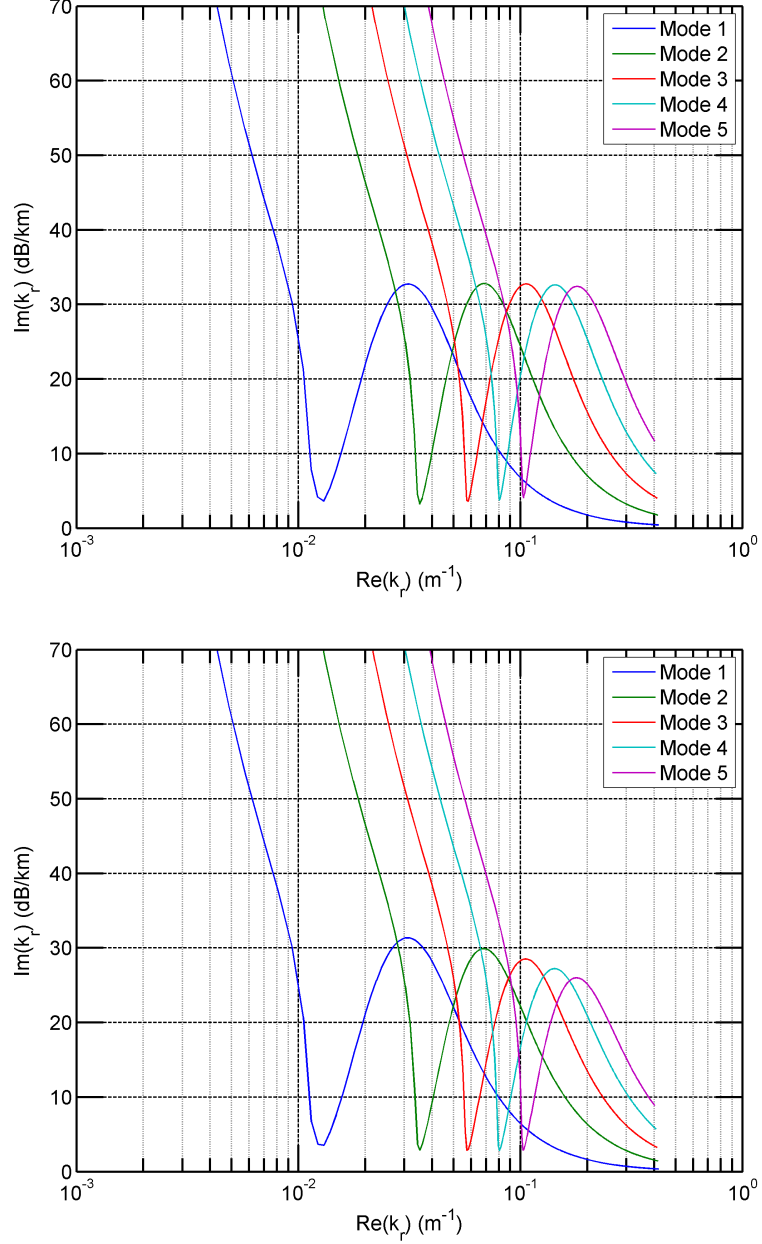


Figure 3.8: Modal wavenumber trajectories through the complex plane from 1 Hz – 100 Hz for the first 5 modes for the thin layer cases in Table 3.2. Top Panel: Cap-rock overlying semi-cemented calcarenite halfspace (Case B). Bottom Panel: Sand overlying semi-cemented calcarenite halfspace (Case C).

3.6 Summary

Section 3.2 outlines the geological setting around a large portion of Australia. The discussion is important because it describes what sort of sediment or rock may be present at the seafloor. In general calcarenite seafloors discussed here are not comparable to typical seafloor sediments from other continental shelves around the globe (Seibold & Berger, 1996; James & Bone, 2011). Section 3.3 describes the current state of the literature concerning the geoacoustic parameters of calcarenite. However, the available information and the geographic distribution of study locations are both sparse. This highlights the need for further investigation on the topic. Considering the geology and acoustic literature mentioned above, three different seafloor formations are proposed to represent the potential types of seafloor environments that are likely to be found around Southern and Western Australia. In nature, the real seabed may be composed of combinations of these seafloor formations.

The influence of these seabed types on acoustic propagation is further discussed in Section 3.4 and 3.5, with an analysis of reflection coefficient and the variation of normal mode wavenumbers with frequency. The main effect of calcarenite on the water column acoustic field is to introduce an additional energy loss mechanism for reflected waves through the conversion of acoustic energy to shear wave energy in the bottom. This effect is present whether the calcarenite is cemented or semi-cemented, layered or homogenous, and can be seen in both the reflection coefficient and wavenumber attenuations. However, around the critical frequencies individual modes propagate with low loss due to the bottom reflection near the critical grazing angle. This causes a band pass filter effect when considering reflections over a band of frequencies (Duncan et al., 2009).

The insertion of layers in the bottom introduces frequency dependence to this bandpass filter effect. Thin layers generally have a greater effect on the reflected field at higher frequencies and thick layers have a greater effect at low frequencies (Ainslie, 1995). It is the side-by-side comparison of the effects of different layered calcarenite structures has on the modal wavenumbers that has not been explicitly examined.

In general, the effect of a cap-rock layer increases bottom attenuation and as the frequency increases and the reflection coefficient becomes influenced by the shear waves in the cap-rock layer which then enhance the coupling to shear waves in the bottom halfspace (Duncan & Gavrilov, 2012). A thin sand layer has the opposite effect; it enhances reflection and reduces attenuation at higher frequencies. Both these mechanisms affect the trajectories of the normal mode wavenumbers through the complex plane as a function of frequency (Figure 3.7). For more complex modelling problems involving calcarenite seabeds, such as range dependent propagation modelling, it is important to capture the low loss peaks near critical frequencies. Moreover, range dependent models also need to be able to accurately model the broadband effects of thin and thick layers in the sub-bottom.

CHAPTER 4 Seismoacoustic Adiabatic Normal Modes

4.1 Introduction

The success of parabolic equation models to accurately predict range dependent seismoacoustic wave propagation has been documented in recent literature (Collis et al., 2008; Collins & Siegmann, 2015). However, there are some scenarios where the PE method can require long runtimes to converge to a realistic solution (Collis & Metzler, 2014). Additionally, for complex layered environments some PE codes appear to fail to converge to a physical solution (Duncan & McCauley, 2008; Duncan et al., 2009).

In this chapter, an alternative to the seismoacoustic parabolic equation propagation method is proposed. Specifically this alternative is an adiabatic seismoacoustic normal mode propagation model. The formalisation of an adiabatic seismoacoustic normal mode method is presented and its applicability to low frequency seismoacoustic range dependent wave propagation is tested. A single frequency benchmark scenario is presented as an initial validation test of the adiabatic approach.

4.2 Normal Modes for Environments with Elastic Bottoms

Range dependent propagation in purely acoustic media has been studied in detail with coupled normal modes and parabolic equations, where the equations of motion are satisfied by one scalar potential function or pressure (Jensen et al., 2011c). In contrast, the equations of motion for a 2-D seismoacoustic normal mode problem involve two different potential functions, one for compressional waves and one for shear waves (Ewing et al., 1957). Considering an ocean waveguide with a point source located in the water column, only compressional and vertically polarised shear waves (P-SV) can be excited in the seabed (Ewing et al., 1957). The term “vertically polarised shear waves” (SV waves) refers to shear waves polarised in the range-depth plane, and these waves will have both vertical and radial displacement components. P-SV propagation also describes the propagation of interface waves

such as Scholte and Stonely waves (Aki & Richards, 1980). Moreover, it has been shown that the governing equations for seismic interface waves can also be applied to seismoacoustic modal propagation of acoustic waves over a solid bottom (Jensen et al., 2011b).

A coupled-mode theory for propagating seismic waves has been formalised by Woodhouse (1974) and Kennett (1984b). Based on this, Maupin (1988) proposed a theoretical approach for mode coupling in a fluid over an elastic bottom. Maupin's solution was given in the form of a stress-displacement vector, where a vector of local modes evolves in range with continuous mode coupling coefficients. This form of the stress-displacement vector $\vec{U}(x, z; k_y; \omega)$ in Cartesian coordinates is defined as

$$\vec{U}(x, z; k_y; \omega) = \sum_m C_m^\pm(x) \vec{U}_m(z) e^{\pm i \int_0^x k_{x,m}(x') dx'} \quad (4.1)$$

where, $C_m(x)$ is the modal amplitude subject to mode coupling, and $\vec{U}(x, z; k_y; \omega)$ is in general a six element stress-displacement vector (Park and Odom, 1998). For P-SV waves the stress-displacement vector becomes

$$\vec{U}(x, z; k_y; \omega) = \begin{bmatrix} u_x(x, z) \\ 0 \\ u_z(x, z) \\ \sigma_{xx}(x, z) \\ 0 \\ \sigma_{xz}(x, z) \end{bmatrix} \quad (4.2)$$

and the modal amplitudes are defined through the differential equation governing their evolution in range,

$$\partial_x C_n(x) = B_{nm} C_m(x). \quad (4.3)$$

The coupling matrix B_{nm} is defined by Maupin (1988) and methods for calculating the matrix elements are given by Odom et al. (1996) and Park and Odom (1998). However, Odom et al. (1996) suggested that if coupling between modes were neglected, then the functional form above reduces to the adiabatic approximation. When assuming the environment is translationally invariant in the y direction and neglecting modal coupling (i.e. $B_{nm} = 0$ for $n \neq m$) then $C_m(x)$ becomes

$$C_m(x) = \frac{i\sqrt{2\pi}e^{-i\frac{\pi}{4}} C_m(0, z_s)}{\sqrt{k_{x,m}(0)k_{r,m}(x) \int_0^x \frac{1}{k_{x,m}(x')} dx'}} \quad (4.4)$$

A simple derivation of Equation (4.4) is provided in Appendix A of this thesis. The adiabatic seismoacoustic stress-displacement vector for P-SV waves can then be written as,

$$\vec{U}(x, 0, z) = \frac{i}{\sqrt{8\pi}} e^{-i\frac{\pi}{4}} \sum_m \frac{C_m(0, z_s) \vec{U}_m(x, z) e^{i \int_0^x k_{x,m}(x') dx'}}{\sqrt{k_{x,m}(0) k_{x,m}(x) \int_0^x \frac{1}{k_{x,m}(x')} dx'}} \quad (4.5)$$

where $C_m(0, z_s)$ is associated with the source excitation. Park and Odom (1998) provide the source excitations for different wave types including Love, Rayleigh, and acoustic waves. Since this form of the adiabatic approximation assumes that the environment is translationally invariant in the y direction and that the source and receiver are chosen to lie in the xz plane where $y = 0$, the x coordinate can be interchanged with the r coordinate for cylindrical geometry (Jensen et al., 2011b).

In a fluid medium this equation (4.5) can be reduced to a form similar to the Cartesian adiabatic approximation for acoustic pressure proposed by Porter (1994) and Godin (2002). Moreover, when the source is in a fluid layer above an elastic seafloor the displacement potential is given by,

$$\Phi(r, z) = \frac{\sqrt{2\pi}}{\omega^2 \rho(r, z) \rho_s} e^{i\frac{\pi}{4}} \sum_m \frac{\bar{\varphi}_m(0, z_s) \bar{\varphi}_m(r, z) e^{i \int_0^r k_{r,m}(r') dr'}}{\sqrt{k_{r,m}(0) k_{r,m}(r) \int_0^r \frac{1}{k_{r,m}(r')} dr'}} \quad (4.6)$$

Porter (1994), Godin (2002), and Jensen et al. (2011b) have all stated that this form of the adiabatic approximation satisfies the reciprocity principle of linear acoustics. If the environment is axially symmetric and cylindrical coordinates are used, another adiabatic approximation can be obtained following a similar procedure. The resultant form (Tindle & Zhang, 1997; Hall, 2004; Jensen et al., 2011b) is given by,

$$\Phi(r, z) = \frac{\sqrt{2\pi}}{\omega^2 \rho(r, z) \rho_s} e^{i\frac{\pi}{4}} \sum_m \frac{\bar{\varphi}_m(0, z_s) \bar{\varphi}_m(r, z) e^{i \int_0^r k_{r,m}(r') dr'}}{\sqrt{k_{r,m}(r)r}} \quad (4.7)$$

Since the pressure and the displacement potential in a fluid medium are related by a constant factor, either can be used to calculate the transmission loss (TL),

$$TL(r, z) = -20 \log_{10} \left(\left| \frac{P(r, z)}{P(\vec{r}_o)} \right| \right) = -20 \log_{10} \left(\left| \frac{\rho(r, z) \omega^2 \Phi(r, z)}{P(\vec{r}_o)} \right| \right) \quad (4.8)$$

where $P(\vec{r}_o)$ is a scaling term to ensure a pressure amplitude of 1 Pa at a reference range of 1 metre from the acoustic centre of the source (Jensen et al., 2011b).

4.2.1 Description of the Seismoacoustic Adiabatic Normal Mode Algorithm

The procedure to implement the seismoacoustic adiabatic normal mode method is as follows:

- The environment is divided into a number of range segments and the normalised mode functions and modal wavenumbers are computed at each segment. The normal mode program ORCA (Westwood et al., 1996) is used to perform these calculations.
- The modal wavenumbers and mode shapes are interpolated to a finer computational range grid; this is done to achieve a better spatial resolution of the field without having to re-run ORCA many times on a fine range grid.
- The range integrals in Equation (4.6) or Equation (4.7) (depending whether translational symmetry or axial symmetry is desired) are then evaluated by trapezoidal integration. The pressure can then be calculated by summing up the mode functions in Equation (4.6) or Equation (4.7). The displacements in cylindrical coordinates can be computed from Equations (2.10) and (2.11) and the stresses in cylindrical coordinates from Equation (2.19), Equation (2.20) and Equation (2.21). The Cartesian equivalents can be found in Hovem (2012).
- The transmission loss can then be computed by evaluating Equation (4.8).

This propagation model is further referred to as SANMO, for Seismoacoustic Adiabatic Normal Modes with ORCA, and was developed in Matlab. It should be noted that this is not the first model to use adiabatic mode propagation theory with ORCA. The program AMBO (Adiabatic Modes Based on Orca) that was developed by Hall (2004) follows a similar approach. The key differences between AMBO and SANMO are, firstly the option to choose the form of the adiabatic approximation, and secondly the ability to compute displacements and stresses. The adiabatic forms used by AMBO and SANMO are shown in Equation (4.9)

$$\text{AMBO} \rightarrow \frac{e^{i \int_0^r k_{r,m}(r') dr'}}{\sqrt{k_{r,m}(r)r}} \quad (4.9)$$

$$\text{SANMO} \rightarrow \frac{e^{i \int_0^r k_{r,m}(r') dr'}}{\sqrt{k_{r,m}(r)r}} \text{ or } \frac{e^{i \int_0^r k_{r,m}(r') dr'}}{\sqrt{k_{r,m}(0)k_{r,m}(r) \int_0^r \frac{1}{k_{r,m}(r')} dr'}}.$$

The form used by AMBO does not fully satisfy the principle of reciprocity because there is no dependence of $k_{r,m}(0)$ (i.e. the wavenumber at the source) in the denominator (Porter, 1994; Jensen et al., 2011b), whereas the second form used by SANMO does include this dependence. When this second form is used to compute transmission loss in Cartesian coordinates, the result is reciprocal as a consequence of the environment being translationally invariant; however, this is not the case for axially symmetric propagation in cylindrical coordinates. For the benchmarking exercises below the axially symmetric, non-reciprocal form is used. The reciprocal form becomes important when measured data are considered, and is used in Chapter 5.

4.3 Numerical Examples of Single Frequency Benchmarks

In order to evaluate the performance of the seismoacoustic adiabatic mode method, a benchmarking exercise was conducted. The benchmarking process of numerical methods ensures consistency between numerical models and in the absence of precise laboratory data, benchmarking can be used as an initial validation of a model's performance. Extensive work has been conducted on the benchmarking of range dependent acoustic problems (Jensen & Ferla, 1990). For seismoacoustic problems, an initial list of benchmarks has been discussed by Chin-Bing et al. (1993) and Goh et al. (1997). It has also been noted that further benchmarking exercises of seismoacoustic propagation models should be conducted in a similar fashion to acoustic models (Collins & Siegmann, 2015).

4.3.1 Acoustical Society of America's (ASA) Elastic Wedge

The Acoustical Society of America's (ASA) elastic wedge (Chin-Bing et al., 1993) is a standard benchmark for range dependent acoustic propagation in a fluid over an elastic bottom. A variety of wedge scenarios were initially considered by Collins (1989b) and a formal benchmark was presented at the Acoustical Society of America's (ASA's) second parabolic equations workshop (Chin-Bing et al., 1993). Cylindrical coordinates are used for the elastic wedge and the environment is axially symmetric; therefore, the corresponding axially symmetric cylindrical coordinate adiabatic form is used by SANMO. The wedge environment is significant because it

is analogous to many real world problems that are encountered in underwater acoustic propagation modelling. The propagation phenomena associated with the wedge are comparable to underwater sound propagation either up or down the continental slope.

The geoacoustic parameters for the ASA's elastic wedge model are presented in Table 4.1.

Table 4.1: Geoacoustic properties for the ASA Elastic Wedge proposed by (Chin-Bing et al., 1993) at the ASA's second parabolic equations workshop

Layer Type	ρ (g/cm ³)	c_p (m/s)	c_s (m/s)	α_p (dB/λ)	α_s (dB/λ)
Water	1.0	1500	0.0	0.0	0.0
Sediment	1.5	1700	800	0.5	0.5

For the validation test of SANMO, three scenarios were considered that are variations on the ASA elastic wedge model. These included scenarios that correspond to propagation over a flat bottom (FLAT), propagation over an up sloping bottom (UP), and propagation over a down sloping bottom (DOWN). The frequency, bathymetry variations (H), source depth (z_s), and receiver depth (z_{rx}) for each case are summarised in Table 4.2.

Table 4.2: Propagation model parameters for three benchmark cases of SANMO

Case	Frequency (Hz)	H (r = 0 km) (m)	H (r = 3.5 km) (m)	z_s (m)	z_{rx} (m)
FLAT	25.0	200.0	200.0	100.0	30.0
UP	25.0	200.0	25.0	100.0	30.0
DOWN	25.0	50.0	225.0	25.0	30.0

4.3.2 Range Independent Benchmarking Results (FLAT)

The first validation test considers a purely flat waveguide. The FLAT scenario has a water depth of 200 metres and a point source at a depth of 100 metres. For this

scenario, SANMO was compared to three different propagation models. These models included two range dependent (RD) models and a range independent (RI) model. A list of the propagation models and their literature references is provided in Table 4.3. For the FLAT case OASES is considered to be the authoritative propagation model.

Table 4.3: References for the propagation models used for benchmark comparisons of the adiabatic seismoacoustic normal mode method.

Propagation Model Name (Method)	Literature Citation
OASES (Wavenumber Integration - RI)	(Schmidt & Tango, 1986)
LAYROTVARS (Parabolic Equation - RD)	(Collis et al., 2008)
RAMSGEO (Parabolic Equation - RD)	(Collins, 1993a)

As shown in Figure 4.1 at a receiver depth of 30 metres OASES and SANMO produce a very similar transmission loss prediction.

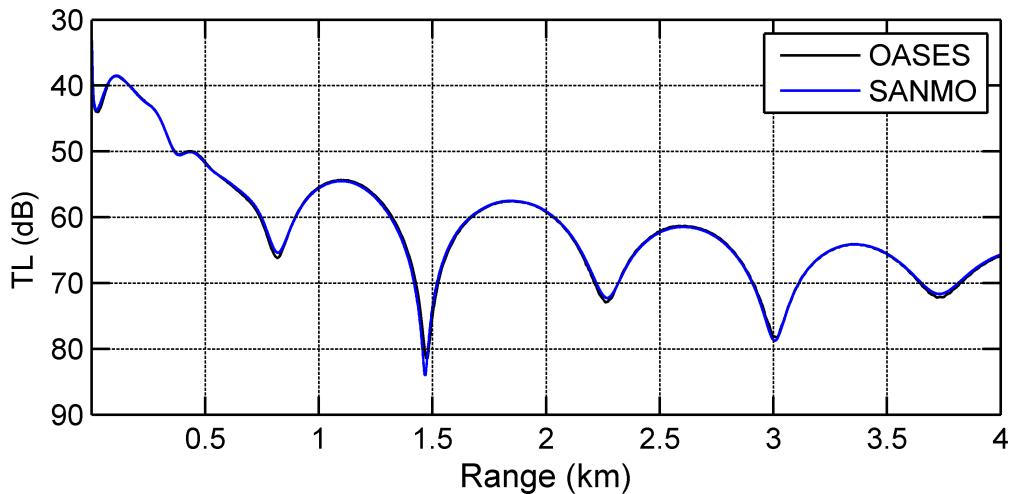


Figure 4.1: Transmission loss (TL) at a depth of 30 metres for the flat bottom waveguide (FLAT) validation scenario predicted using propagation models OASES as benchmarks for SANMO.

Each propagation model outputs transmission loss based on the acoustic pressure when a receiver is in the water column; however, when a receiver is placed in the seabed, which is elastic, several quantities can be compared. OASES has the option to output transmission loss based on the normal seismic stresses, (σ_{zz} and/or σ_{rr}) and

particle velocities (v_z and/or v_r) (Schmidt, 2004). These quantities from OASES were compared to SANMO for a receiver at 230 metres depth, 30 metres below the seafloor interface. The particle velocity can be obtained from the displacements by,

$$\vec{v} = j \omega \vec{u}, \quad (4.10)$$

which can be used to produce the vertical and horizontal velocities v_z and v_r . Equation (4.10) is the frequency domain equivalent of a time derivative. The displacements are related to the potential functions in Equation (2.10) and Equation (2.11) and the stresses are related to the displacements in Equation (2.19) and Equation (2.21). Figure 4.2 shows the stresses and velocities from OASES compared to those produced by SANMO when a halfspace representation of the bottom is used.

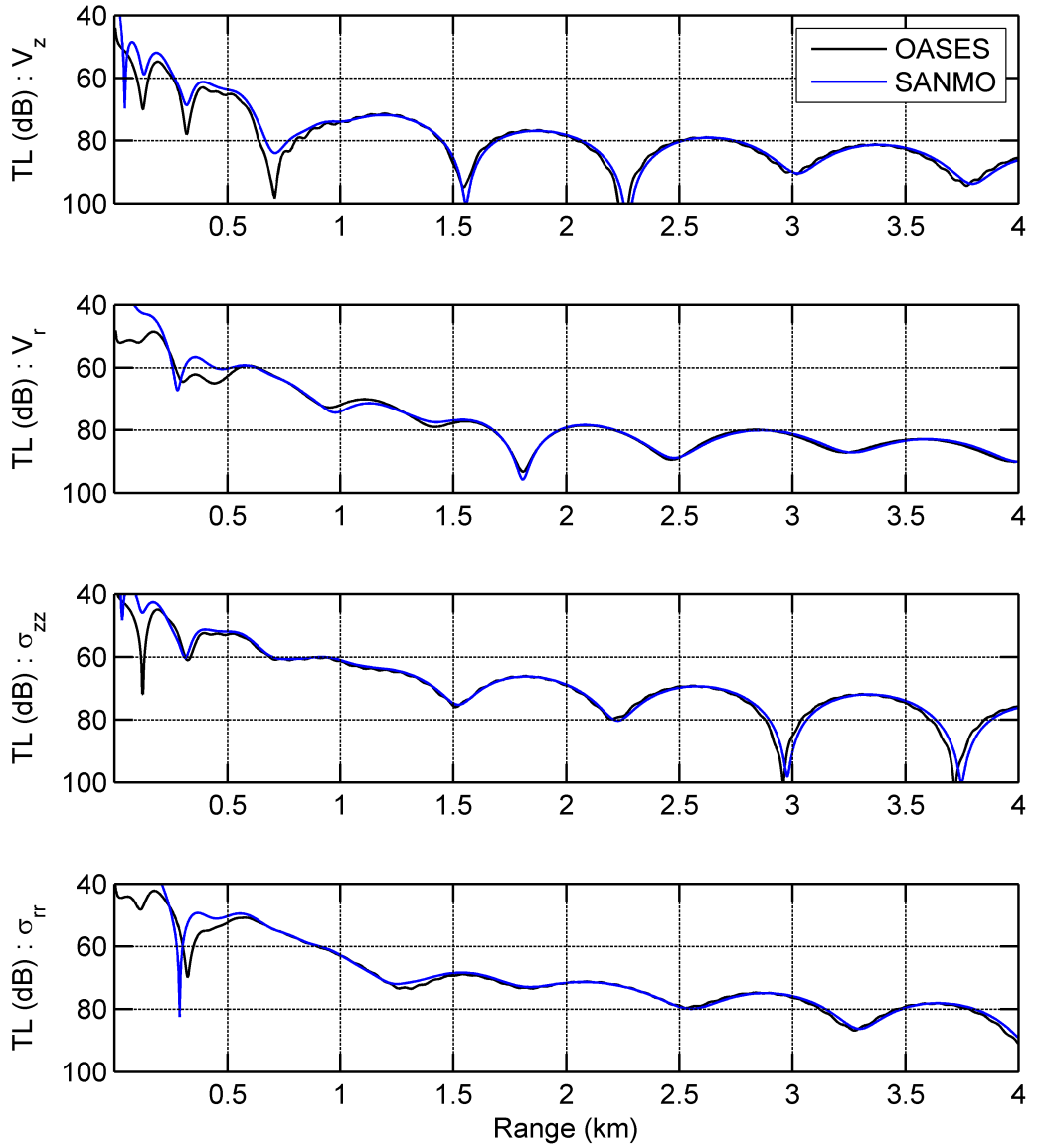


Figure 4.2: Transmission loss comparison between OASES and SANMO at receiver depth of 230 metres. The panels starting from the top shows the transmission loss from vertical and horizontal particle velocities and vertical and horizontal normal seismic stresses.

A consequence of using a halfspace representation and the Pekeris branch cut is that leaky modes are required to represent components of the seismoacoustic field that propagate at steep grazing angles. These leaky modes do not decay with depth but grow in amplitude in the halfspace. Figure 4.3 illustrates this by showing $\bar{\varphi}_m(z)$ for mode 4, the first leaky mode for this environment.

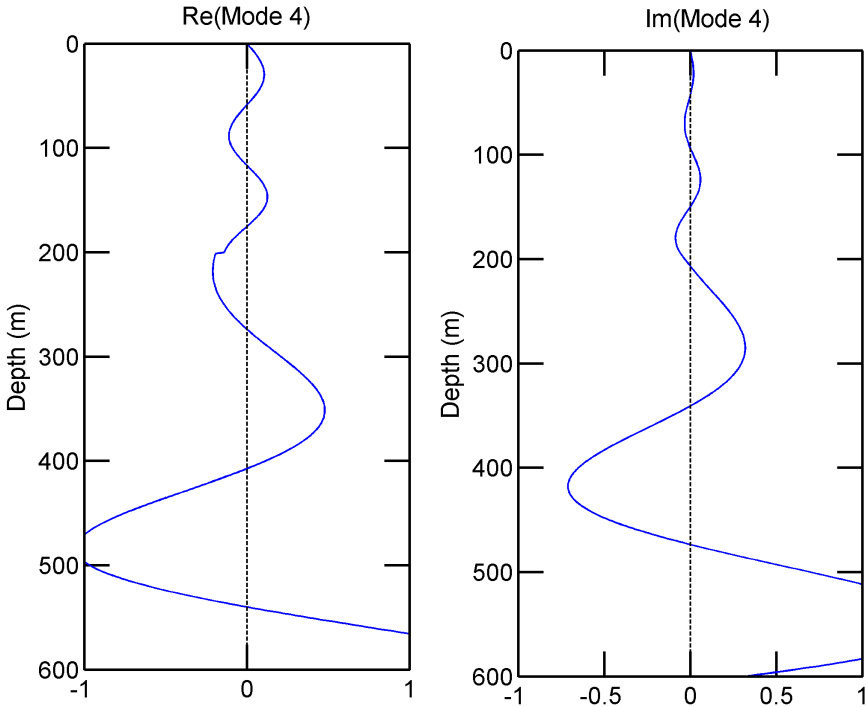


Figure 4.3: The real (*Left Panel*) and imaginary (*Right Panel*) parts of the mode function for mode 4.

There is a discontinuous jump in the compressional mode function at 200 metres depth because of the fluid-elastic interface at the seabed. It is the vertical displacement and vertical normal stress that are continuous at a flat fluid-elastic interface, both of which include contributions from the shear mode functions as discussed in section 2.3.1. The discontinuity is more pronounced in the real part of the mode function but there is also a very small discontinuity in the imaginary part of the compressional mode function, which is not visible on the plot. Generally the inclusion of leaky modes in the modal summation produces a more accurate solution in the near field rather than just including trapped modes in the modal summation. Even though leaky modes are included here, there are still some discrepancies between SANMO and OASES especially when a receiver is in the bottom. Neglecting the BLI when computing the seismoacoustic field likely causes this discrepancy.

Most PE models do not use a halfspace representation below the lower most interface of interest, rather they use a false bottom layer over the top of a pressure or stress release interface as an artificial representation of the bottom halfspace (Jensen

et al., 2011c). Here, the false bottom used by RAMSGEO and LAYROTVARS consists of two layers: a layer with the same geoacoustic properties as the original halfspace and a second layer with the same properties except the compressional and shear attenuations have both been increased to $10 \text{ dB}/\lambda$. The first layer is 15 wavelengths thick and the second layer is 10 wavelengths thick. These two layers that together compose the false bottom are inserted above a stress release surface at the very bottom of the PE's computational grid. Figure 4.4 shows a schematic of the false bottom configuration.

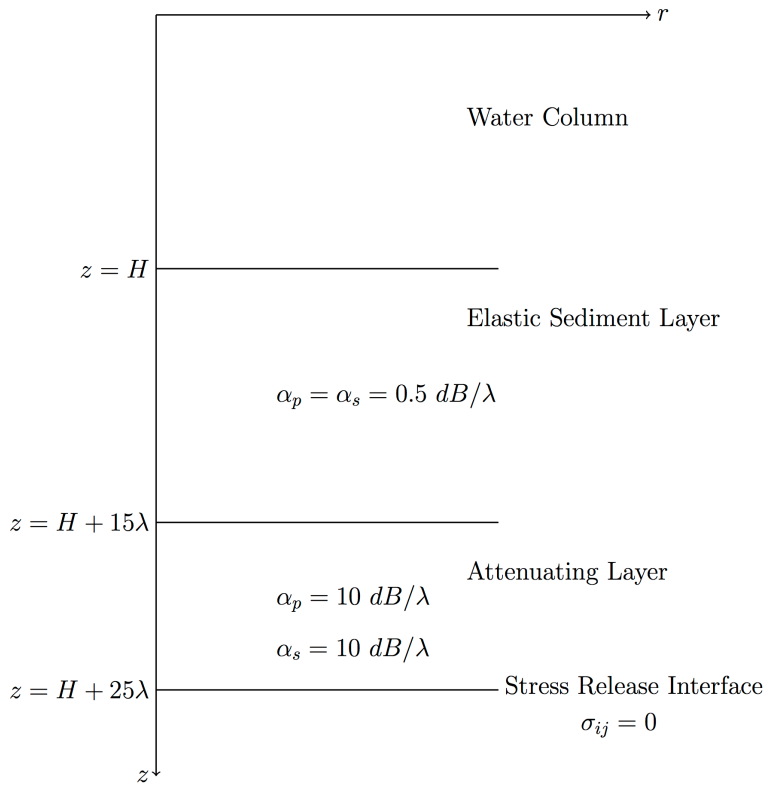


Figure 4.4: A schematic for the false bottom configuration used by all the propagation models for the FLAT case.

For consistency when comparing the output of SANMO and OASES to that of the PE models the same false bottom was inserted in their environments. When considering a receiver located in the elastic bottom and comparing OASES, SANMO, and the two PE models, transmission loss based on the bulk pressure was used. The bulk pressure is another output option from OASES (Schmidt, 2004) and in an elastic material the bulk pressure is only related to the displacement potential through Equation (2.5). The transmission loss outputted by the two seismoacoustic

PE models when a receiver is in the seabed is calculated using the far-field dilatation (Collis et al., 2009) and can be related to the displacement potential or the pressure by,

$$\frac{\rho c_p^2 \Delta}{2} = \frac{\rho c_p^2}{2} (-k_p^2 \Phi) = -\frac{\rho \omega^2 \Phi}{2} = -\frac{P}{2}. \quad (4.11)$$

To facilitate a comparison with OASES and SANMO for receivers in the seabed, the transmission loss from the PE models was adjusted to account for the one half factor in Equation (4.11). For receivers in the seabed, the transmission loss shown in Figure 4.5, Figure 4.6, and Figure 4.7 was computed from the bulk pressure.

Figure 4.5 shows the results from all four models, the transmission loss in the top panel is shown when a receiver is at a depth of 30 metres and the bulk pressure transmission loss is shown in the bottom panel for a receiver at a depth 230 metres. The models are in very good agreement when comparing the transmission loss in the water and the transmission loss in the seabed.

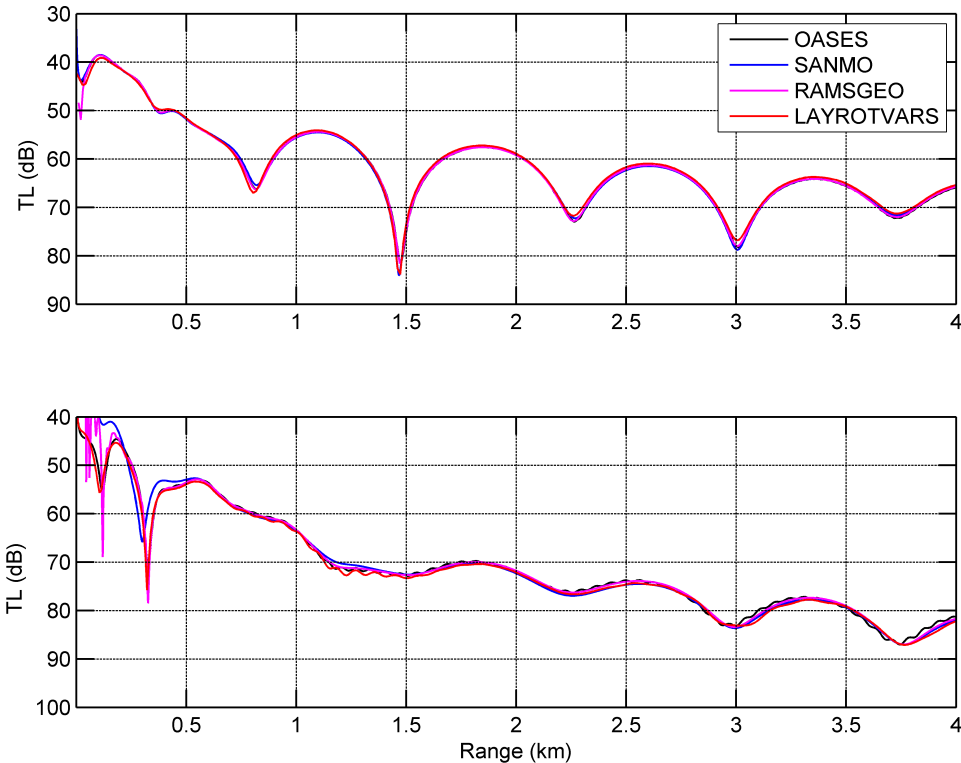


Figure 4.5: Top Panel: Transmission loss at a depth of 30 metres for the flat bottom waveguide (FLAT) validation scenario predicted using propagation models, OASES as benchmarks for LAYROTVARS, RAMSGEO, and SANMO. **Bottom Panel:** Transmission loss at a depth of 230 metres for the flat bottom waveguide (FLAT) validation scenario.

The colour plots in Figure 4.6 show a cross-section of the transmission loss outputted by each propagation model when a false bottom is included. The bulk pressure is used for transmission loss when a receiver is located in an elastic material.

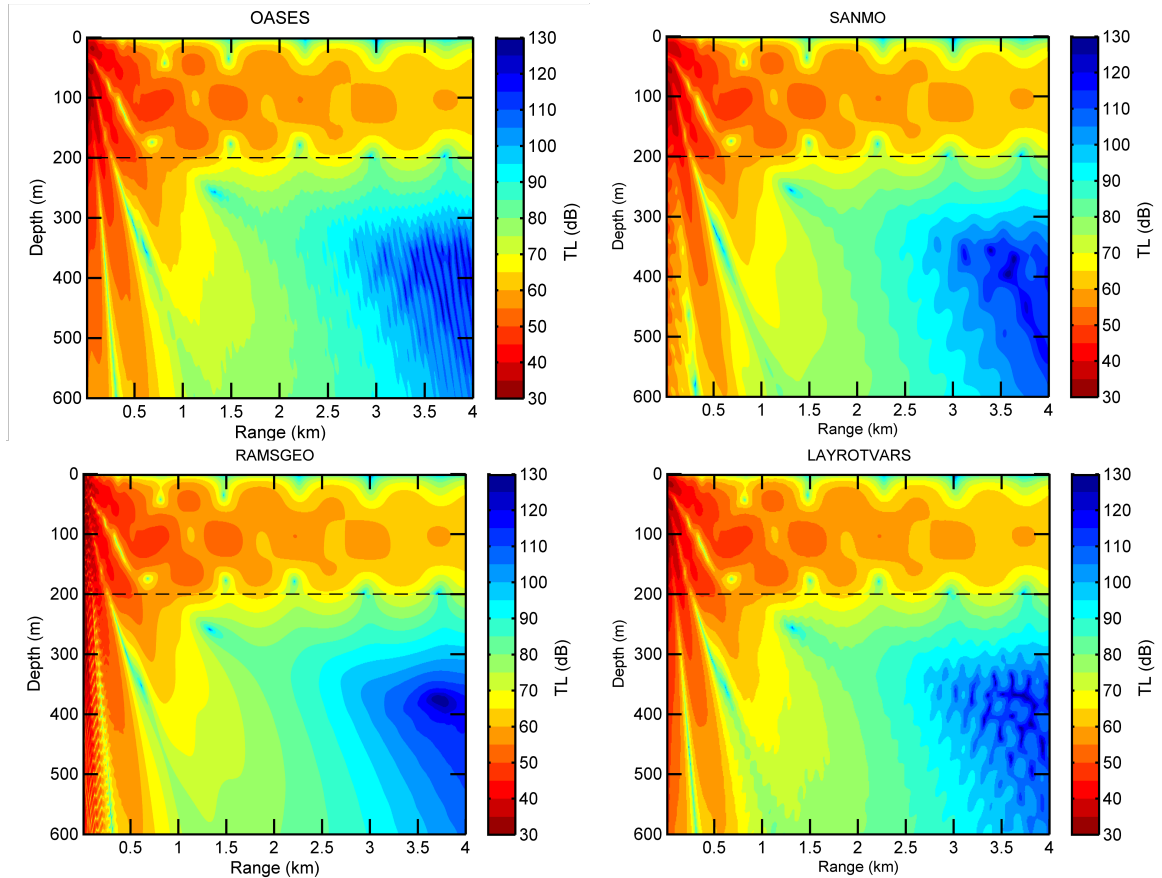


Figure 4.6: Cross-section of TL for the FLAT case with a false bottom.

While there are differences in the transmission loss predictions between the models when compared to each other and when compared to SANMO, generally the differences in the transmission loss are larger in the elastic bottom than in the water column. Overall each model produces a very similar result to the reference model OASES. The important observation is that all the models produce very consistent transmission loss results for a receiver in the fluid. When a false bottom is used, SANMO provides a consistent result when a receiver is located in the elastic sediment when compared to OASES and the PE models.

It should be noted that without a false bottom SANMO does not produce as consistent of a result when compared to OASES. A cross-section of transmission loss is shown for OASES and SANMO below in Figure 4.7; again the bulk pressure is used for the transmission loss in the seabed. In this figure a halfspace representation was used for seabed. The discrepancies are larger for deep receivers located in the elastic seabed and at short ranges near the source. This disagreement is likely due to neglecting the branch line integral in the modal sum for SANMO. Furthermore, this result supports the observation above that using a false bottom adequately represents the branch line portion of the field in the elastic seabed.

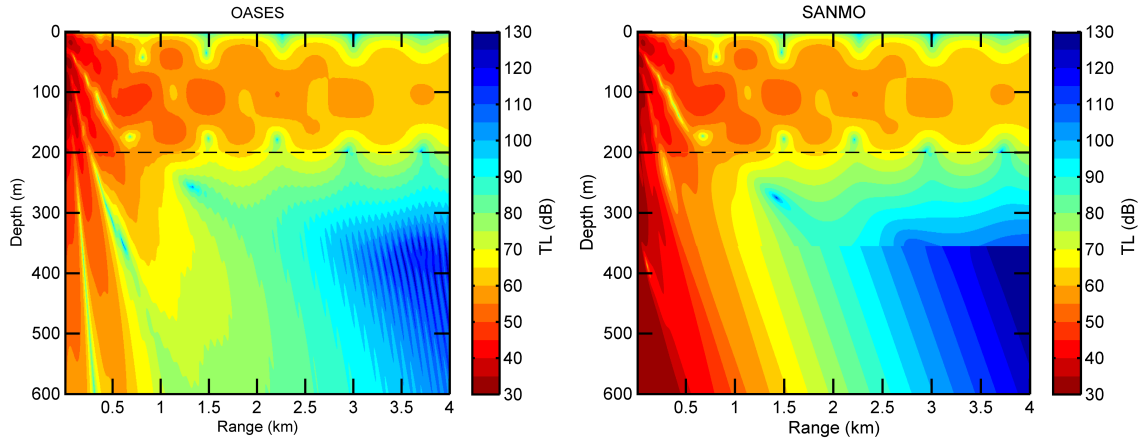


Figure 4.7: Cross-sections of TL for the FLAT case with a halfspace representation of the seabed.

4.3.3 Range Dependent Benchmarking Results (UP)

The next two sections consider range dependent scenarios; therefore transmission loss from OASES is not considered. Moreover, the rotated coordinate single-scatter seismoacoustic PE model LATYROTVARS is considered as the authoritative solution for the range dependent benchmark cases presented here. LAYROTVARS is considered to be authoritative because it has been shown to provide accurate results (Collis et al., 2007) and is based on a single-scatter, rotated coordinate method (Collis et al., 2008) to handle range dependence, which theoretically provides a more accurate solution than the approximate energy correction used by RAMSGEO (Collins, 1993a). Furthermore, since only comparisons with PE models are considered in the remainder of this chapter and this thesis, transmission loss will only be denoted as TL with the understanding that, when a receiver is in a fluid, then

the transmission loss is based on pressure and Equation (4.8) is used; whereas if a receiver is in an elastic material then the quantity in Equation (4.11) is used to compute the transmission loss.

The second validation test, UP, considers upslope propagation. At a frequency of 25 Hz, the waveguide at the source contains 3 propagating modes. As the water depth decreases, the normal modes that are initially trapped in the water column start to leak into the bottom. At 3.5 kilometres the waveguide is 25 metres thick and only mode one propagates. Tindle and Zhang (1997) have successfully benchmarked the adiabatic normal mode method for the elastic wedge when a receiver is in the water column; however, they did not consider the field in the elastic bottom. When using a halfspace representation of the bottom and neglecting the branch line integral the transmission loss predictions for receivers deep in the bottom can be erroneous, as seen in Figure 4.7. In an attempt to determine whether better agreement can be achieved, a false bottom was also used with SANMO for the UP case; this was the same false bottom as that used for the PE models. Figure 4.8 shows a slice of transmission loss from SANMO, LAYROTVARS, and RAMSGEO at a receiver depth of 30 metres along with the difference in dB between SANMO relative to LAYROTVARS (red curve) and RAMSGEO (magenta curve). Notable differences are seen when a trapped propagating mode transitions into the seabed at ranges of approximately 0.7 kilometres and 1.2 kilometres for mode 3 and mode 2 respectively. The differences around the mode cut-off are about 6 dB. There are also differences at longer ranges beyond 3 kilometres when only mode one propagates.

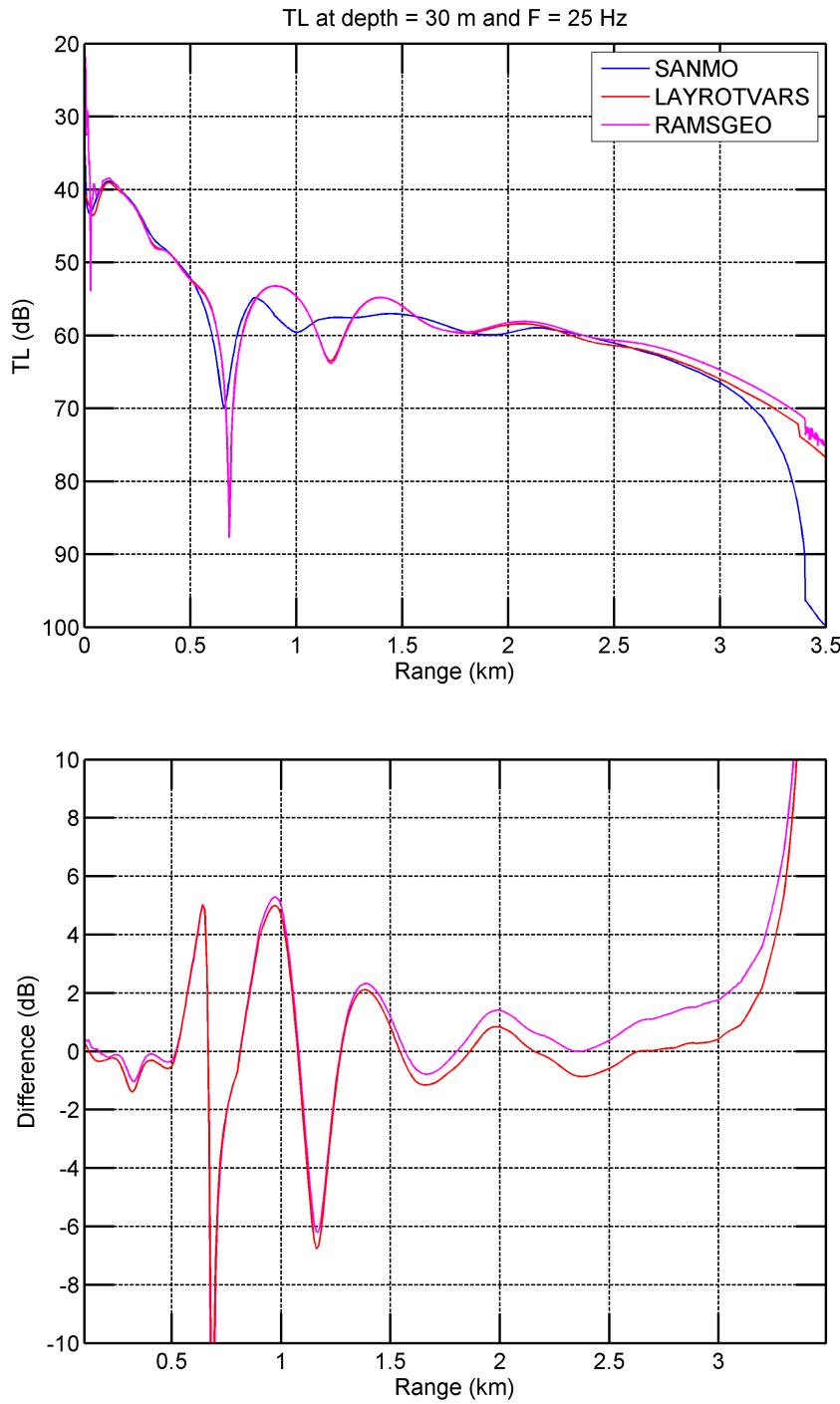


Figure 4.8: (Top Panel) Transmission loss slice at a receiver depth of 30 metres for the upslope (UP) validation scenario with a false bottom using propagation models LAYROTVARS and RAMSGEO as benchmarks for SANMO. **(Bottom Panel)** Difference between SANMO and LAYROTVARS (red curve) and SANMO and RAMSGEO (magenta curve) at a receiver depth of 30 metres as a function of range from the source.

The transmission loss colour cross-section in Figure 4.9 shows that the agreement is good at shorter ranges between 0.0 and 0.7 kilometres, but the transmission loss

output by SANMO diverges from the PE results at mid-ranges where mode 3 and mode 2 transition into the bottom. It is clear from the colour cross-section plots of the transmission loss that the field outputted by SANMO in the water column and in the bottom is inconsistent with the PE predictions.

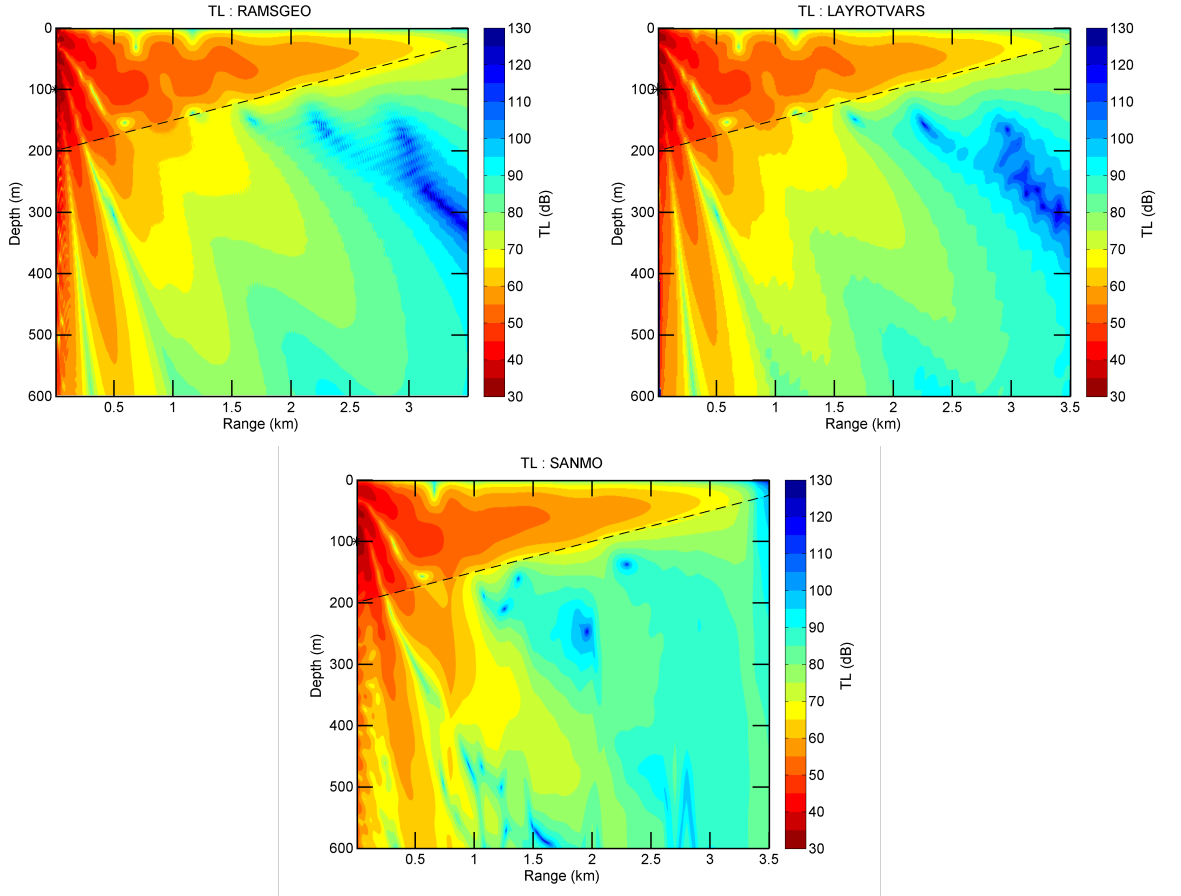


Figure 4.9: Cross-section of TL for the UP case with a false bottom.

4.3.3.1 An Elastic Airy Halfspace for Up Slope Propagation

Since inserting a false bottom into the upslope wedge environment results in a poorer agreement of SANMO with the PE models, another technique for modelling the elastic seabed of the wedge environment was tested. An Airy halfspace with a gradient in the attenuation was used to produce the transmission loss in Figure 4.11. Westwood and Koch (1998) proposed the use of a n^2 linear gradient in the compressional wave speed as a function of depth in the bottom halfspace to facilitate the use of Airy functions to represent the field in the halfspace rather than exponential function. Here, n^2 refers to the squared index of refraction. Since

attenuation is added as an imaginary part of the wave speed, Westwood and Koch (1998) used a gradient in attenuation (but not the real part of the wave speed) to eliminate the discontinuous transition of modal eigenvalues past the branch line as frequencies increased or decreased. As discussed in Chapter 2 transition of a mode past the branch cut can occur when changing the water depth or the frequency so Westwood and Koch (1998) suggested that the Airy halfspace technique may also be useful for modelling range dependent scenarios with elastic bottoms.

The gradient is defined by the difference in attenuation ($\Delta\alpha$) between the seafloor interface and a depth of three wavelengths below the interface. In ORCA, the gradient is specified by the quantity $\bar{\alpha} = \frac{\Delta\alpha}{40\pi \log_{10} e}$, which is then used to calculate the shear and compressional wave attenuation gradients. Inserting an Airy halfspace is a built-in option in ORCA and only requires the definition of the attenuation gradient, a value of $\bar{\alpha} = 0.1$ was used for the UP case. Figure 4.10 shows a schematic of the attenuating Airy halfspace configuration.

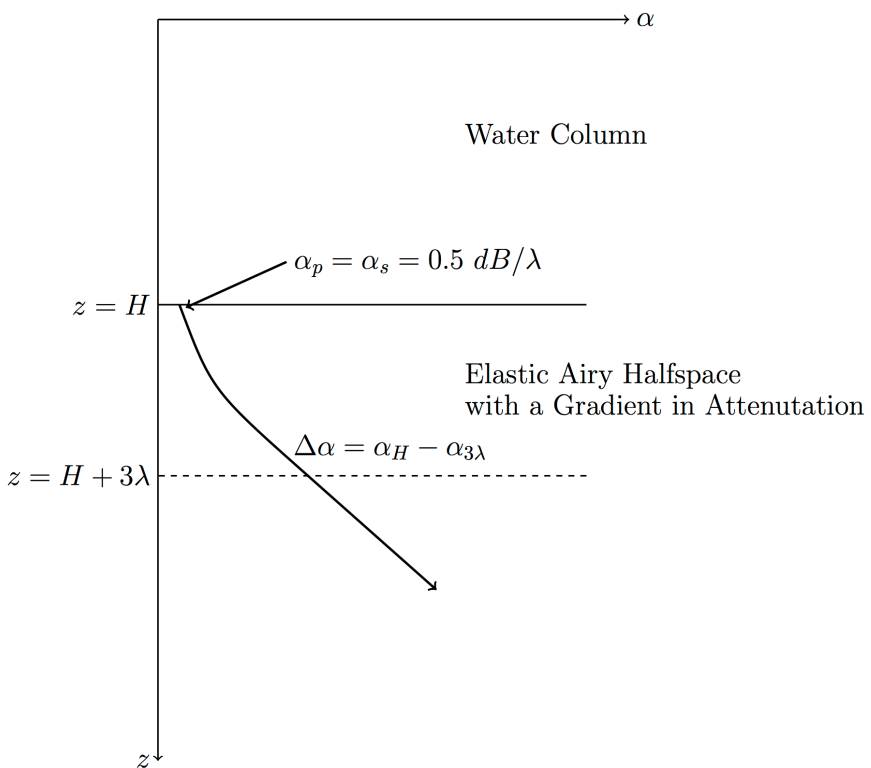


Figure 4.10: A schematic for the attenuating Airy halfspace configuration used by SANMO.

With the Airy halfspace added, the transmission loss from SANMO at a receiver depth of 30 metres is in good agreement with the PE predictions. This is shown in Figure 4.11. The differences are much smaller than the false bottom case. Figure 4.12 shows cross-section of TL produced by LAYROTVARS, RAMSGEO, SANMO using a standard halfspace representation of the bottom, and SANMO using an Airy halfspace representation of the bottom. The Airy halfspace allows for a much smoother transition of modes from trapped modes to leaky modes as the water depth decreases. While there are still disagreements in the transmission loss values between the PE models and SANMO in the bottom, the main upslope propagation effects in the water column are maintained for both types of halfspace.

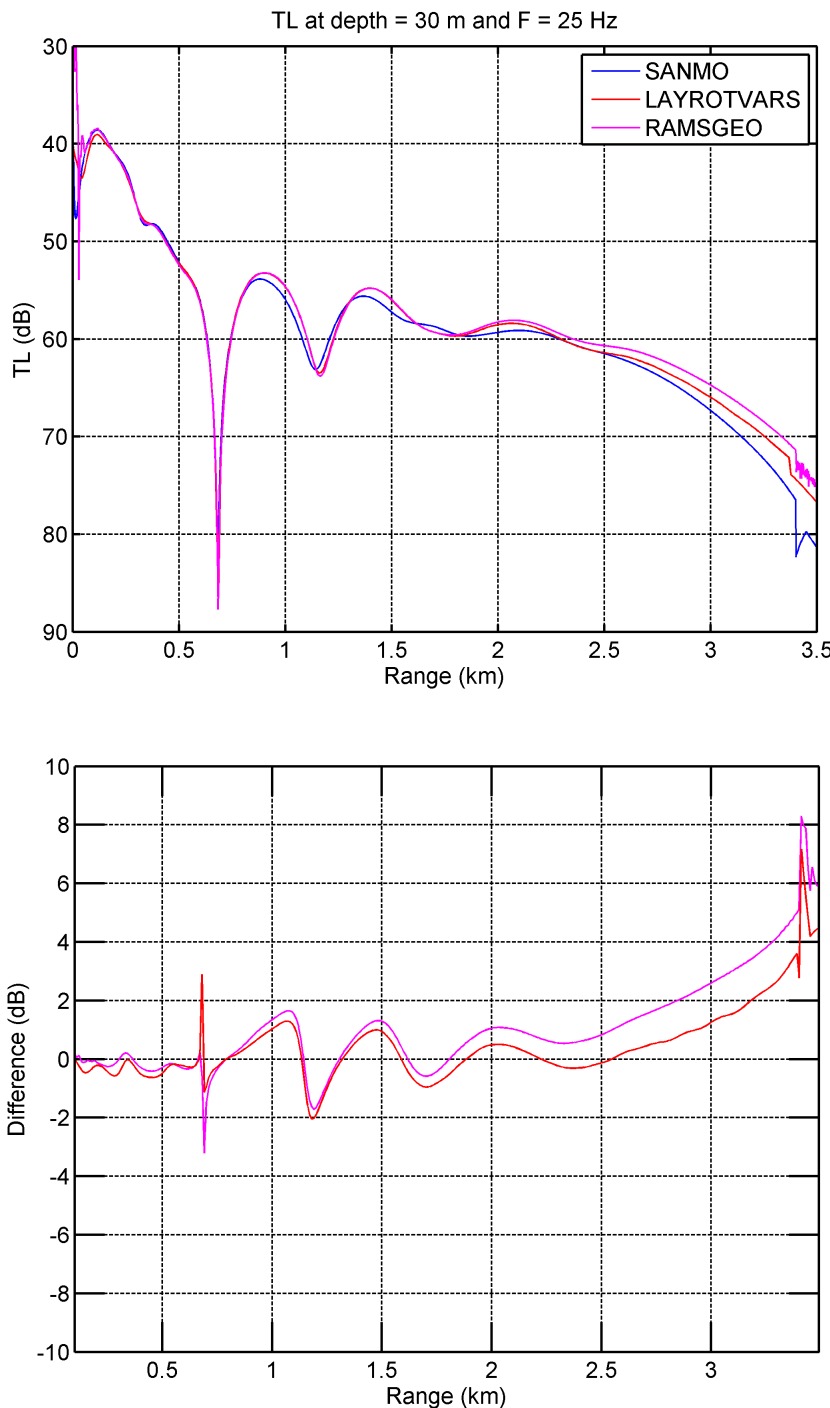


Figure 4.11: (Top Panel) Transmission loss slice at a receiver depth of 30 metres for the upslope (UP) validation scenario with an attenuating Airy halfspace using propagation models LAYROTVARS and RAMSGEO as benchmarks for SANMO. **(Bottom Panel)** Difference between SANMO and LAYROTVARS (red curve) and SANMO and RAMSGEO (magenta curve) at a receiver depth of 30 metres as a function of range from the source.

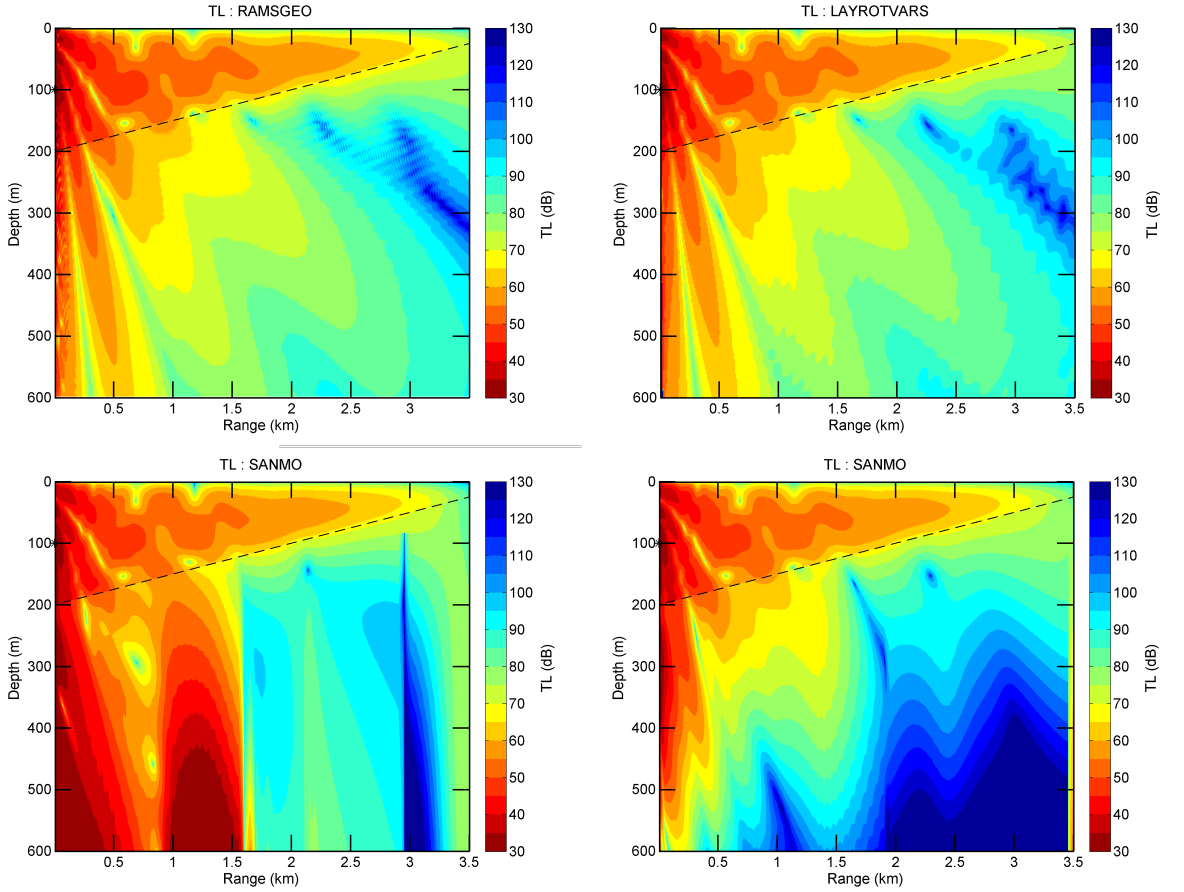


Figure 4.12: Cross-sections of TL for the UP case showing PE results (*Top Panels*), SANMO’s results with standard halfspace representation of the bottom (*Bottom Left Panel*), and SANMO’s results with an attenuating Airy halfspace (*Bottom Right Panel*).

4.3.4 Range Dependent Benchmarking Results (DOWN)

For the downslope propagation case SANMO was run with the same attenuating Airy halfspace seabed. The source depth was changed to 25 metres, which is in the middle of a waveguide that is initially 50 metres thick. For the downslope environment, the water depth increased from 50 metres depth to 225 metres at 3.5 kilometres. This ensures that the slope angle is the same as in the UP case. As the water depth increases, the normal modes transition from leaking modes to trapped modes. Plots in Figure 4.13 and Figure 4.14 show line plots and colour cross-section plots of transmission loss for SANMO, RAMS GEO, and LAYROTVARS in the same order to the UP case.

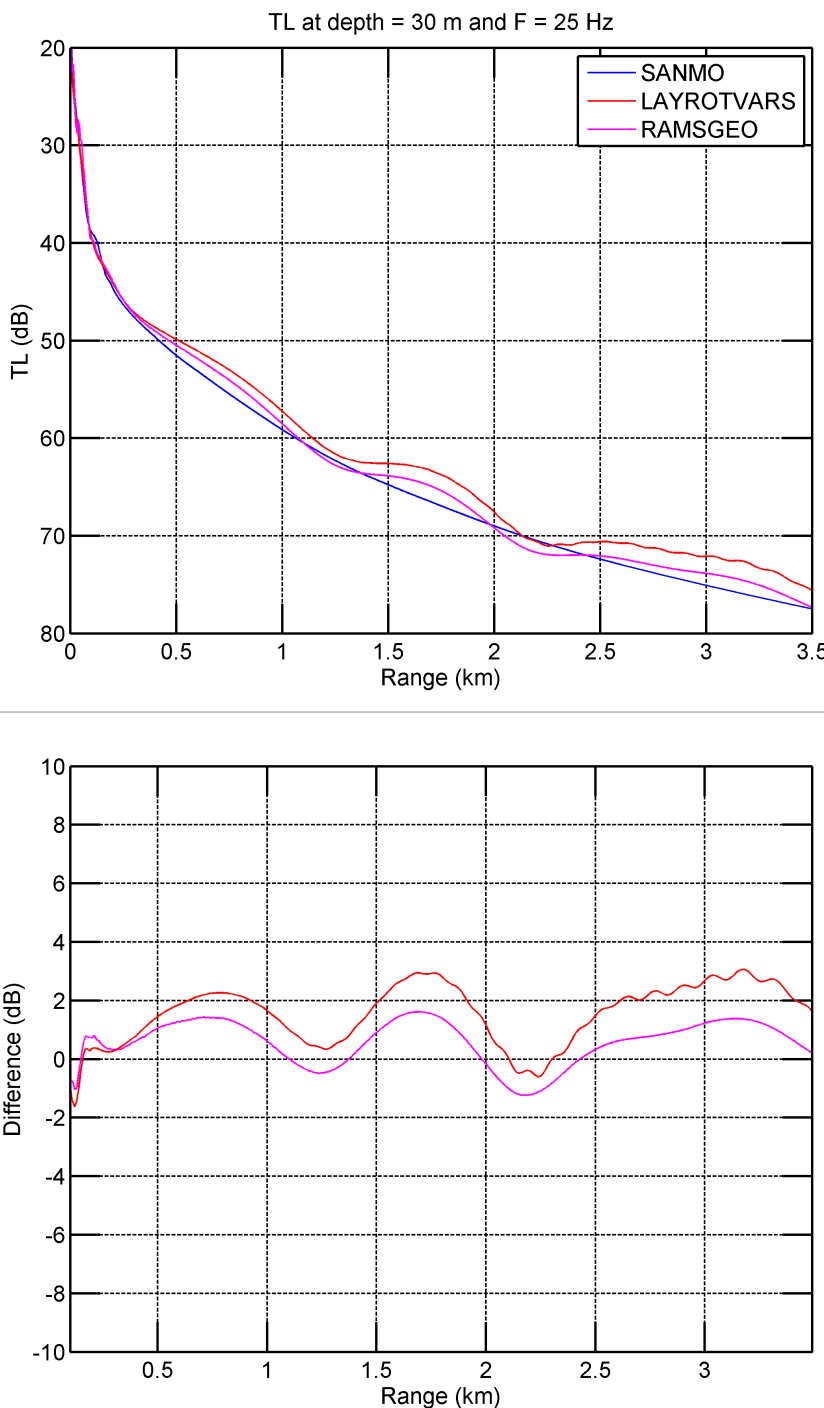


Figure 4.13: (Top Panel) Transmission loss slice at a receiver depth of 30 metres for the downslope (DOWN) validation scenario with an attenuating Airy halfspace using propagation models LAYROTVARS and RAMSGEO as benchmarks for SANMO. **(Bottom Panel)** Difference between SANMO and LAYROTVARS (red curve) and SANMO and RAMSGEO (magenta curve) at a receiver depth of 30 metres as a function of range from the source.

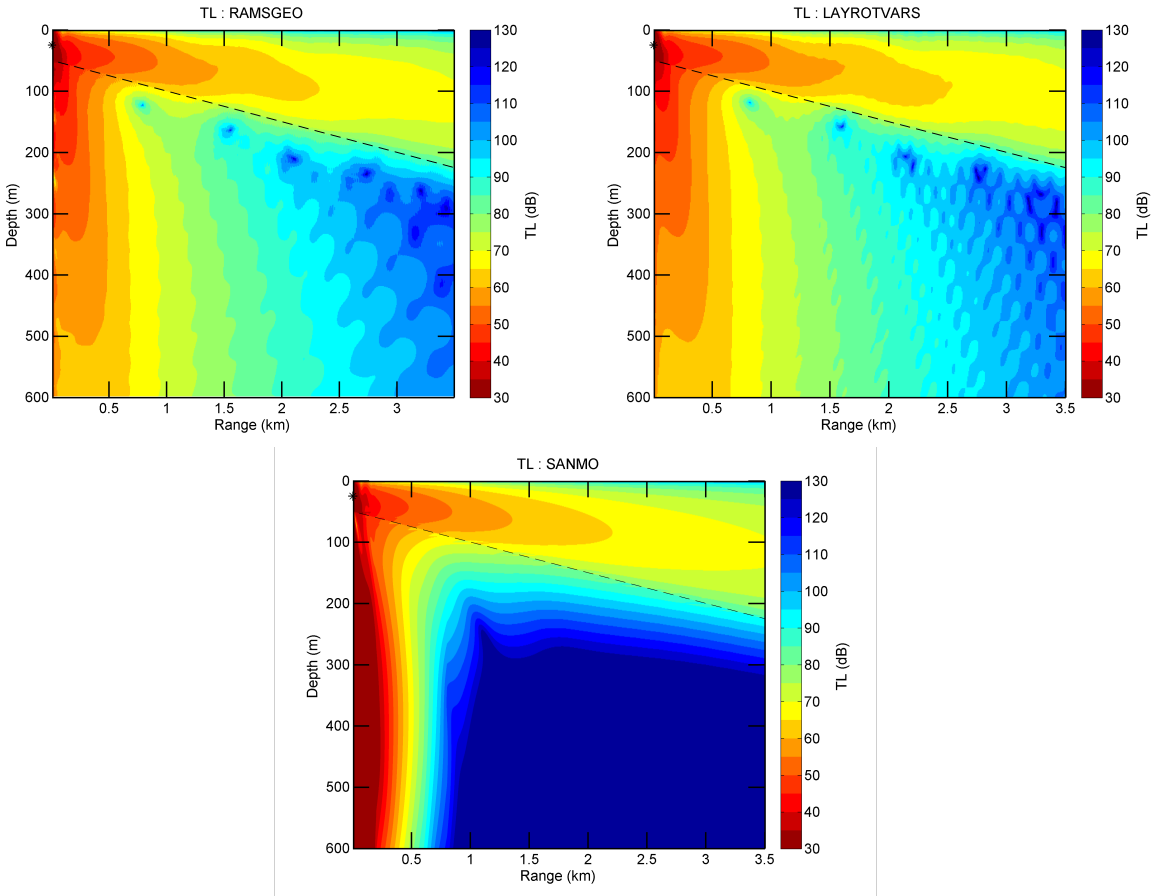


Figure 4.14: Cross-sections of TL for the DOWN case with an attenuating Airy halfspace.

The agreement in water column transmission loss between SANMO, RAMSGEO, and LAYROTVARS is also good for the DOWN case. The use of an attenuating Airy halfspace does produce differences between the water column field and the field in the elastic bottom but when compared to the PEs the differences are on the order of 2 dB. As in the UP case, even though the attenuating gradient does result in differences compared to the PEs it forces the transition of a given mode past the branch line to be smooth. This provides a smooth transition of a leaky mode to a propagating mode and results in a smoothly varying field in both the elastic bottom and the water column as the bathymetry varies with range.

4.4 Discussion: Different Elastic Bottom Representations

For upslope propagation the amplitude of the mode functions (specifically the amplitude of the mode function that is in the water column) that transition into the

bottom is very different for the false bottom and Airy halfspace seabeds. To illustrate this, Figure 4.15 shows the real part of modes 2 and 3 at a range of 1 kilometre from the source. The mode functions for a standard elastic halfspace are also shown. Mode 2 is a trapped mode at this range and there is very little difference between the mode functions. However, mode 3 at this range has just transitioned into the bottom and there is a noticeable difference between the mode functions for the different bottom representations.

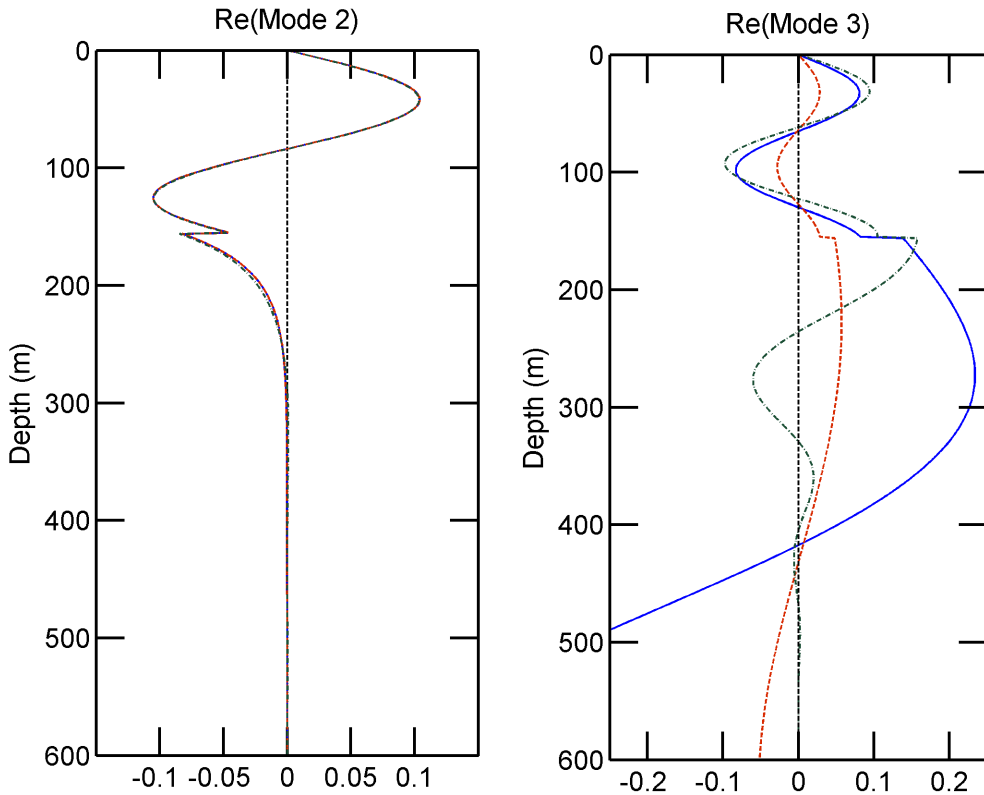


Figure 4.15: The real part of the mode function for a halfspace bottom (blue), false bottom (red), and attenuating Airy halfspace (green). (Left Panel) The real part of mode 2. (Right Panel) The real part of mode 3.

The inclusion of a false bottom increases the number of modes present around the branch cut (Westwood et al., 1996), thus the energy of a single leaky mode is redistributed between several false bottom modes. If elastic mode coupling were considered for the false bottom case, it is possible that this would redistribute the energy between false bottom modes and give a more accurate seismoacoustic field prediction. While it is not yet feasible to consider mode coupling for elastic modes

this point can be illustrated by considering the fluid bottom equivalent. Figure 4.16 shows upslope propagation for a fluid wedge where sound speed, density, and attenuation are the same as the elastic wedge considered above. Figure 4.16 shows three plots comparing adiabatic modes with a halfspace bottom representation, adiabatic modes with a false bottom representation, and a coupled mode result with a false bottom representation. The fluid coupled mode algorithm presented here uses the modes from ORCA and is described in Appendix B. When mode coupling is considered, a false bottom treatment of the seabed produces a much more accurate transmission loss result for the fluid wedge. So a similar result may be achieved for the elastic wedge if mode coupling between elastic modes of a false bottom were considered.

Following an analogues procedure but for downslope propagation, Figure 4.17 compares the results for a halfspace and false bottom representations of the seabed with adiabatic modes and a false bottom representation with the coupled mode model. For the downslope propagation scenario the resultant transmission loss predictions in the water column are all very similar but the fields in the bottom are not comparable. The inclusion of mode coupling does not appear to have as significant of an effect on the water column sound field as it did for upslope propagation scenario shown in Figure 4.16. Extending this to the elastic wedge, the inclusion of elastic mode coupling would not have as significant of an improvement of seismoacoustic field predictions for downslope propagation compared to using an adiabatic approach.

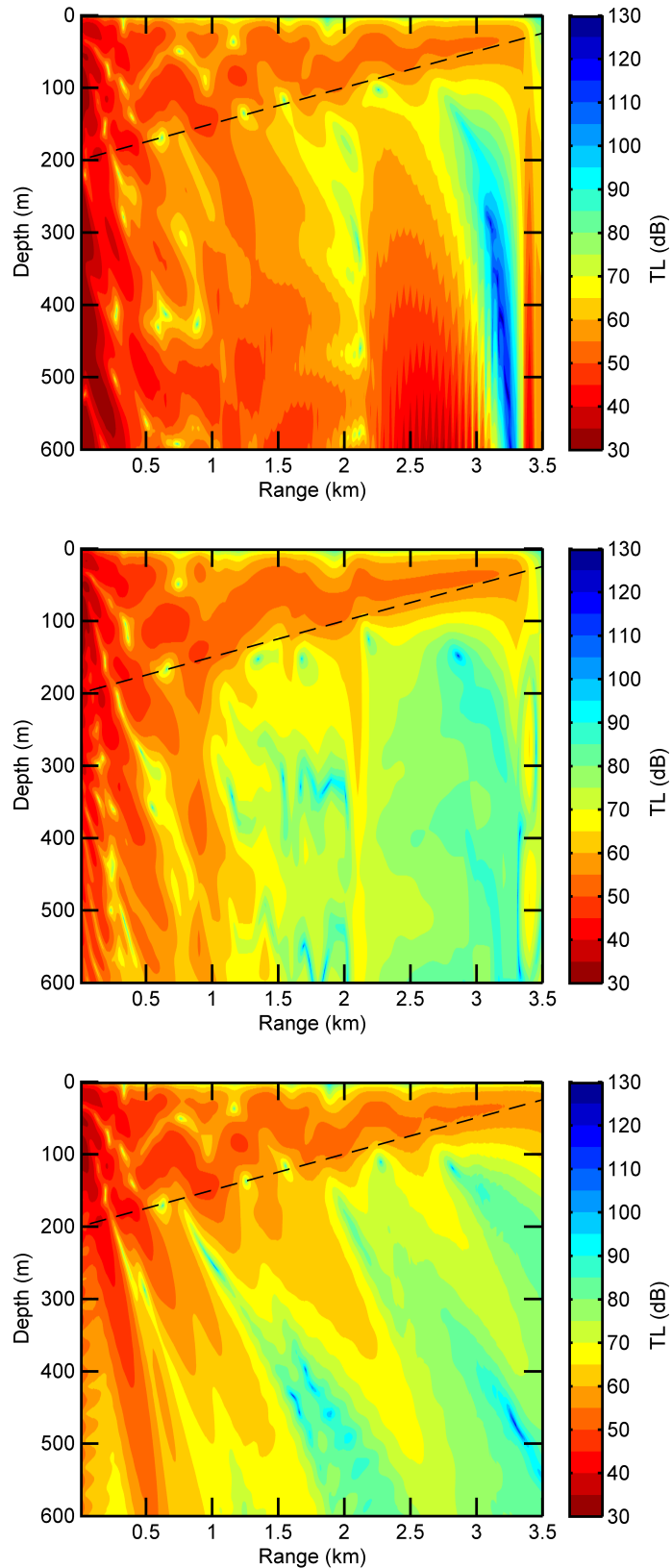


Figure 4.16: Transmission loss cross-sections for upslope propagation with a fluid seabed. *Top Panel:* Adiabatic modes with a fluid halfspace bottom. *Middle Panel:* Adiabatic modes with a false bottom. *Bottom Panel:* Coupled modes with a false bottom.

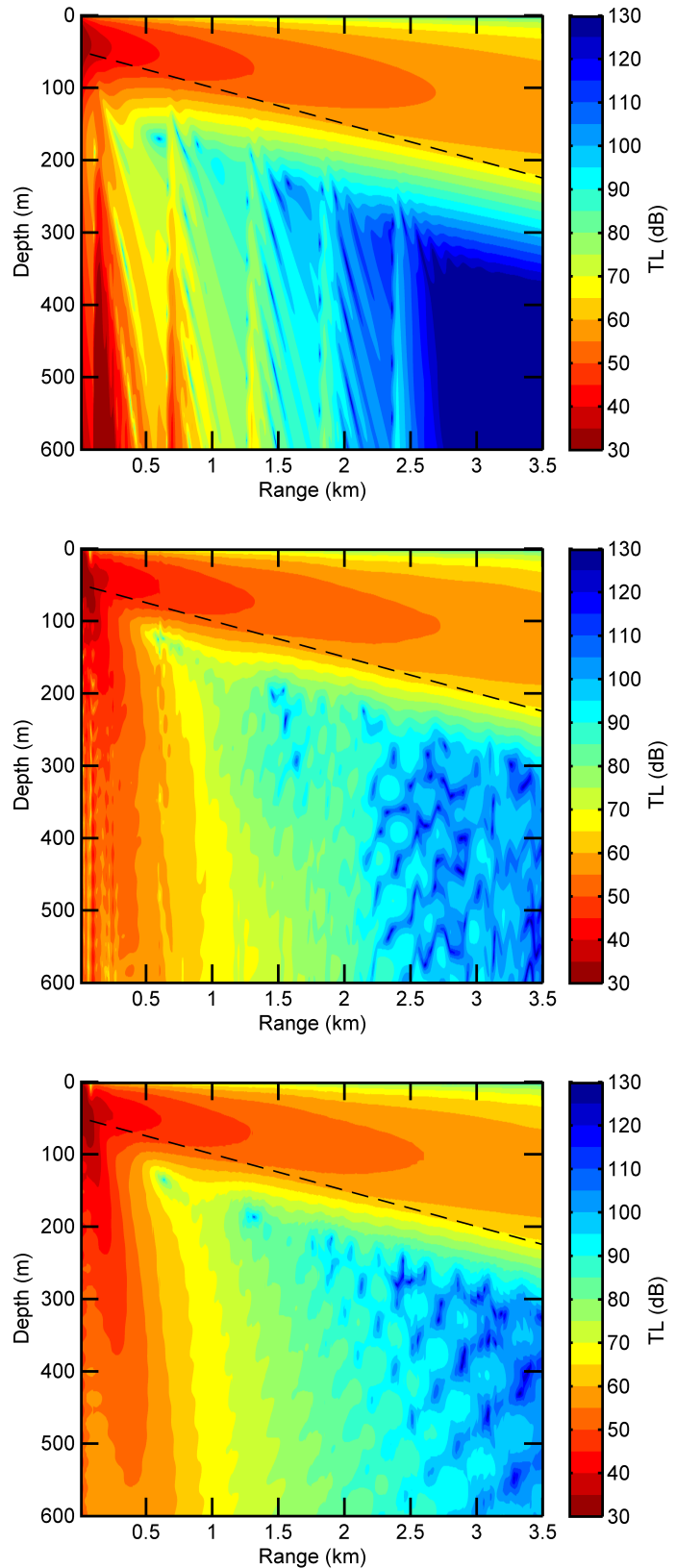


Figure 4.17: Transmission loss cross-sections for downslope propagation with a fluid seabed. **Top Panel:** Adiabatic modes with a fluid halfspace bottom. **Middle Panel:** Adiabatic modes with a false bottom. **Bottom Panel:** Coupled modes with a false bottom.

A few points are clear from the above analysis that considers different treatments of the elastic bottom for modelling sound transmission in the ASA elastic wedge.

- For the UP case, the use of a false bottom with SANMO does not result in a more consistent transmission loss compared to the PE predictions as it did in the FLAT case. When compared to the fluid case, if range dependent mode coupling with elastic modes were used with a false bottom a more accurate solution may be achieved for upslope propagation.
- When used with SANMO, the attenuating Airy halfspace produces results that are in good agreement with the PE models for transmission loss in the water column for the UP case. The standard halfspace representation will also produce a good result for the field in the water column as shown here and by Tindle and Zhang (1997).
- For the UP case, the transmission loss in the elastic bottom is not consistent with the PE predictions. However, the attenuating Airy halfspace representation compared to the standard halfspace representation yields a smoother transition of trapped modes to leaky modes. In the DOWN case, the Airy halfspace yields a smooth transition from leaky modes to trapped modes.
- The field in the DOWN case propagates almost purely adiabatically. Moreover, nearly total adiabatic propagation is consistent with the range dependent fluid bottom scenario where downslope propagation is almost completely adiabatic for slopes less than 6° (Tindle et al., 1987; Yudichak et al., 2006).

4.5 Summary

Section 4.2 outlines a simple mathematical approach to implement an adiabatic normal mode method for seismoacoustic propagation. The core of the method stems from a coupled mode method initially developed for seismic interface wave propagation. The normal mode program ORCA is used to compute the eigenvalues and eigenfunctions and the seismoacoustic adiabatic extension of this, SANMO, interpolates and integrates the modes using an adiabatic approximation. The range

dependent, pressure, displacement potential, stresses, particle displacements, and particle velocities can then be calculated using this approach.

SANMO was tested in Section 4.3 with the ASA elastic wedge benchmark scenario for flat, upslope, and downslope propagation. Two seismoacoustic PE models and a WNI model were used to assess the accuracy of SANMO’s solution for range independent propagation and only the PE models were used to assess the accuracy of SANMO’s solution range dependent propagation. A false bottom and an attenuating Airy halfspace were used in an attempt to better represent the field in within the lower halfspace for various propagation scenarios.

For the FLAT case, the use of a false bottom resulted in a much better agreement in SANMO’s transmission loss with the output of OASES, RAMSGEO, and LAYROTVARS. This was not found to be the same result for the UP case. While the false bottom allows for more modes to represent the halfspace field, the lack of mode coupling ignored in the adiabatic method does not redistribute the correct amount of energy between these modes and therefore produces erroneous transmission loss results. A fluid only wedge was used to confirm this hypothesis.

When used with SANMO, an attenuating Airy halfspace resulted in the smoothest transition from propagating to leaky modes for the range dependent scenarios. The DOWN case was less sensitive to the lack of mode coupling between neighbouring modes as they transition from leaky modes to propagating modes, and this is consistent with the downslope propagation in the purely fluid case.

CHAPTER 5 Numerical Modelling of Bass Strait Data

This Chapter examines range dependent propagation of low frequency signals over seabeds with a complex layered elastic structure, where the seabed structure consists of thick and thin layers of calcarenite. These types of sea bottoms are considered to be indicative of the seabed structure found in Bass Strait Australia and are similar to the type of layered structures that were discussed in Chapter 3. Both SANMO and LAYROTVARS, which were compared and tested in Chapter 4, are used to model transmission loss for five range dependent scenarios. The range dependent scenarios were chosen to make the comparison of numerical predictions with measured data at the end of this chapter.

The following analysis is split into two parts. The first section considers the numerical results from SANMO and LAYROTVARS for the range dependent environments. The aim is to compare numerical results from both models. The second part considers the transmission loss predictions from SANMO and LAYROTVARS which are used to calculate estimates of Sound Exposure Level (SEL) from an airgun array. The predicted SELs are then compared to the SELs computed from data measured on an autonomous seafloor hydrophone recorder. This chapter aims to show the applicability of the adiabatic method to real world scenarios and compares it with the single-scatter rotated coordinate seismoacoustic PE method.

5.1 Modelling of Broadband Low Frequency Propagation over a Range Dependent Layered Elastic Seabed

The airgun signals recorded in Bass Strait have been generally characterised as broad band signals with a significant amount of energy centred around approximately 20 Hz (Duncan et al., 2013). For the numerical analysis of sound propagation in Bass Strait, transmission loss was calculated in 1 Hz increments over a band of low frequencies from 2 Hz to 100 Hz. As discussed in Chapter 3, propagation over calcarenite a seabed results in the majority of energy in the acoustic field propagating in very narrow bands near the cutoff frequencies. Therefore, a 1 Hz frequency increment was chosen to capture changes in transmission loss at these frequencies

and adjacent frequencies as the bathymetry varies. The propagation modelling of the range dependent scenarios were further divided into two sections based on the degree of range dependence. The bathymetry for this work was obtained from a digital elevation map produced by Geoscience Australia (GA) (Whiteway, 2009).

The first two range dependent scenarios were taken from Duncan et al. (2013). In their paper the authors examined and modelled low frequency signals produced by a seismic survey (Survey 1), which were measured on an array of autonomous underwater sound recorders. The range dependent propagation paths were chosen based on the largest source and receiver separation. These two scenarios are discussed in section 5.1.1 and the bathymetric profiles are labelled as Bathymetry 1 and Bathymetry 2 respectively.

The last three scenarios correspond to data that was gathered from an earlier seismic survey (2004) in Bass Strait (Survey 2). The bathymetric variations from source to receiver were again chosen from the largest source-receiver separations. However, these propagation paths span sections of the seabed with more variable bathymetry and therefore exhibit a higher degree of range dependence. These scenarios are discussed in section 5.1.2, and corresponding profiles are labelled as Bathymetry 3, 4, and 5.

Figure 5.1 shows a map of the different survey locations. Based on the relative locations of the surveys, the same geoacoustic seabed parameters from Duncan et al. (2013) were used in the modelling for all the scenarios. The same parameters were used because of a lack of detailed information about the geoacoustic parameters of the seabed in the Bass Strait area.

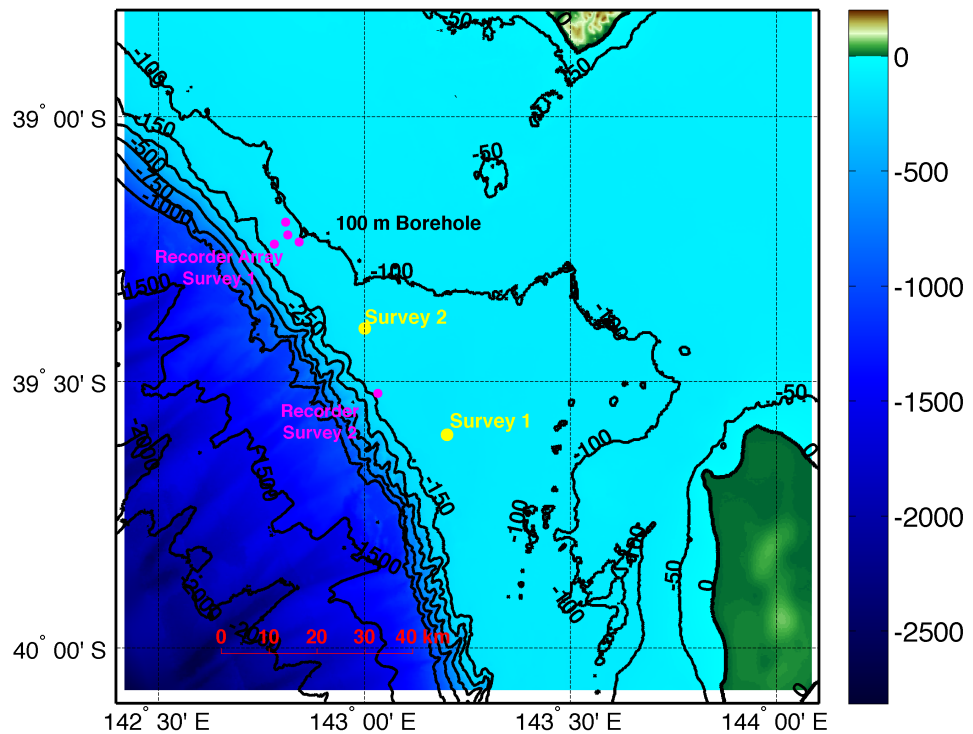
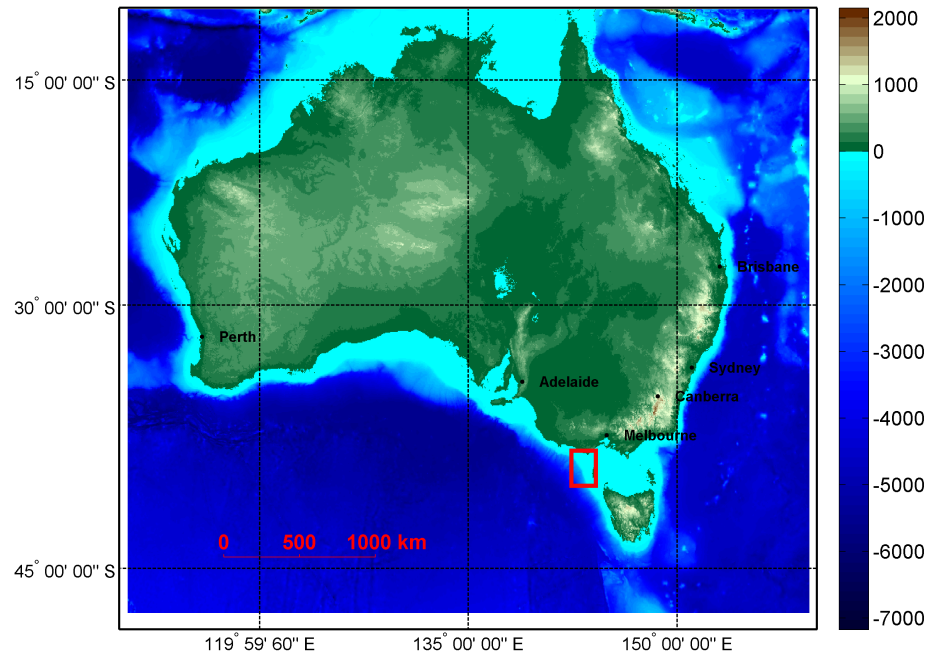


Figure 5.1: Top Panel: A topography and bathymetry of Australia in which the study region in western Bass Strait is indicated by the red square (Whiteway, 2009). **Bottom Panel:** The approximate locations of the 100 m geotechnical borehole and locations of autonomous underwater sound recorders in relation to the two seismic surveys discussed in this chapter; Survey 1 corresponds to the results of (Duncan et al., 2013) and Survey 2 corresponds to an earlier survey.

The geoacoustic parameters were used for the seabed for sections 5.1.1 and 5.1.2 are presented in Table 5.1 and Figure 5.2 shows the water column sound speed profile taken from Duncan et al. (2013). The authors in Duncan et al. (2013) note that the geoacoustic parameters were estimated from geotechnical data obtained from a 100 m borehole (see Figure 3.2 in Chapter 3 and Figure 5.1) and head wave refraction analysis was used to determine the deeper structure. The sound speed profile was obtained from CTD casts for Survey 1. Moreover, in keeping with the analysis of the aforementioned authors, the layered calcarenite structure was assumed to follow the bathymetry.

Table 5.1: Geoacoustic Properties for the Layered Calcarenite Bottom proposed by Duncan et al. (2013)

Layer Type	Thickness (m)	ρ (g/cm ³)	c_p (m/s)	c_s (m/s)	α_p (dB/λ)	α_s (dB/λ)
Calcareous Cap-rock Layer	1	2.3	2600	1200	0.2	0.4
Slightly semi-cemented Calcarenous	100	1.9	2100	550	0.12	0.25
Semi-cemented Calcarenous	900	1.9	2200	650	0.12	0.25
Sedimentary Basement	N/A	3.0	3800	1900	0.1	0.2

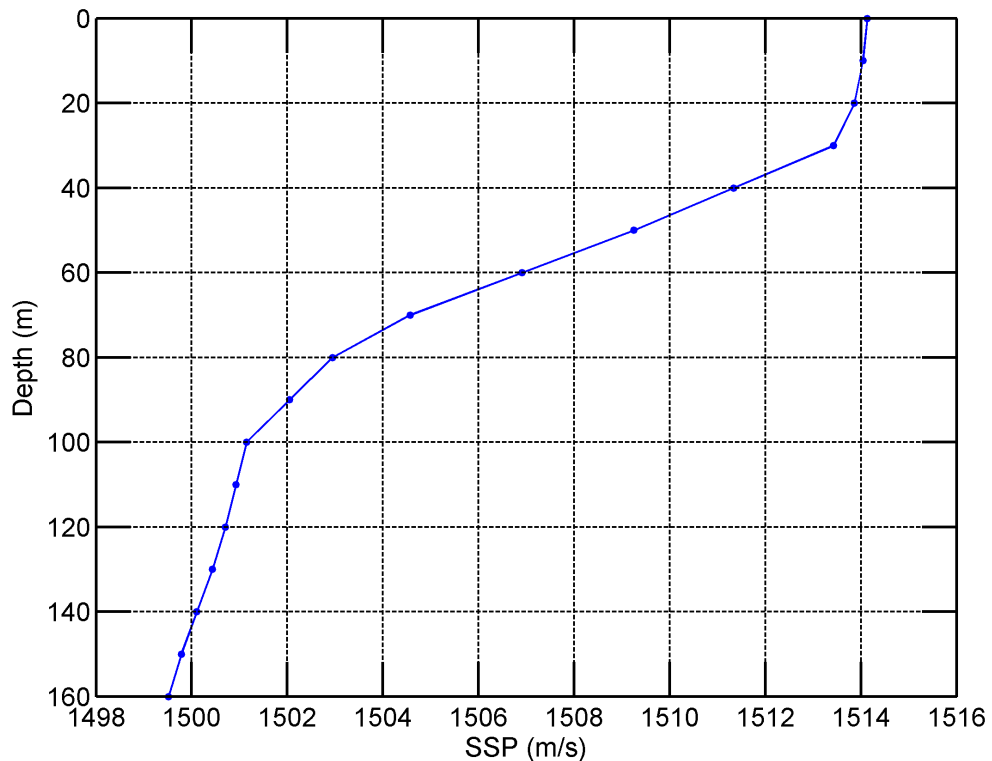


Figure 5.2: Water column sounds speed profile for modelling Bass Strait range dependent scenarios from Duncan et al. (2013).

5.1.1 Range Dependent Broadband Low Frequency Propagation over Layered Elastic Seabeds with Gradually Varying Bathymetry

Table 5.2 and Figure 5.3 summarise the variations in bathymetry from source to receiver. To facilitate a comparison with measured data later in the chapter the source and receiver were interchanged. Using the reciprocity principle interchanging the source and receiver locations means that multiple source locations from a moving survey vessel needn't be modelled. Since the sound recorder was bottom-mounted, the source location for the propagation modelling was placed 1 metre above the seafloor. The new interchanged source depths for the two modelling scenarios are 104 metres and 113 metres respectively for Bathymetry 1 and Bathymetry 2. The new receiver depth of 7 metres was used for Bathymetry 1 and Bathymetry 2, which is the original tow depth of the airgun array. The bathymetry in Figure 5.3 was taken from the propagation paths when the source and receiver locations were interchanged.

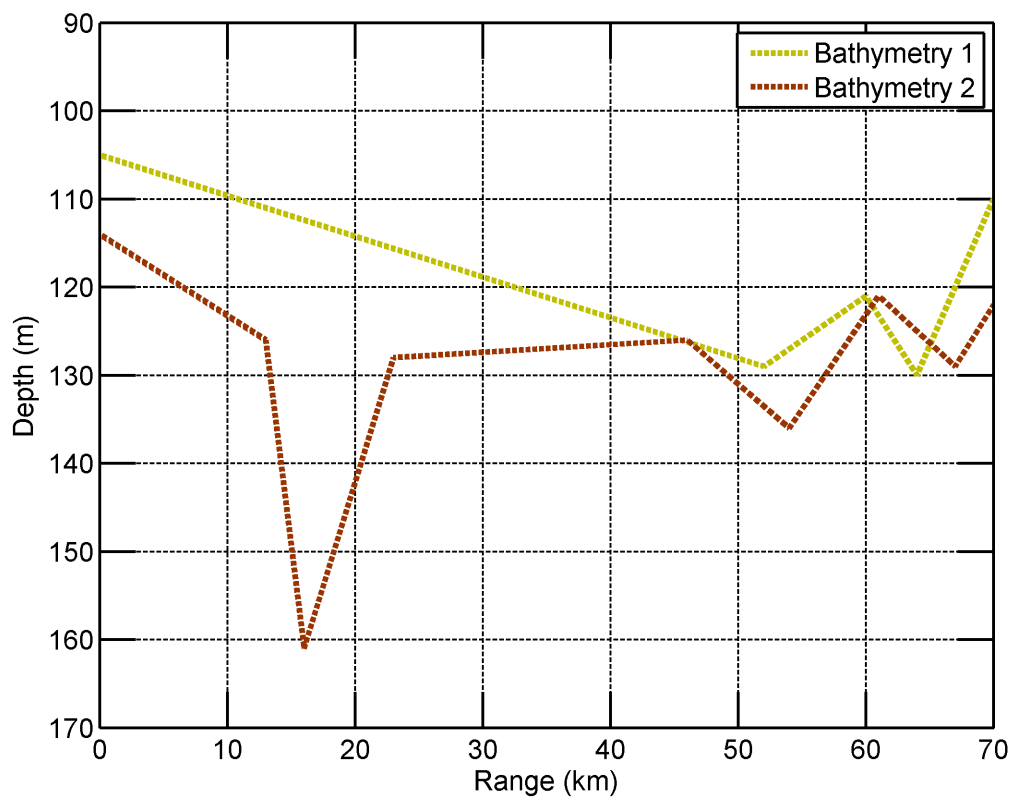


Figure 5.3: Bathymetry profiles from Geoscience Australia (Whiteway, 2009) for Bathymetry 1 and Bathymetry 2.

Presented below in Figure 5.4 are the transmission loss predictions from SANMO and LAYROTVARS for Bathymetry 1. The figure shows the transmission loss versus frequency at a receiver range (RRX) of 40 kilometres and a receiver depth (ZRX) of 7 metres. The agreement between the two curves is good.

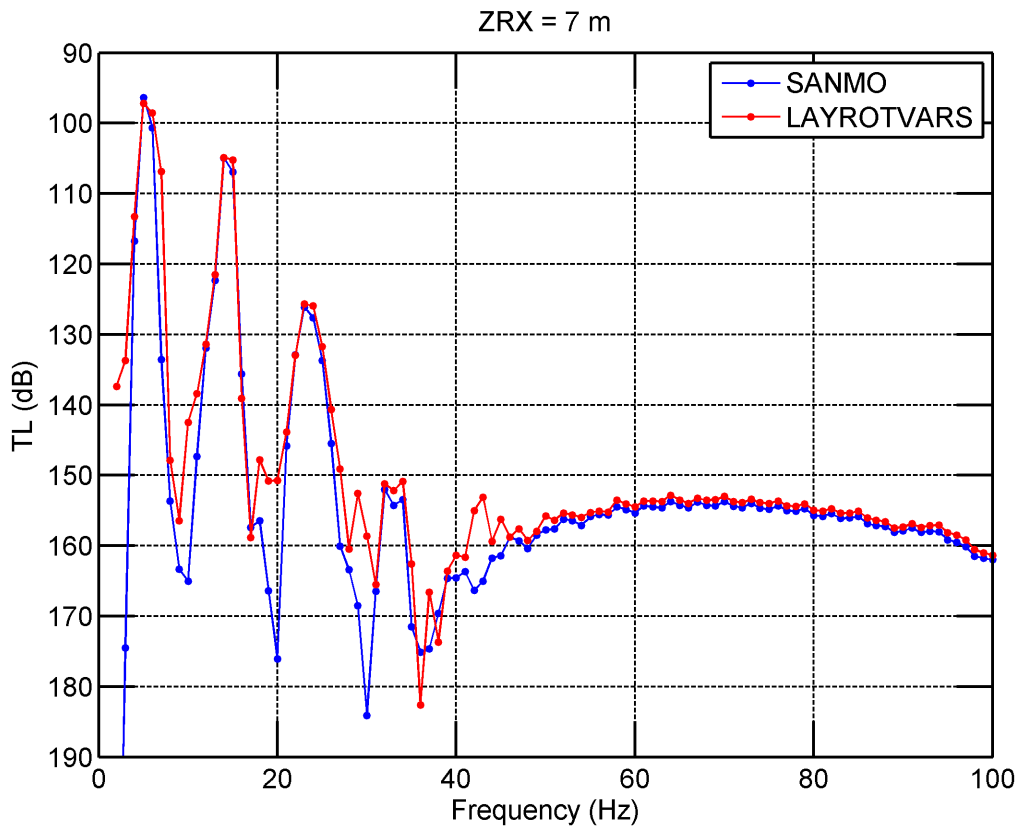


Figure 5.4: Comparison of the transmission loss versus frequency predicted by SANMO and LAYROTVARS at a depth of 7 m and range of 40 km for Bathymetry 1.

Transmission loss variations shown in two-dimensional plots can only be compared as a function of one spatial variable and frequency at most. The two panels in Figure 5.5 compare the transmission loss as a function of frequency and range at a receiver depth of 7 metres for LAYROTVARS and SANMO. Both the models produce a very similar transmission loss prediction and show the narrow bands of low transmission loss typical of propagation in shallow water environments with highly elastic seabeds as previously discussed in Chapter 3.

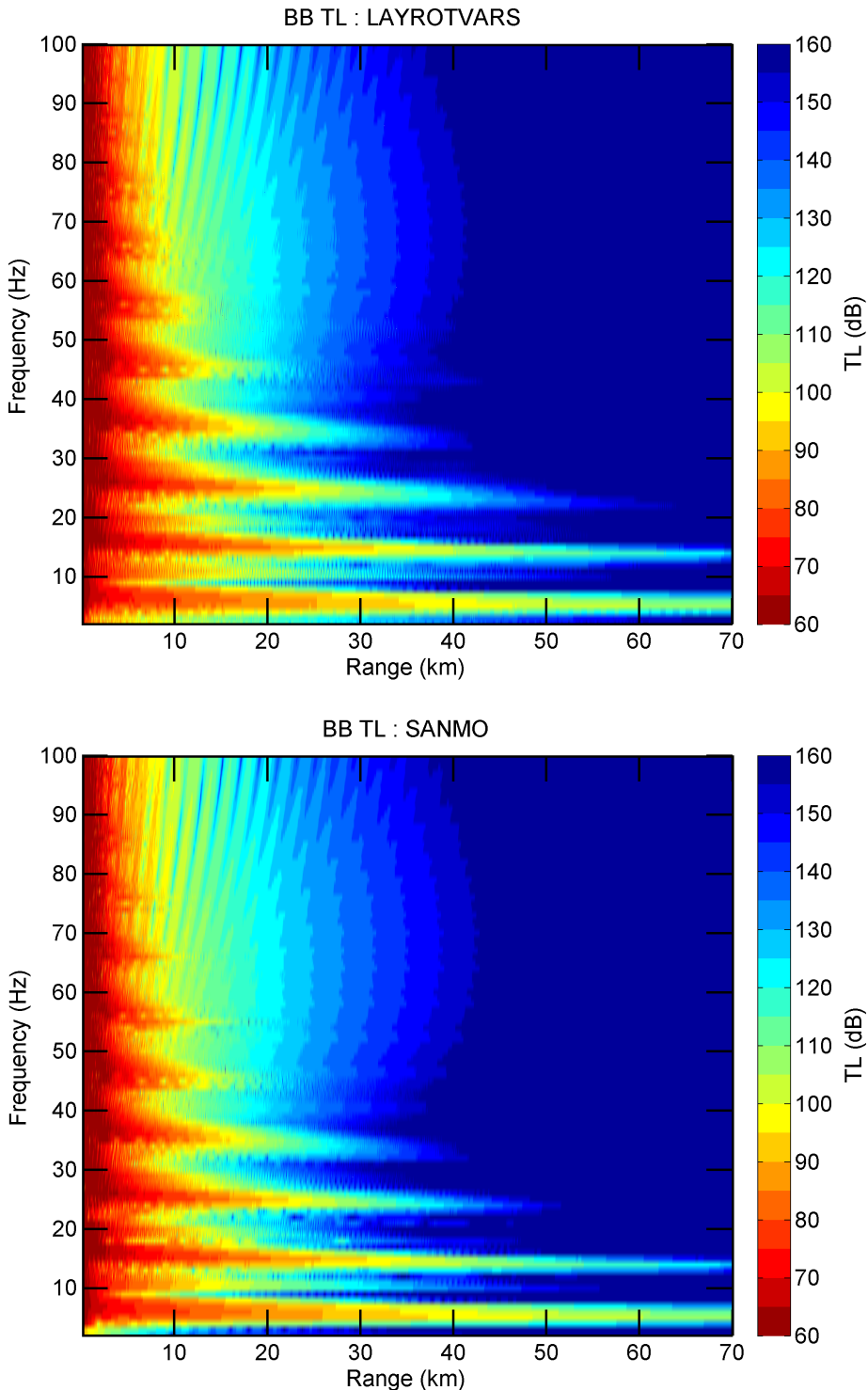


Figure 5.5: A comparison plot from SANMO (bottom panel) and LAYROTVARS (top panel) showing a broadband transmission loss cross-section at a source depth of 7 m and a source-to-receiver range of 40 km for Bathymetry 1.

As further discussed in Chapter 3, the shallow water environment with a layered calcarenite seabed modelled here has a band pass filter effect on the water column sound field (Duncan & Gavrilov, 2012; Gavrilov et al., 2012; Duncan et al., 2013).

As a mode propagates, the amount of modal attenuation is a function of both bathymetry and frequency. This can be seen in Figure 5.6 that shows the variation of the modal attenuation coefficient for the first 5 modes for Bathymetry 1 at a frequency of 23 Hz. The modal attenuation coefficient is proportional to the imaginary part of each wavenumber. The water depth at the source range is 105 metres and at 23 Hz mode 3 is close to its critical wavenumber and therefore it has a relatively low modal attenuation coefficient. As the water depth increases, there is an optimal depth where mode 3 propagates with the least amount of attenuation. The total modal attenuation coefficient at any range is given by the integrated variation along the acoustic path. The effect of the bathymetry can shift the modal attenuation coefficient to higher or lower values, which can affect the water column sound field when the sound field is dominated by one propagating mode, as in the case discussed here.

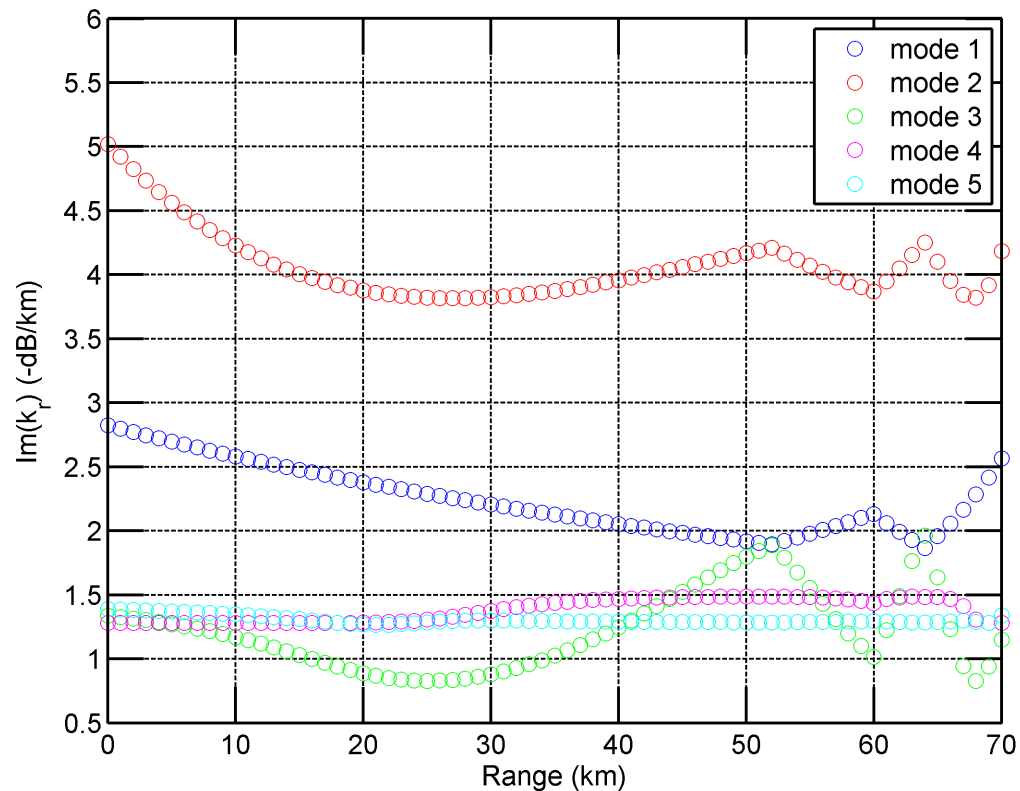


Figure 5.6: Modal attenuation coefficient for Bathymetry 1, Mode 1 – 5 at a frequency of 23 Hz.

The low frequency transmission loss for Bathymetry 2 at a receiver range of 40 kilometres and a receiver depth of 7 metres is shown in Figure 5.7. Bathymetry 2 has stronger variations in water depth than Bathymetry 1, but the adiabatic mode results are still in good agreement with the LAYROTVARS' results.

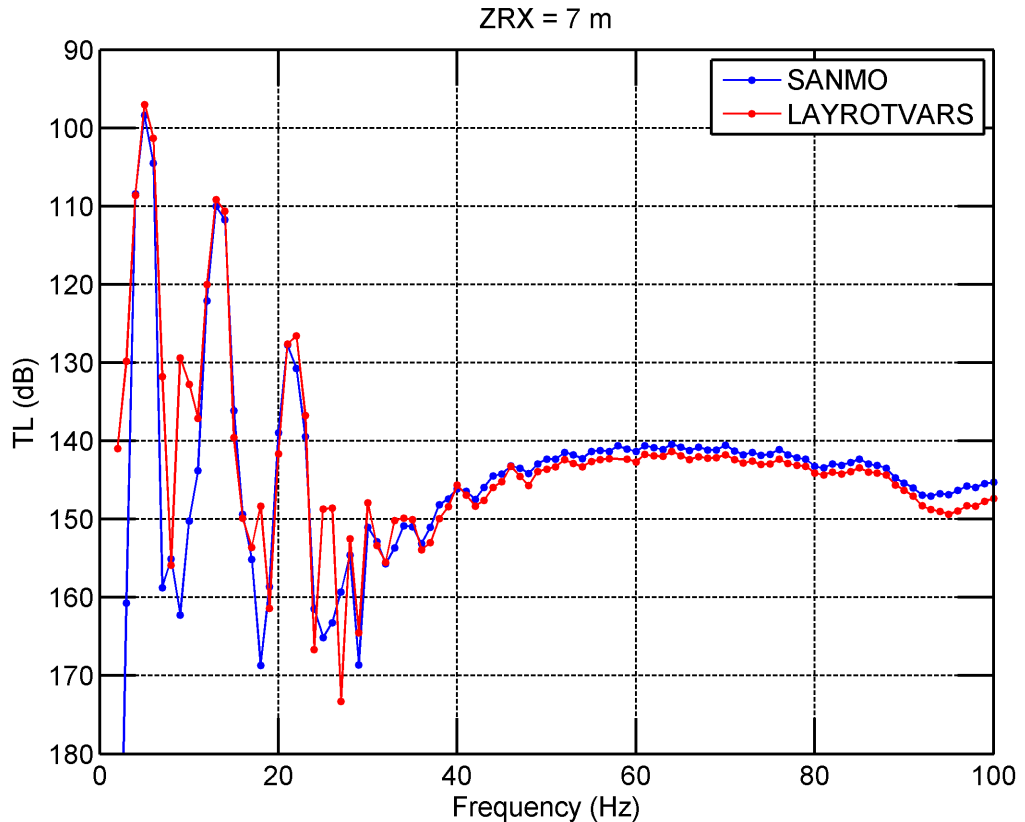


Figure 5.7: Comparison of the transmission loss versus frequency predicted by SANMO and LAYROTVARS at a depth of 7 m and range of 40 km for Bathymetry 2.

An interesting observation is the presence of secondary low loss peaks (or side lobes) around the mode 3 peak for Bathymetry 1 shown in Figure 5.4. The same can be observed around the mode 2 and mode 3 peaks for Bathymetry 2 in Figure 5.7. These side lobes are not replicated in the adiabatic mode prediction. Therefore, the presence of these side lobes may be due to mode coupling between adjacent modes as individual wavenumbers transition past the branch cut. This is discussed further in section 5.1.4.

To compare the transmission loss at additional receiver depths within the waveguide, Figure 5.8 shows variation of the transmission loss as a function of range at

frequencies of 21 Hz and 75 Hz for a receiver at a depth of 7 metres and 30 metres for Bathymetry 2. Two depth slices at receiver ranges of 20 kilometres and 59 kilometres are also shown in the bottom left panel at a frequency of 21 Hz.

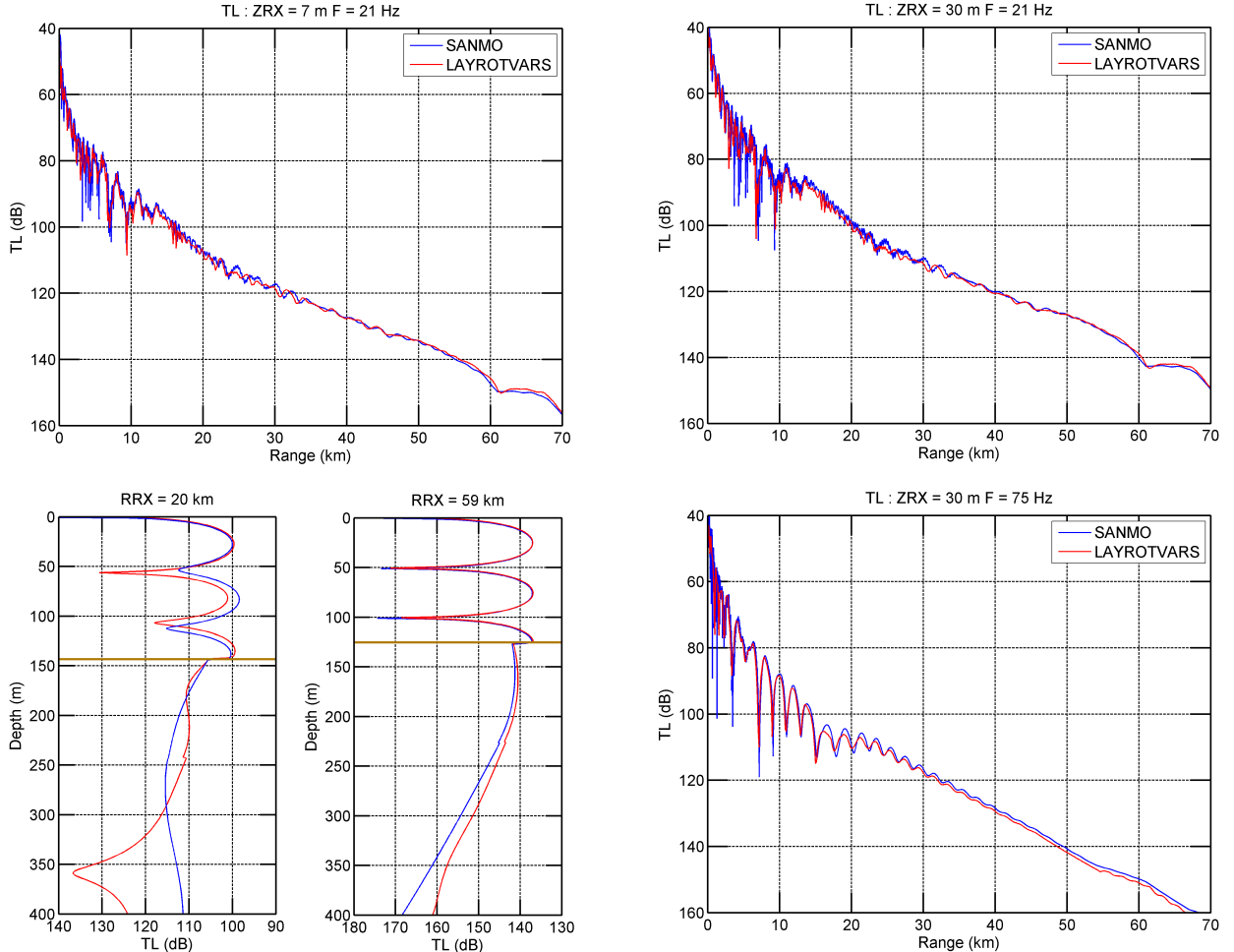


Figure 5.8: Single frequency transmission loss slices for Bathymetry 2, showing transmission loss range slices at a depth of 7 metres and 30 metres (top left and top right) at a frequency of 21 Hz, Depth slices at ranges of 20 and 59 kilometres (bottom left), and an additional range slice at a depth of 30 metres at a frequency of 75 Hz. The brown lines in the bottom left panels represent the seafloor interface.

The agreement is still good; however, there are differences of one to three dB at some ranges and depths when comparing transmission loss in the water column. It is likely that this is a due to a limitation associated with the adiabatic approximation.

5.1.2 Range Dependent Broadband Low Frequency Propagation over Layered Elastic Seabeds with Rapidly Varying Bathymetry

Figure 5.9 shows the bathymetric variations for Survey 2. All the interchanged source depths for bathymetries 3 – 5 are at 131 metres, because there was only one recorder, and the interchanged receiver depth was 6 metres, the tow depth of the second array. The total change in sea depth over the propagation path is about 20 metres, which is less than that for Bathymetry 1 and Bathymetry 2 in the previous section. However, bathymetries 3 to 5 are rougher with rapid changes in the water depth over relatively shorter distances. Again the bathymetry data were taken from GA's digital elevations model.

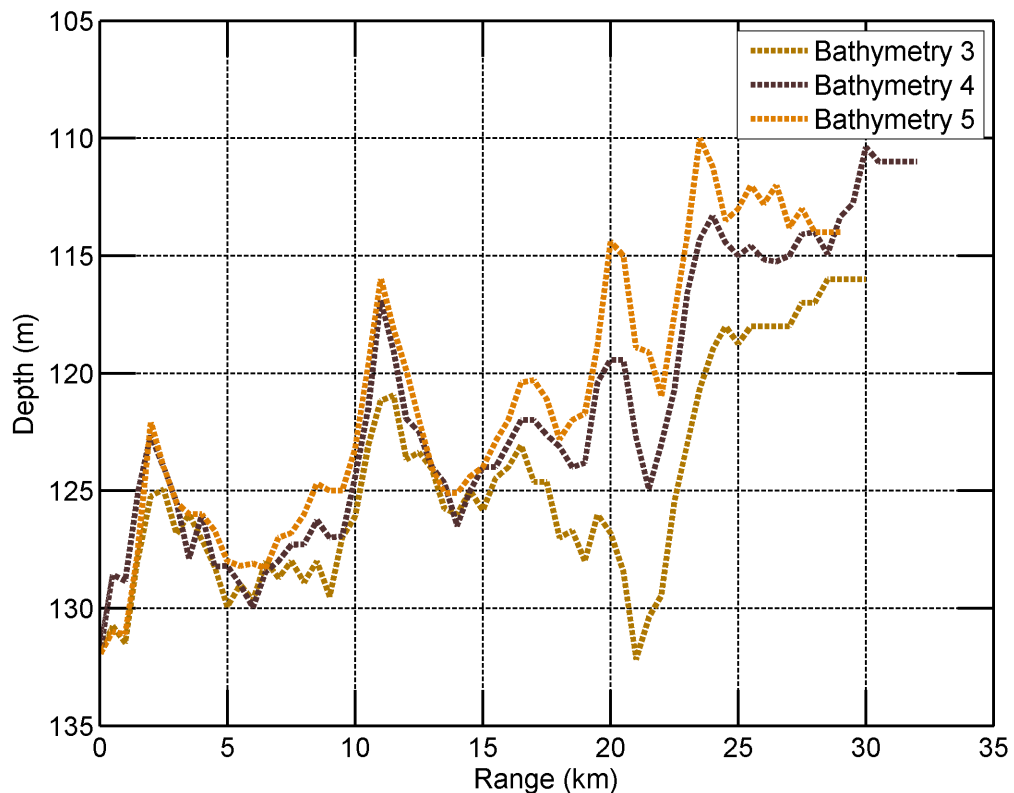


Figure 5.9: Bathymetry profiles from Geoscience Australia (Whiteway, 2009) for Bathymetries 3 to 5.

Figure 5.10 shows broadband transmission loss slices for bathymetries 3 to 5 at receiver depths of 6 metres and 75 metres, both of which are within the water column. All the curves are plotted at a range of 20 kilometres.

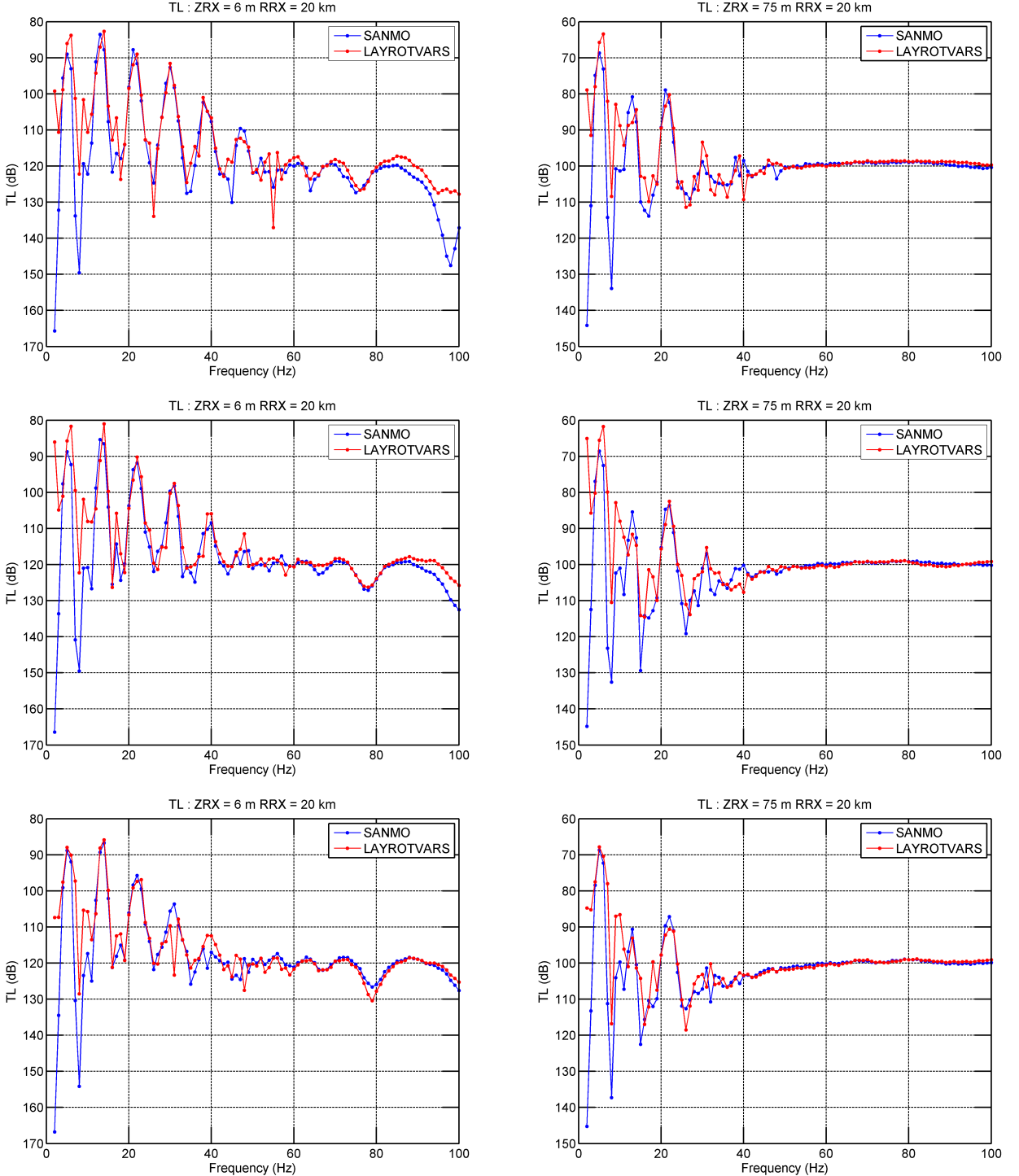


Figure 5.10: Left Panels: Broadband transmission loss slices for Bathymetries 3 – 5 (top – bottom) at a receiver depth of 6 m. **Right Panels:** Broadband transmission loss slices for Bathymetries 3 – 5 (top – bottom) at a receiver depth of 75 m. The transmission loss are plotted at a receiver range of 20 km for all the plots.

To examine the transmission loss at additional receiver depths within the waveguide, Figure 5.11 shows cross sections of transmission loss as a function of range and depth at the frequencies of 21 Hz and 75 Hz for Bathymetry 5. At 21 Hz, the

acoustic field is dominated by mode 3 because it propagates with minimal attenuation. When comparing the results from SANMO and LAYROTVARS, the influence of the variable bathymetry can be seen. From the LAYROTVARS result at 21 Hz, the rapid bathymetric variations changes the transmission loss in correlation with peaks in the bathymetry. This effect is not fully reproduced by the adiabatic method and is likely due to mode coupling over the rough bathymetry. At 75 Hz both LAYROTVARS and SANMO produce very similar transmission loss results at long ranges. About eleven trapped modes make up the majority of the sound field in the water column at 75 Hz. Since 75 Hz is not near a cutoff frequency the seabed mainly acts as a loss mechanism through attenuation and shear wave conversion in the sub-bottom. After 4 kilometres only mode one and two dominate the water column sound field and gradually the contribution of mode two decreases leaving mostly mode 1 after 20 kilometres.

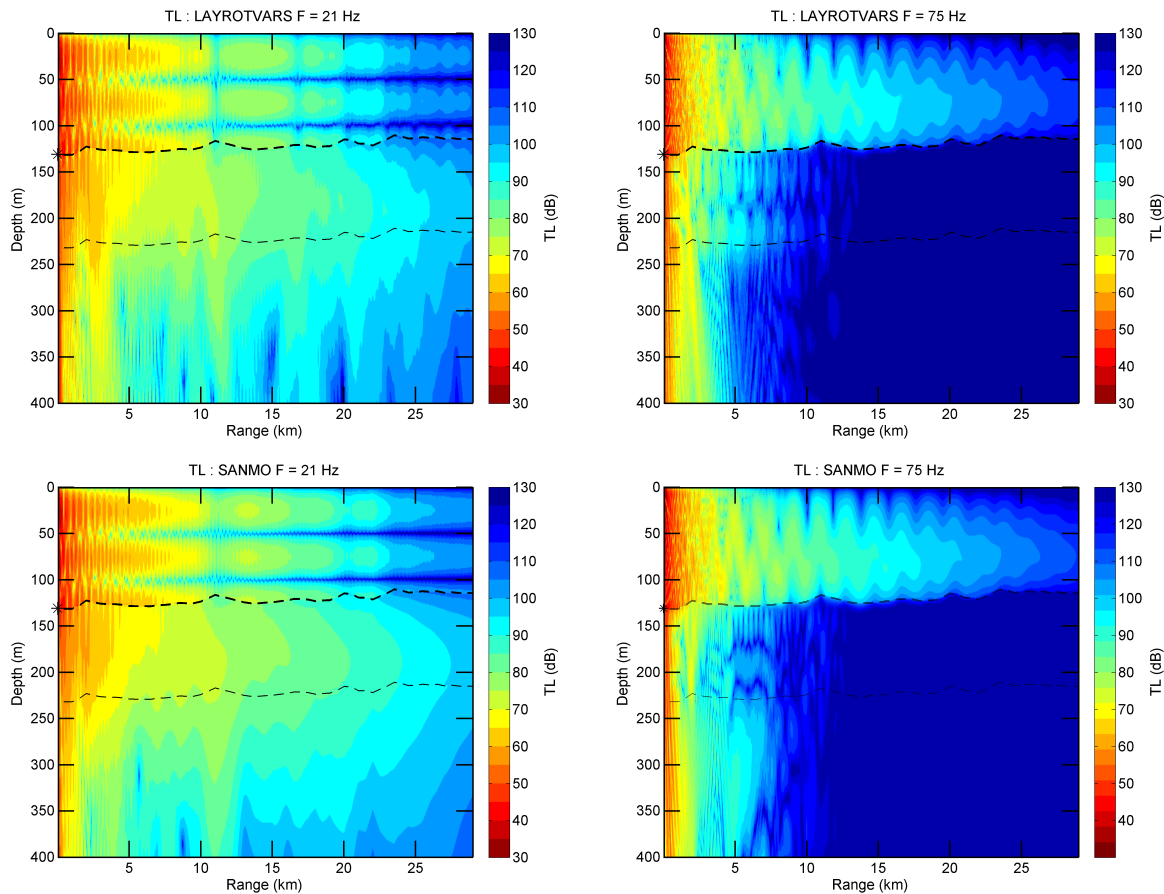


Figure 5.11: Single frequency transmission loss slices for Bathymetry 5. Left Panels: LAYROTVARS (top) and SANMO (bottom) at a frequency of 21 Hz. Right Panels: LAYROTVARS (top) and SANMO (bottom) at a frequency of 75 Hz.

Several transmission loss plots for the propagation scenario of Bathymetry 5 are shown in Figure 5.11 in an analogous form to Figure 5.8. These line plots further highlight the scattering effects due to variable bathymetry of the elastic seabed on the acoustic field for individual modes that propagate with low attenuation near their cutoff frequencies. At higher frequencies this effect is not as dominant at long ranges, which is likely due seabed attenuation and shear wave conversion having a larger influence at higher frequencies, as discussed cap-rock case in Chapter 3.

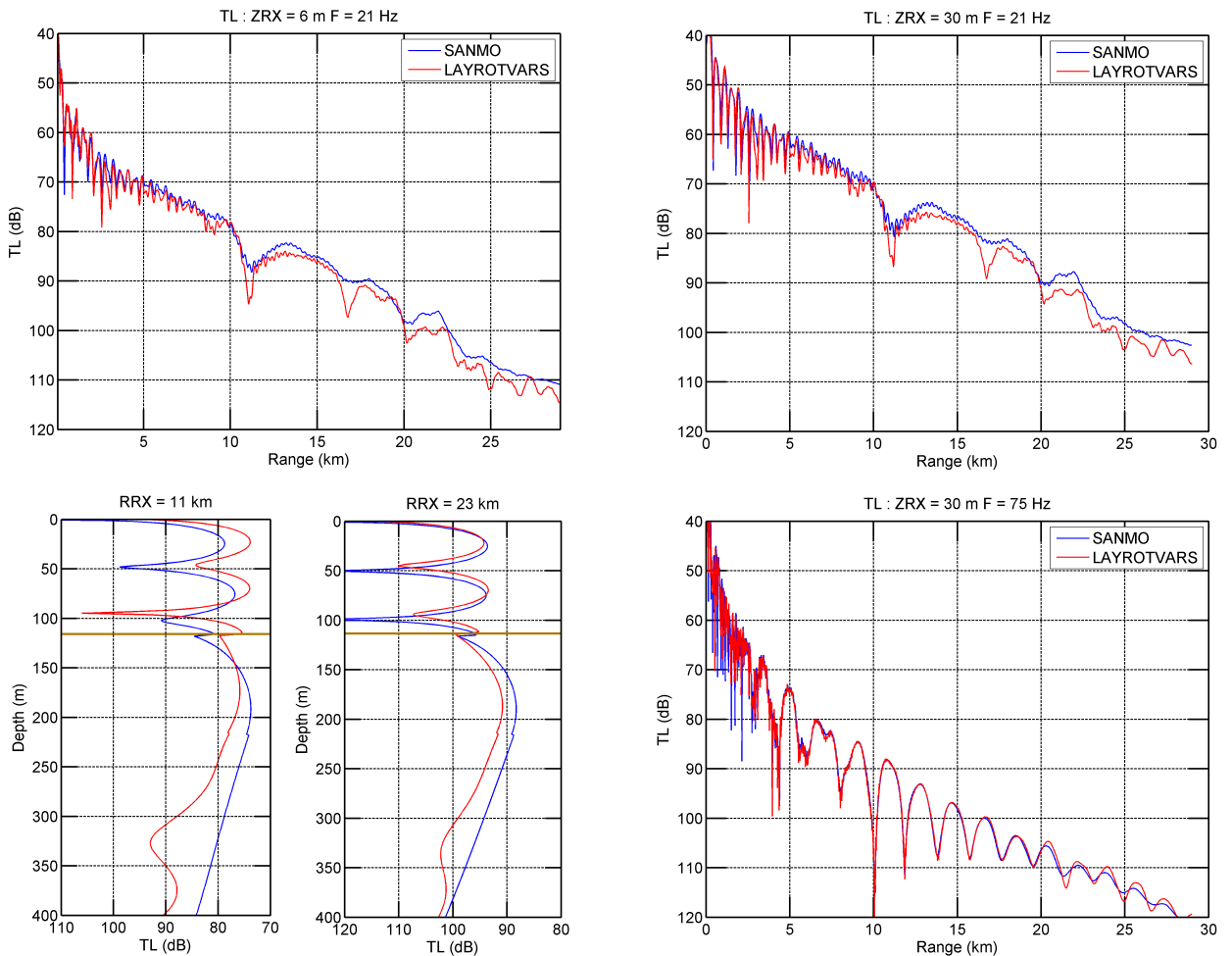


Figure 5.12: Single frequency transmission loss slices for Bathymetry 5 showing transmission loss range slices at a depth of 6 m and 30 m (top left and top right) at a frequency of 21 Hz. Depth slices at ranges of 11 km and 23 km (bottom left), and an additional range slice at a depth of 30 m at a frequency of 75 Hz. The brown lines in the bottom left panels represent the seafloor.

Together, Figures 5.9 – 5.12 illustrate the following points:

- For the range dependent seafloor profiles (Bathymetry 3 - 5) there is good agreement in the transmission loss predictions between SANMO and LAYROTVARS.
- Around the cutoff frequencies (e.g. 21 Hz which is close mode 3's cutoff frequency), the extrema's of the bathymetry produce a noticeable difference between the LAYROTVARS and SANMO's transmission loss predictions. This can be interpreted as a consequence of mode coupling, which scatters energy into higher and lower order modes, an interaction that is not included in SANMO.
- At the higher end of the frequency range considered here (e.g. 75 Hz) the influence of scattering over rough bathymetry appears to be less apparent at the longer ranges, and the adiabatic mode solution is in good agreement with the results from LAYROTVARS.

The differences between the two models are discussed further in the next subsection.

5.1.3 Influence of Mode Coupling on the Water Column Acoustic Field

In this section a brief examination of the influence of mode coupling in some of the above range dependent scenarios is discussed. Some of the deviations between the LAYROTVARS and adiabatic mode method may be attributed to ignoring mode coupling in the adiabatic solution. The following analysis uses an approximate acoustic single-scatter mode coupling algorithm described in Appendix B. The algorithm generally follows the coupling algorithm proposed by (Porter et al., 1991) and the mode functions and wavenumbers from ORCA were used in the analysis. An example of some similar work has been done by Tindle et al. (2000), but here it is applied to a seismoacoustic problem.

Before examining and interpreting the results of the mode coupling algorithm and LAYROTVARS the model, a few points need to be discussed:

- The mode functions calculated by ORCA satisfy the fluid and elastic boundary conditions at horizontal interfaces
- The coupling algorithm discussed in Appendix B and applied here is based on the conservation of energy flux through a vertical plane for fluid

environments but the coupling integrals here are evaluated over depths that included the elastic layers.

- The equations defining energy flux conservation for fluid (Morse & Ingard, 1968) and elastic materials (Auld, 1973; Ben-Menahem & Singh, 1981) are different, so using fluid coupling coefficients for acoustic-elastic mode functions is incorrect.

Therefore, the aim to see if the addition of mode fluid coupling can explain some of the difference between SANMO and LAYROTVARS, albeit even if fluid coupling coefficients do not completely satisfy energy flux conditions. The use of fluid coupling coefficients should be sufficiently accurate because the modes are initially excited in the water column, and so the majority of the modal energy should stay in the water column.

Two examples are considered to investigate the influence of mode coupling. Example 1 considers the environment for Bathymetry 5 and propagation at a frequency of 21 Hz shown in Figure 5.11 and Figure 5.12. The geoacoustic model that is used is the same as that presented in Table 5.1. The focus of this example is on explaining the dips in the transmission loss that occur in correlation with the apexes in the bathymetry. Example 2 considers Bathymetry 1 at a frequency of 29 Hz; this frequency corresponds to one for the side lobes in the broadband transmission loss slice predicted by LAYROTVARS and shown in Figure 5.4.

5.1.3.1 Example 1: Bathymetry 5 at 21 Hz

Figure 5.13 and Figure 5.14 show the results of applying the coupled modes model to the scenario defined by Bathymetry 5, the geoacoustic model is the same as that presented in Table 5.1. Here the coupled mode result is referred to as CM+ORCA to represent the combination of the mode functions from ORCA with the coupled mode algorithm in Appendix B. Figure 5.14 shows line plots at receiver depths of 6 metres and 30 metres similar to those presented in Figure 5.12. It is clear from these transmission loss colour cross-sections in Figure 5.14 compared to Figure 5.11 and curves in Figure 5.14 compared to Figure 5.12, that mode coupling does influence the propagation at this frequency. The inclusion of mode coupling produces a better

match to LAYROTVARS' transmission loss predictions over the sections of rapid changes in the bathymetry. Moreover, the fields in the bottom bare better resemblances as well.

However, there are also points where the agreement between the coupled modes and PE transmission loss predictions is poor. In particular, after 23 kilometres the coupled mode solution begins to exhibit an oscillatory behaviour, which the PE solution does not. A fully seismoacoustic coupled mode propagation model that correctly conserves acoustic and elastic energy flux would be better suited to determine the cause this type of behaviour. A propagation model of this type has not yet been developed.

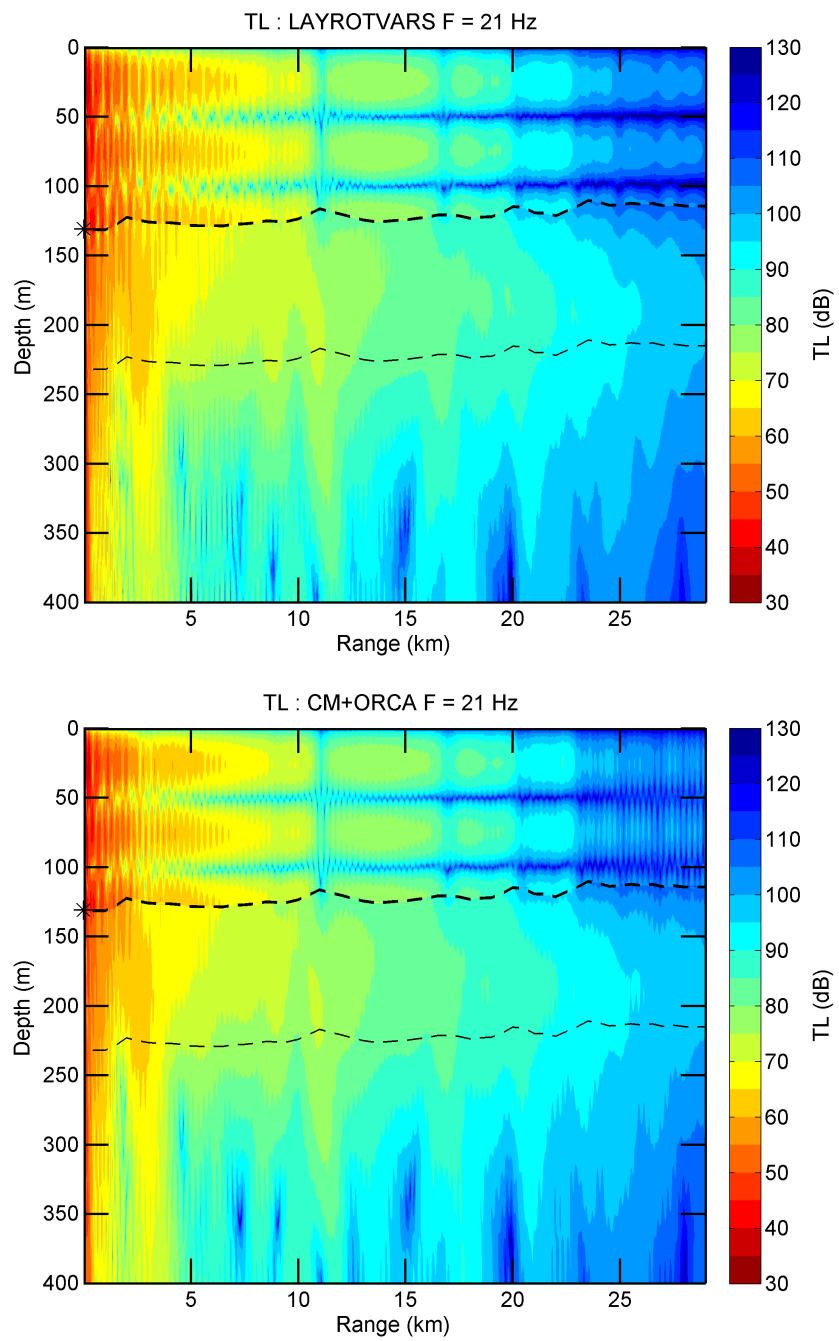


Figure 5.13: *Top Panel:* Transmission loss cross-section at 21 Hz for Bathymetry 5 from LAYROTVARS. *Bottom Panel:* same from acoustic coupled modes and ORCA.

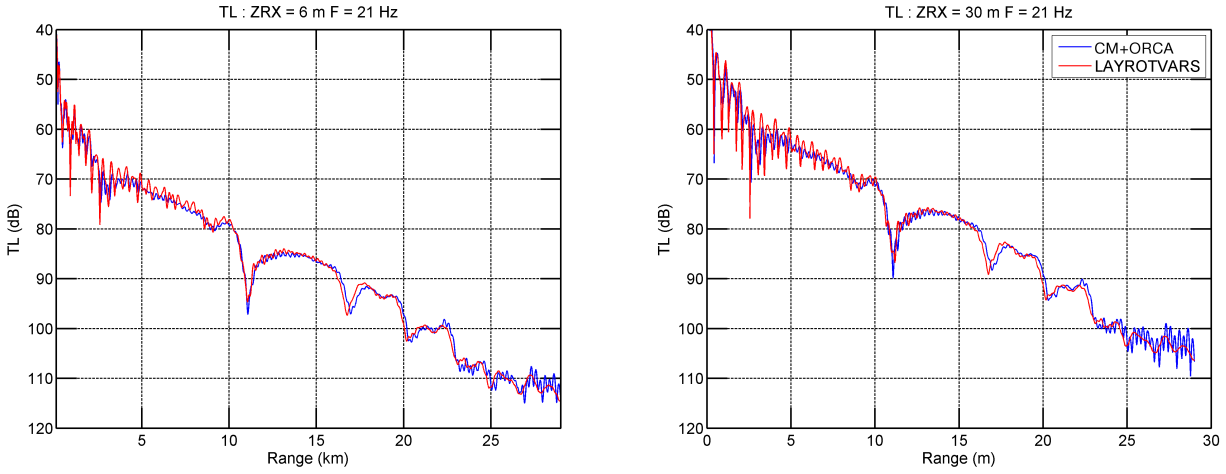


Figure 5.14: *Left Panel:* Transmission loss plot at 21 Hz for Bathymetry 5 from LAYROTVARS and acoustic coupled modes with ORCA at a receiver depth of 6 m.
Right Panel: same at a receiver depth of 30 m.

5.1.3.2 Example 2: Bass Strait Bathymetry 1 at 29 Hz

The panels in Figure 5.15 show the results of applying the coupled modes model to the scenario defined by Bathymetry 1 at a frequency of 29 Hz. Note that the range scale starts at 10 kilometres and ends at 40 kilometres. Both the adiabatic mode solution and the coupled mode solution predict very similar transmission loss. LAYROTVARS' solution, however, exhibits a different transmission loss prediction in the water column at ranges greater than 30 kilometres and peculiar "bands" of lower transmission loss in the bottom.

It is not clear whether these features predicted by LAYROTVARS are correct physical predictions or they represent numerical errors in the single-scatter rotated coordinate PE solution. The bands may also be a numerical artefact due to truncation of the PE's computational grid at the stress release surface at the end of the false bottom. If reflections off the stress release surface were present in the solution from LAYROTVARS, they would likely be observed when the reflections off the other layers were relatively small. The frequencies in-between the cutoff frequencies are one such case. For this bathymetry profile and this frequency, the differences between SANMO and LAYROTVARS are not explained by lack of mode coupling in the adiabatic approach used by SANMO. So the side lobes around

the main cutoff frequency peaks in Figure 5.4, 5.7, and 5.10 are not a consequence of fluid mode coupling. However, they may still be explained by elastic mode coupling, which has not been considered here. For practical purposes, the difference between the models at this frequency is negligible given the large loss at such long ranges from the source.

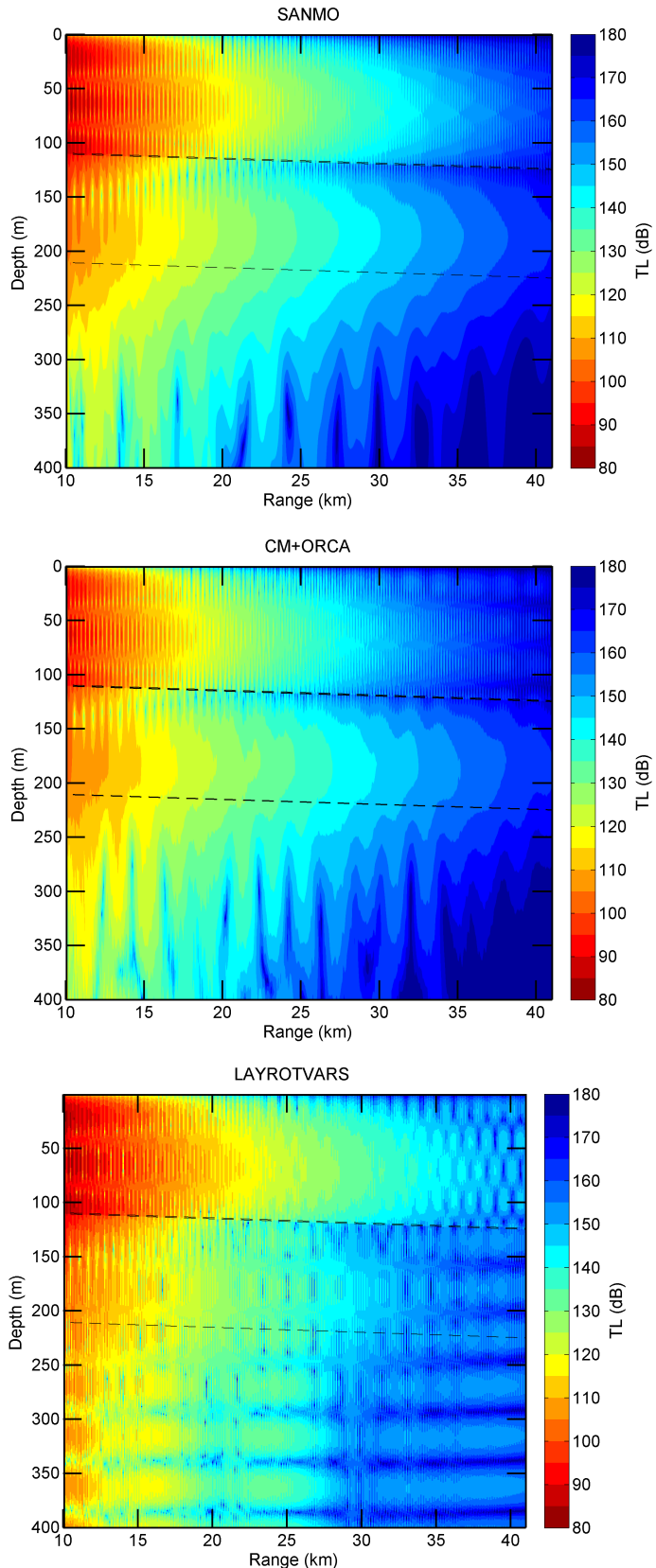


Figure 5.15: Transmission loss cross-sections at 29 Hz for Bathymetry 1 from SANMO (Top Panel), Acoustic Coupled Modes with ORCA (Middle Panel), and LAYROTVARS (Bottom Panel).

5.1.4 Computational Cost

While the PE reference solution generally produces accurate results (Collis et al., 2007) for range dependent seismoacoustic scenarios. To achieve an accurate solution for acoustic propagation over this type of calcarenite seabed a very fine computational grid was required. The PE model was run with a uniform depth grid spacing of 0.1 metres and a range grid spacing of 2 metres for all the scenarios considered here. The 1 metre thick layer of cap-rock is the reason for the use of such a small computational grid. The grid spacing was determined by running the model with successively smaller grids at a few frequencies until the solutions appeared to converge. Transmission loss from SANMO was calculated at a 1 metre by 1 metre computational grid, but the mode shapes were calculated at a 500 m range increment. The same computational depth grid spacing (i.e. 0.1 m) was not required for SANMO because the amplitude of mode shapes from ORCA are related to reflection coefficients calculated at interface boundaries, so changing the depth grid spacing for ORCA/SANMO does not affect the stability of the normal mode solution.

The small computational grid spacing for LAYROTVARS, especially the depth grid, resulted in long computational runtimes at a single frequency. The total times to perform calculations by LAYROTVARS and SANMO were recorded at each frequency run. The calculations were performed on a desktop computer with an Intel i7-2600 3.4 GHz CPU with 16 GB of RAM. Figure 5.16 shows the total runtimes to perform the broadband transmission loss calculations discussed in this chapter. The maximum total computational time for LAYROTVARS was about 172 hours or 7.2 days and the maximum total computational time for SANMO was about 2.5 hours.

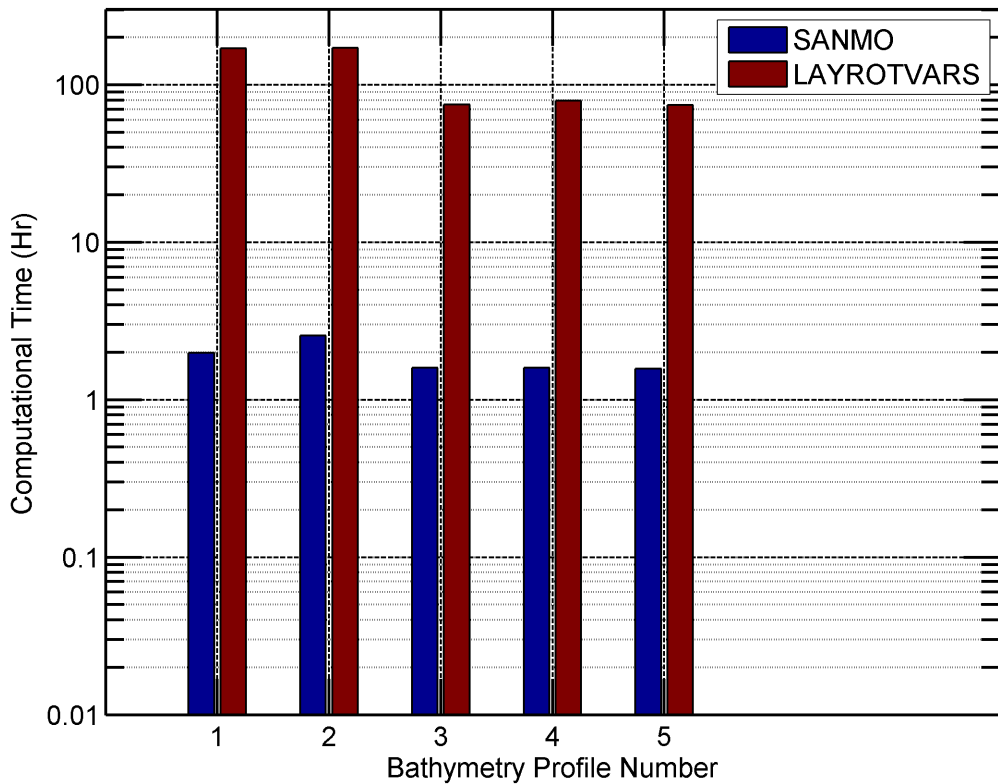


Figure 5.16: Processing time in hours to compute transmission loss for all frequencies for each propagation track.

Figure 5.17 shows the required computational time at each frequency. Generally the time to run SANMO increases with frequency, which is consistent with ORCA finding more modes at higher frequencies and thus taking longer to complete (Westwood et al., 1996). LAYROTVARS on the other hand takes about the same amount of time regardless of frequency and the time to perform the required calculations is just under 2 hours per frequency.

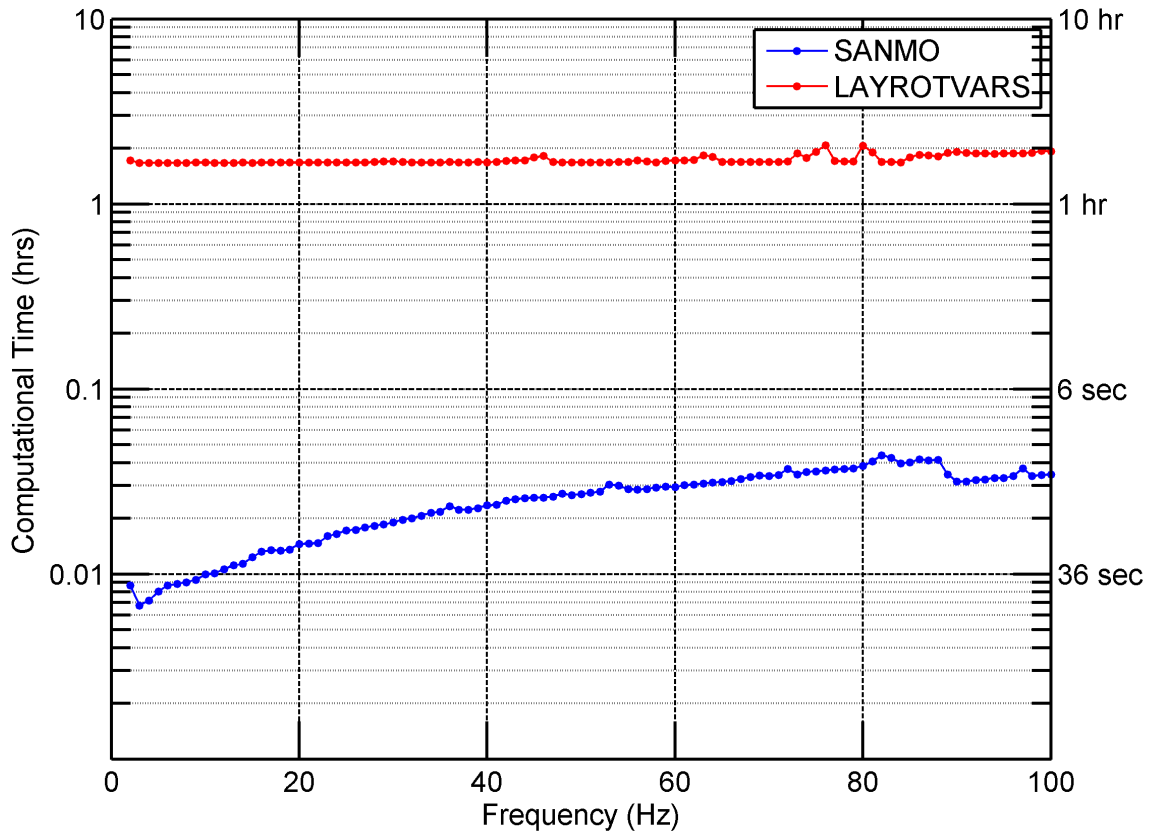


Figure 5.17: Processing time in hours as a function of frequency to compute transmission loss for all frequencies for propagation bathymetry 2.

5.2 Model Predictions and Measured Data Comparison

Section 5.2 presents a case study that applies the transmission loss modelling methods discussed above in a comparison with measured data. The signals from Survey 2 recorded in 2004 were used for this comparison. Figure 5.18 shows the sail tracks for the survey relative to the hydrophone recorder, which was located on the ocean floor.

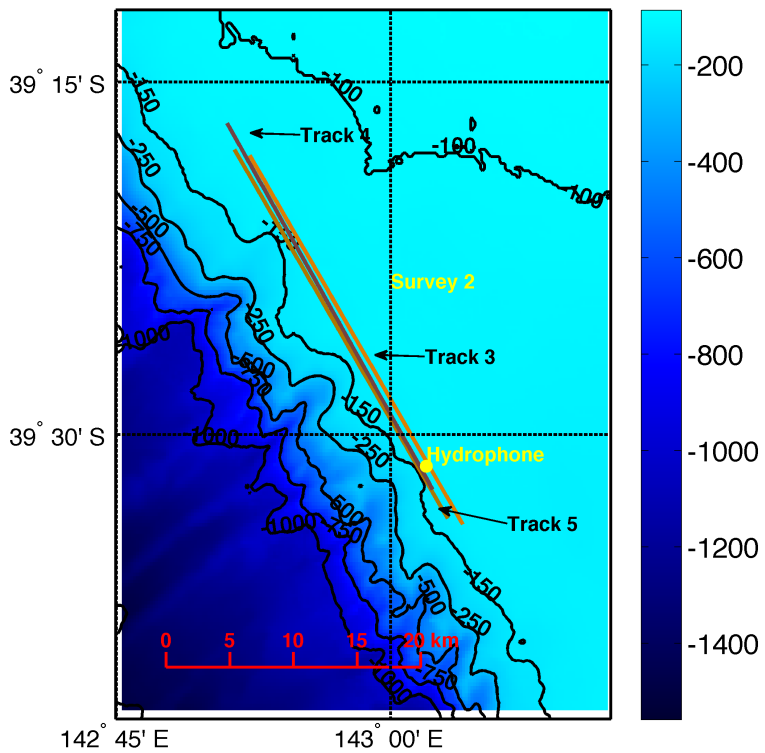


Figure 5.18: A detailed map of survey 2, showing the locations of the hydrophone and the sail tracks from the seismic survey. The track numbering corresponds to the range dependent bathymetry scenarios discussed in section 5.1.

Figure 5.19 shows a colour plot of the Energy Spectral Density (ESD) spectrum computed from airgun array signals measured from track 3. The important features to note in this plot are that the majority of energy is concentrated at low frequencies and that there is a peak pattern that is analogous to that found for calcarenous seabeds (see Figure 5.5 or Figure 3.3 for an example). With these observations in mind, the rest of the chapter is devoted to comparing these data to the modelling prediction that were carried out above in section 5.1. As a reminder, the seabed was assumed to be composed of layered calcarenous.

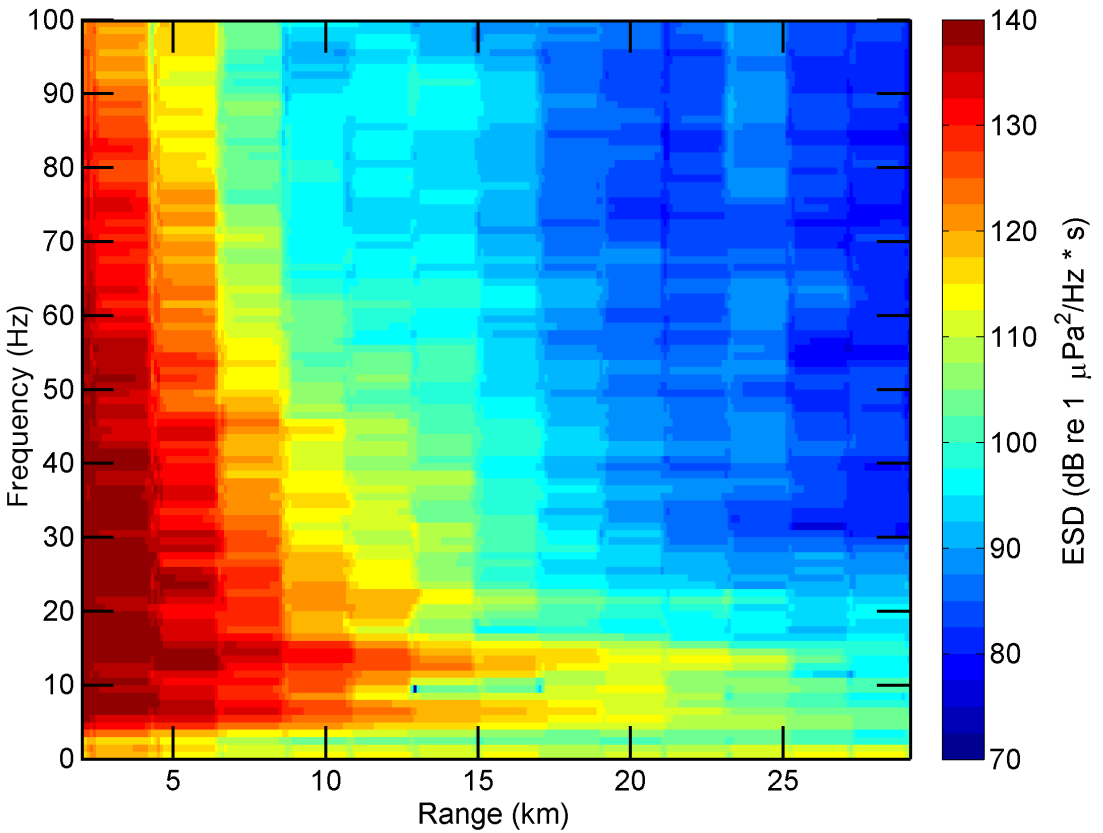


Figure 5.19: Energy Spectral Density calculated from the signals recorded from track 3 (Bathymetry 3) showing the low frequency peaks in acoustic energy associated with propagation over a calcarenite seabed.

5.2.1 Calculation of the Sound Exposure Level

The comparison of data to model results consisted of comparing Sound Exposure Levels (SELs) of the recorded signals with synthetic SELs, which were calculated using the transmission loss results discussed above. In practice the sound exposure level is a commonly used metric for environmental impact assessment (Erbe, 2013) which is why this metric was chosen for this comparison.

Two methods for computing the SEL are discussed below. The first method involves the standard definition of the sound exposure level (Carey, 2006) over a time interval defined by T_1 and T_2 , from which the SEL is given as

$$SEL = 10 \log_{10} \left(\int_{T_1}^{T_2} P(\vec{r}, t)^2 dt \right) dB \text{ re } 1 \mu Pa^2 s, \quad (5.1)$$

where $P(\vec{r}, t)^2$ is the squared acoustic pressure in μPa^2 . A common way to define T1 and T2 is such that a transient signal contains 90% of its energy between these times. This is the method that was used to compute the SEL of the recorded signals.

The second method involves computing the SEL of a signal from its energy density spectrum (Carey, 2006). This method was used to produce synthetic SELs. The energy density spectrum (ESD) of an acoustic signal is proportional to the magnitude of the pressure spectrum from Parseval's theorem (Carey, 2006). The full bandwidth of the source signal is broken into a number of frequency bands, each narrow enough such that a single transmission loss value can be used to represent the transmission loss over the band. The centre of each band is used here. The received sound exposure in a band can be obtained by integration,

$$E_m(\vec{r}) = \left(\int_{\omega_{l,m}}^{\omega_{h,m}} ESD_s(\omega) d\omega \right) \cdot |P_{TL}(\vec{r}, \omega_{0,m})|^2. \quad (5.2)$$

Here $E_m(\vec{r})$ is the sound exposure in the m^{th} frequency band, $ESD_s(\omega)$ is the energy density spectrum of the source signal, $\omega_{l,m}$ and $\omega_{h,m}$ are respectively the lower and upper frequency limits of the m^{th} frequency band, $P_{TL}(\vec{r}, \omega_{0,m})$ is the squared pressure obtained from the transmission loss calculated by a propagation model, and $\omega_{0,m}$ is the angular frequency at the centre of the band. By summing the sound exposures, $E_m(\vec{r})$, over all frequency bands, the SEL at any range or depth can be computed as

$$SEL(\vec{r}) = 10 \log_{10} \left(\sum_m \frac{E_m(\vec{r})}{1 \mu Pa^2 s} \right) dB \text{ re } 1 \mu Pa^2 s. \quad (5.3)$$

The principle advantage of this method is that the SEL at any receiver can be computed entirely in the frequency domain. In contrast, to use Equation (5.1) rather than Equation (5.3) to produce synthetic SELs, Fourier synthesis would be required. Fourier synthesis is an additional step that adds to the computational cost of computing the SEL because it requires the evaluation of the inverse Fourier integral to produce time domain signals at every receiver range and depth, which can then be integrated to obtain the SEL.

To produce synthetic SEL results, an additional numerical model was used to calculate the source spectrum of the airgun array at one metre from its acoustic

centre (Duncan & McCauley, 2000). The source spectra of seismic airgun arrays are generally a function of elevation angle and azimuth angle (Ziolkowski et al., 1982). Figure 5.20 shows the spectrum that was used to calculate the synthetic SELs. The source spectrum was produced using the Centre for Marine Science and Technology's airgun array source model. The spectrum was computed for an elevation 90° and an azimuth 150°. The elevation is relative to a downward vertical line and the azimuth is relative to the sail direction of the survey, so an azimuth of 0° corresponds to a direction parallel to sail track of the survey. An elevation of 90° and an azimuth of 150° were chosen as an average spectral representation of array source. In reality the signals that were recorded would be due to a combination of array azimuths and tilt elevations as the seismic survey progressed.

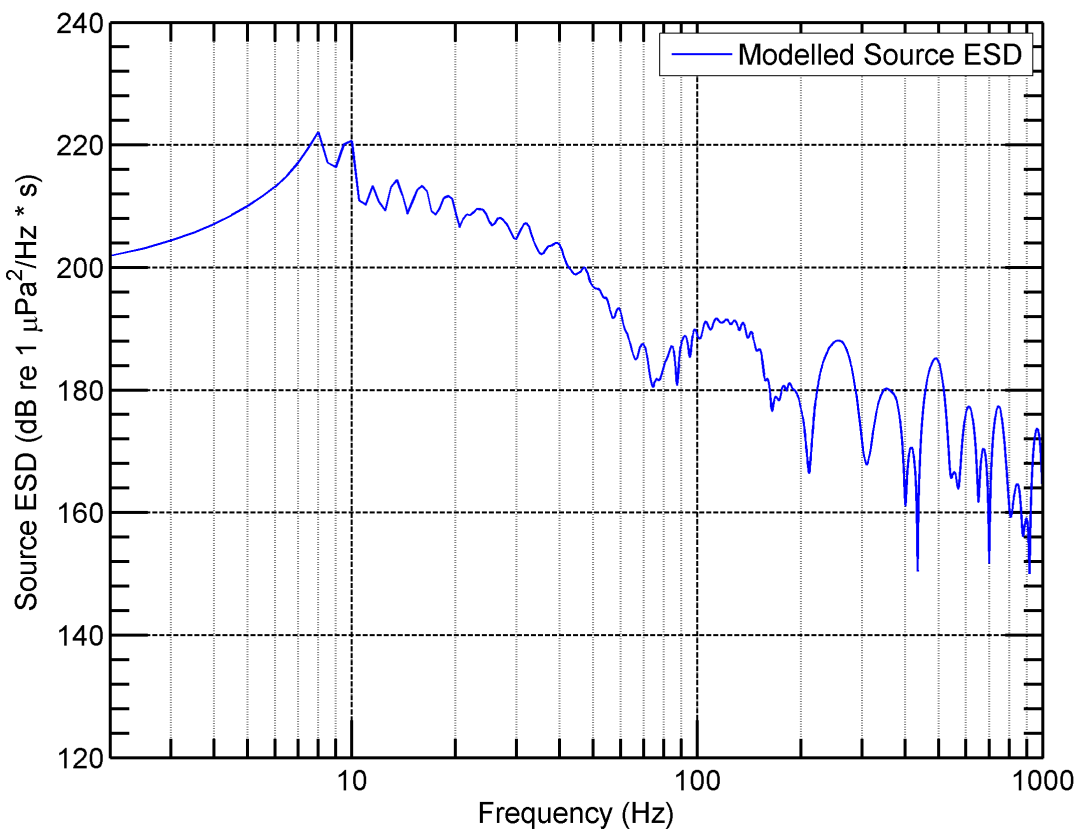


Figure 5.20: The source spectrum from CMST's airgun array model that was used to compute the synthetic SELs. This spectrum represents an equivalent point source of the airgun array at one metre from the source centre.

The following procedure was implemented to produce synthetic SEL results:

- The transmission loss was calculated using SANMO and LAYROTVARS.
- The source model was run with the array configuration parameters to provide the source energy spectral density (Duncan & McCauley, 2000; Duncan et al., 2008). This model used the configuration of airguns that was used for the survey and was supplied by the seismic contractors who conducted the survey. This configuration included the relative geometry of all the airguns, as well as their individual volumes and pressures required by the airgun array model.
- Equations (5.2) and (5.3) were used to compute the SEL where $E_m(\vec{r})$ was obtained from the source model and $P_{TL}(\vec{r}, \omega_{0,m})$ was obtained from one of the propagation models. The source spectrum was split into 1 Hz wide bands with centre frequencies ranging from 2 Hz to 100 Hz.
- The measured signals were low pass filtered prior to calculating the SEL. The filter was an 8th order Butterworth filter with a corner frequency of 100 Hz. This filter was applied to facilitate comparison with the synthetic SELs.
- Equation (5.1) was used to compute the SELs from the measured data.

Figure 5.21 shows the results of this calculation (SEL) using the transmission loss from LAYROTVARS and SANMO.

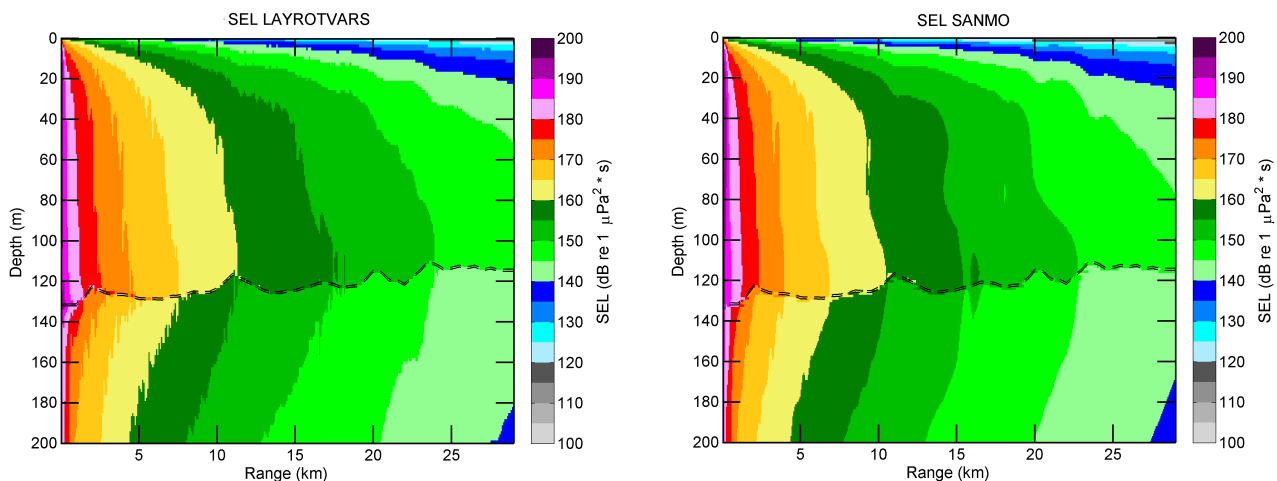


Figure 5.21: A comparison of modelled SEL cross-sections using the source spectrum in Figure 5.20 combined with the transmission loss from LAYROTVARS and SANMO.

The black dotted lines define the seafloor and the calcarenite cap-rock layer.

Figure 5.22 shows the synthetic SELs compared to the SELs computed from the data. Note that the receiver depth (Z_{RX}) is defined as 6 m because the source and receivers were swapped to facilitate this comparison.

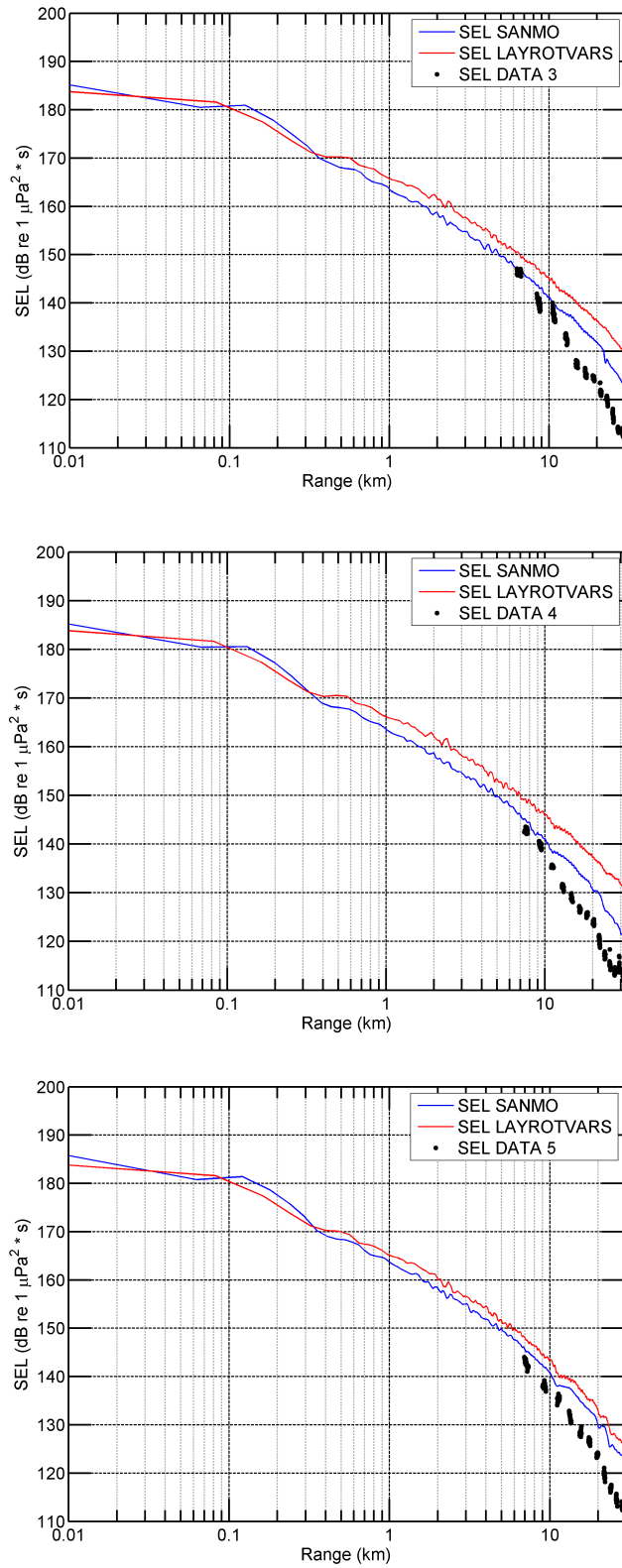


Figure 5.22: SELs computed from measured data and synthetic SELs obtained using the airgun array model source spectrum with SANMO and LAYROTVARS models.

The first observation is that all the measured SELs are lower than the synthetic SELs; secondly the SELs obtained using the PE propagation model to calculate the transmission loss are larger than the SELs produced using the adiabatic normal mode model.

The differences between the measured and the synthetic SELs can be explained considering the uncertainty in the geoacoustic parameters used to produce the transmission loss prediction. While the best possible estimates of the geoacoustic parameters available from prior studies were used to produce the transmission loss, the accuracy of these parameters is uncertain and small errors could have a large impact on the synthetic SEL values. In particular since the majority of the low frequency energy for signals propagating over a calcarenite bottom is focussed in narrow frequency bands, the transmission loss within these bands is sensitive to small errors from incorrect geoacoustic parameters. These can then result in large differences between the SELs. Moreover, since these narrow bands are also sensitive to variations in the range dependent bathymetry profiles, errors in the assumed profiles can also result in difference in the measured and synthetic SELs.

Since the difference in the measured and synthetic SELs widens as the range increases the deviation may be due to an error in either shear wave speed or attenuation because these parameters act to reduce the amplitude of water born propagating modes (see Chapter 3). Therefore, adjusting either of these parameters may lead to a better agreement between the synthetic and measured SELs. Considering that the geotechnical borehole was only drilled to a depth of 100 m below the seafloor and that the shear speed in the third layer was estimated from data obtained at the bottom of the borehole, the value for this layer could be significantly different from actual shear speed values. Moreover, because the shear speeds in the sub-bottom are based on this single borehole, it seemed reasonable to investigate the effect of increasing the shear wave speed in the layers below the cap-rock layer. The shear speed values of 550 m/s and 650 m/s that were used in the modelling described above are at the lower end of the range of shear wave speeds for calcarenite that have been discussed in other studies (see Chapter 3).

To test this hypothesis the shear wave speed in the second and third layers were increased by 100 m/s to 650 m/s and 750 m/s respectively and SANMO and LAYROTVARS were run again for all frequencies, and the SELs were re-calculated. A sample result comparing the data, the new synthetic SELs and the old synthetic SELs is shown below in Figure 5.23. Figure 5.24 shows the results for the new synthetic SELs and the data for tracks 3 through 5 considering the results from SANMO only.

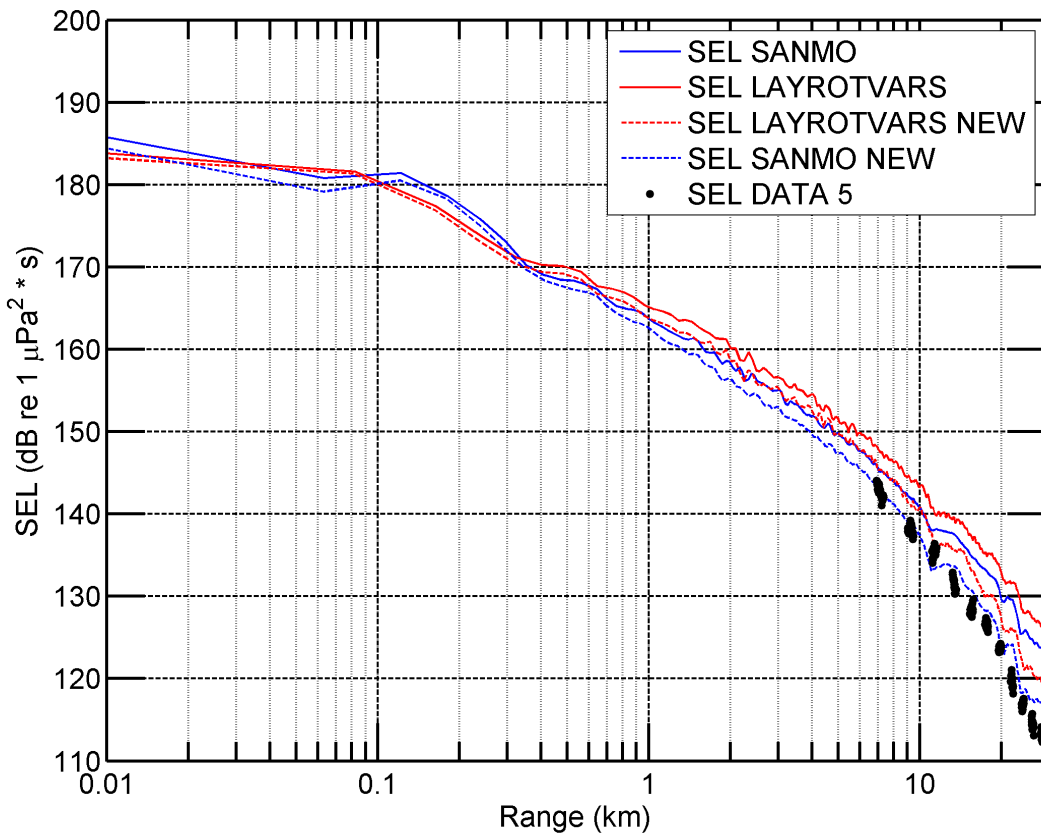


Figure 5.23: SELs computed from measured data and new synthetic SELs (Track 5) obtained using the airgun array model source spectrum with SANMO and LAYROTVARS models (dashed lines) and the previous synthetic SELs in Figure 5.22.

From these figures the agreement between SEL predicted from SANMO with the updated geoacoustic profile and the SELs derived from data is much better. There are still some small differences between the synthetic SELs and the measured SELs but they are on the order of 1 dB rather than 10 dB.

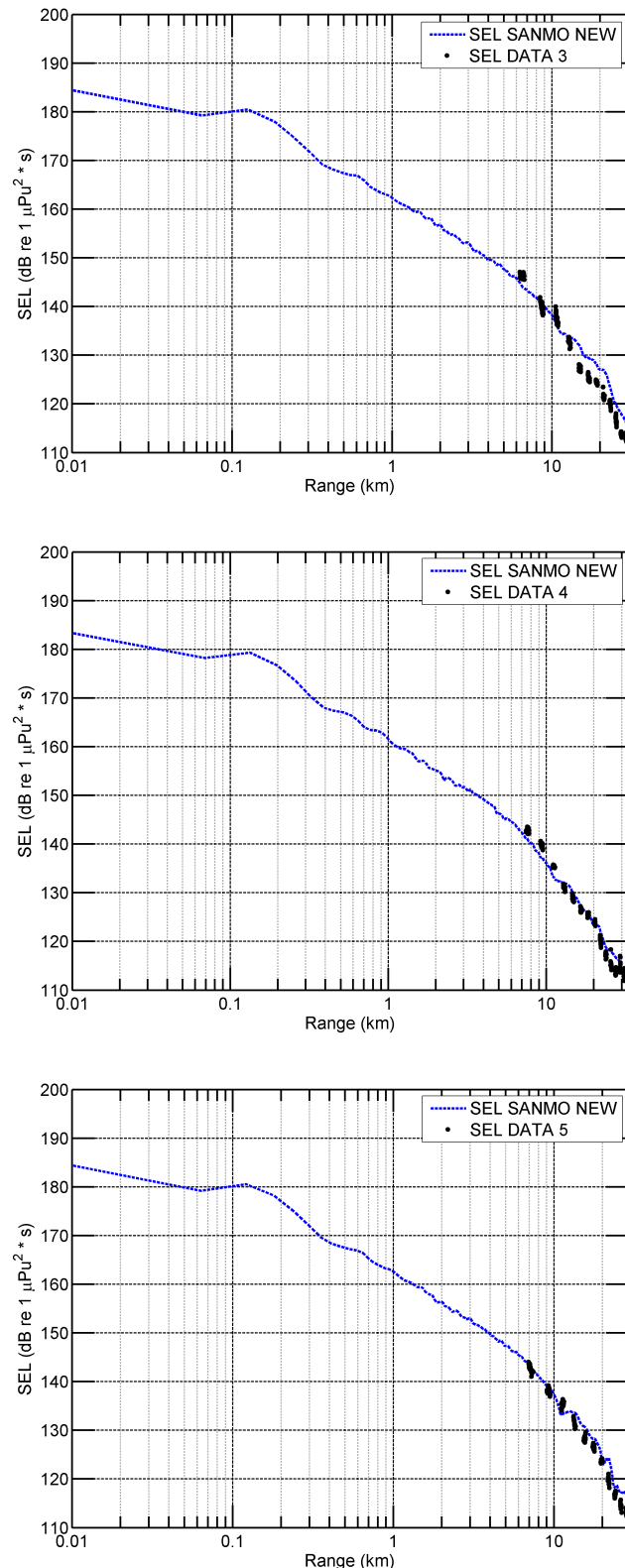


Figure 5.24: SELs computed from measured data and synthetic SELs obtained using the airgun array model source spectrum with SANMO and the updated geoacoustic profile.

5.3 Discussion: An Assessment of the Modelling Methods for Propagation over a Range Dependent Layered Elastic Seabed

The difference between the synthetic SELs (SANMO and LATROTVARS) are due to differences in the predicted transmission loss since the same source spectrum was used. In particular, differences in the transmission loss at low frequencies less than 10 Hz (see Figure 5.10), where LAYROTVARS predicts lower loss than SANMO, are likely to be a major contributor to this difference. The side lobes predicted by LATROTVARS would also affect the synthetic SEL relative to SANMO, but to a lesser extent. Moreover, from section 5.1.3 it is unclear whether these side lobes are indeed correct physical predictions.

An increase in the shear wave speed in the second and third layers of the geoacoustic model resulted in a better fit between the synthetic SELs and the measured SELs. This highlights the effect that the sea bottom geoacoustic parameters have on the water column acoustic field. A parameter study would help isolate which parameters influence SELs the most and by how much. Geoacoustic inversion studies in particular would help reduce the uncertainty in the parameters that are used to describe calcarenite in Bass Strait. Ultimately more data should be collected, analysed, and modelled to build up a statistical representation of range dependent propagation over calcarenite seabeds around Australia.

An important result of this analysis is the different computational efficiencies of the two modelling methods. The majority of the computational time compute the synthetic SELs is incurred by the propagation models that compute the transmission loss; the time to evaluate Equation (5.2) and (5.3) which are used to compute the SELs was about 1 minute per track once the transmission loss has been computed. Given that uncertainties in the chosen geoacoustic parameters may be influencing the agreement between the synthetic SELs and SELs obtained from measurements, a parameter study as discussed above could be conducted to build a statistical estimate of the synthetic SEL. However, any such parameter study using the LAYROTVARS method, at least in the same way that it has been used here, would require a large amount of time. Thus for modelling this type of range dependent environment, the seismoacoustic single-scatter rotated coordinate PE model may not be practically appropriate.

Although the adiabatic mode method is based on a theoretical approximation and therefore may be less accurate than the PE method, trade off in computational efficiency outweighs the shortcomings in the adiabatic modelling method for these scenarios. Furthermore, since measured data can be notoriously difficult to model, as seen here, the combined use of the two methods could be very useful. The PE method could be used to benchmark the adiabatic mode method at a selected number or frequencies that are important to the problem at hand (for example, the cutoff frequencies a few modes) then a wider analysis could be conducted with the adiabatic mode method.

5.4 Summary

5.4.1 Numerical Results

The work presented in section 5.1 investigated the use of an adiabatic seismoacoustic normal mode model (SANMO) for sound propagation modelling over range dependent layered calcarenite seabeds. While further testing is required, the work presented here demonstrates that the adiabatic mode method can produce results that are consistent with a reference seismoacoustic PE (LAYROTVARS) model in a small fraction of the time. An important consideration is the computational cost of modelling. For the broadband scenarios considered here computational costs were on the order of days for the LAYROTVARS but only hours for SANMO. The computational cost per frequency was constant at about 2 hrs per calculation for LAYROTVARS, compared to 30 seconds at low frequencies to 3 minutes at the higher frequencies for SANMO. The increase in computational cost for SANMO is related to an increase in the number of modes found as frequencies increase.

For some applications, such as geoacoustic inversion studies, many calculations would have to be conducted (on the order of 1,000s-10,000s for full broadband inversion (Chapman et al., 2003)), in which case execution time is critically important. With this in mind the adiabatic mode method may be considered as a useful alternative for many scenarios involving complex sea bottoms with thin elastic layers.

5.4.2 SEL Measurements and Simulated SEL

Section 5.2 presents data acquired from a seismic survey operating over the continental shelf in Bass Strait. Generally, these data contained signals with the majority of energy concentrated at low frequencies below 100 Hz. A comparison was conducted between SELs computed from the recorded signals and synthetic SELs derived from the combination of numerical airgun array model and transmission loss from SANMO and LAYROTVARS. The synthetic SEL results from both models were initially higher and disagreed with the SELs from the measured data. Increasing the shear wave speed in the second and third layers of the seabed geoacoustic model and re-computing the transmission loss resulted in better fit between the synthetic SELs and the measured SELs. The important result is that both the PE and adiabatic mode models are capable of modelling these data that are associated with layered elastic seabeds and that the adiabatic mode method efficiently produces accurate results for these scenarios.

To re-run LAYROTVARS with any new geoacoustic parameters (e.g. the shear speeds were changed here) it would take about 9 days to re-model all three datasets, compared to SANMO that took about 1.5 hours. Thus for modelling of this type of range dependent environment consisting of thick and thin calcarenite layers the seismoacoustic single-scatter rotated coordinate PE model is not practically appropriate because of the long runtimes. For scenarios with a greater degree of range dependence that required broadband modelling or modelling of multiple tracks a dual modelling approach could be employed. The first step would be to evaluate the accuracy of SANMO relative to LAYROTVARS for some select cases, such as important frequencies or the most range dependent tracks. Then more comprehensive modelling could be conducted with the adiabatic mode method. Used in this way the combination of the two methods would represent a good balance between efficiency and accuracy for application where elastic layers and range dependence cannot be ignored.

CHAPTER 6 Conclusions and Further Research Avenues

6.1 Conclusions

The main conclusions from this thesis come from Chapter 4 and Chapter 5. These Chapters demonstrates the use of the adiabatic seismoacoustic normal mode method for underwater acoustic propagation modelling. This work investigates the applicability of adiabatic modes to model range dependent acoustic propagation over elastic sea bottoms. While the adiabatic normal mode approach has been a common method for modelling range dependent propagation, the novelty of its use here is centred on its application to range dependent seismoacoustic problems.

6.1.1 Seismoacoustic Adiabatic Normal Modes in the Elastic Wedge Environment

The ASA elastic wedge environment was considered in Chapter 4 as a formal benchmark for the seismoacoustic adiabatic normal mode method SANMO. Two seismoacoustic parabolic equation methods, RAMSGEO and LAYROTVARS, were considered as reference models that would provide accurate solutions for the elastic wedge and were compared to SANMO. Generally, accuracy to within about 2 dB could be achieved with the adiabatic mode method relative to the PE methods. An elastic false bottom and an attenuating Airy halfspace were tested as two different approaches to model the elastic bottom of the ASA wedge. The Airy halfspace approach produced the smallest differences relative to the reference models for range dependent propagation. Furthermore, the attenuating Airy halfspace was found to produce stable and consistent solutions when incorporated into the adiabatic mode method for range dependent propagation over the elastic bottom of the wedge environment.

6.1.2 Modelling Range Dependent Propagation over Layered Elastic Seafloors

Chapter 5 considered range dependent propagation with variable bathymetry and an underlying layered structure of cemented and semi-cemented calcarenite. Transmission loss results from SANMO and LAYROTVARS were found to be in

good agreement. Some differences in the water column transmission loss at low frequencies and/or long ranges were observed; however most of these differences occurred in regions of high transmission loss and are not as important as differences when transmission loss is low. Some differences between the SANMO and LAYROTVARS were attributed to mode coupling, which is ignored in the adiabatic approximation used by SANMO. In an example the inclusion of mode coupling by way of an approximate single-scatter acoustic mode coupling algorithm with mode functions from ORCA accounted for these differences in transmission loss relative to LAYROTVARS.

The synthetic SELs computed using the transmission loss output from SANMO and LAYROTVARS were compared to SELs from measured signals. When initially comparing SELs computed from measurement and synthetic SELs, the synthetic SELs were larger. Errors in the geoacoustic parameters were hypothesised as the likely cause of this difference. The shear wave speeds in two layers were increased by 100 m/s and the propagation models were re-run and synthetic SELs were re-calculated. The new synthetic SELs from SANMO agreed much better with the measured SELs.

One of the main results of this work is the demonstration that there are large differences between the computational costs of the PE model and the adiabatic normal mode model. Each propagation model was run considering a band of low frequencies from 2 Hz to 100 Hz incremented at 1 Hz, maximum ranges between 30 kilometres and 70 kilometres, and water depths on the order of 130 metres, with a seabed composed of layered cemented and semi-cemented calcarenite. For the 70 kilometre case, LAYROTVARS required a total runtime of 7 days for a single broadband calculation, whereas SANMO completed the required calculations in 2.5 hours. Therefore in situations where multiple calculations are required LAYROTVARS would be impractical to use because of the long computational runtimes, which are on the order of hours per frequency. This does not suggest that LAYROTVARS or other PE models may not be efficient for other environments, but for range dependent layered calcarenite environments when one or more elastic layers are thin relative to the wavelength and when multiple calculations (i.e. many

frequencies or many tracks) are required, their use is impractical. This further supports that it is a difficult environment to model.

The high efficiency of SANMO that has been demonstrated in this thesis is an important result for practical applications such as the generation of synthetic SEL predictions discussed in Chapter 5. For range dependent environments that are similar to those discussed here, the adiabatic mode method would be very useful for applications that require broadband calculations. Examples of such application would include environmental impact assessments or geoacoustic inversion studies.

In underwater acoustics, the parabolic equation method has been the favoured method for modelling range dependent propagation; however, despite the advances in the numerical technique there are some scenarios where the PE method is not practical. The main aim of this thesis has been to present a numerical sound propagation model that can both accurately and efficiently model range dependent acoustic propagation over layered calcarenite seabeds. Considering these two points, the seismoacoustic adiabatic normal mode model has been shown to produce results with sufficient accuracy and with high efficiency. So when the PE method is not applicable, range dependent normal modes can serve as a useful alternative.

6.2 Future Research Opportunities

The computational efficiency of SANMO may be further improved by re-writing the numerical routine, currently coded in Matlab, in a more efficient computer language such as Fortran or C. A relatively large amount of time is incurred by reading the output files from ORCA, which are required to perform the adiabatic transmission loss calculation, into Matlab. Performing the adiabatic calculations using a single programming language and running the algorithm as an executable would significantly improve the computational efficiency of SANMO.

The comparison of numerical results from SANMO, RAMSGEO, and LAYROTVARS with other experimental data collected around Australia would help better understand the range dependent propagation characteristics associated with calcarenite seafloors. While range dependent propagation modelling of

environments with calcarenite seafloors has posed numerical difficulties, the uncertainty in bottom geoacoustic parameters associated with different types of calcareous seafloors is an equally important limitation to the accuracy of modelling. For calcarenite seafloors around Australia these uncertainties are large, mainly due to a scarcity of appropriate measured data. A comparison of more numerical and measured data would be used to build a geo-spatial database of geoacoustic parameters that would help to reduce this uncertainty.

This work suggests that the development of a range dependent seismoacoustic coupled normal mode propagation model may be an avenue for further research. Any such propagation model would have to satisfy the elastic energy flux conditions at a vertical interface to ensure realistic numerical solutions and numerical stability. This may take the form as a correction factors as discussed by (Collins, 1993a; Collins & Siegmann, 1999), or a single-scatter approximations to the coupling equations discussed by Park and Odom (1998) and shown in Equation (4.3). Moreover, an unknown at the moment is the consequence of including 3-D propagation effects with calcarenite seafloors. Considering the work of Ballard (2012) it may be possible to extend use of normal modes further to model 3-D environments with elastic seabeds

References

- Abramowitz, M., & Stegun, I. (1965). *Handbook of mathematical functions: with formulas, graphs and mathematical tables*: National Bureau of Standards
- Ainslie, M. A. (1995). Plane-wave reflection and transmission coefficients for a three-layered elastic medium. *The Journal of the Acoustical Society of America*, 97(2), 954-961.
- Aki, K., & Richards, P. G. (1980). *Quantitative Seismology*. San Francisco: W. H. Freeman
- Arfken, G. (1970). *Mathematical Methods For Physicsts* (Second ed.). New York: Academic Press.
- Arvelo, J. I. (1990). Adiabatic normal-mode theory of sound propagation including shear waves in a range-dependent ocean floor. *The Journal of the Acoustical Society of America*, 88(5), 2316.
- Auld, B. A. (1973). *Acoustic field and waves in solids: vol. II*. New York: Wiley.
- Ballard, M. S. (2012). Modeling three-dimensional propagation in a continental shelf environment. *The Journal of the Acoustical Society of America*, 131(3), 1969-1977.
- Ballard, M. S., Goldsberry, B. M., & Isakson, M. J. (2015). Normal Mode Analysis of Three-Dimensional Propagation Over a Small-Slope Cosine Shaped Hill. *Journal of Computational Acoustics*, 23(03), 1550005.
- Ben-Menahem, A., & Singh, S. J. (1981). *Seismic Waves and Sources*. New York: Springer-Verlag.
- Beringen, F., Kolk, H., & Windle, D. (1982). Cone penetration and laboratory testing in marine calcareous sediments. *ASTM STP*, 777, 179-209.
- Biot, M. A. (1956). Theory of Propagation of Elastic Waves in a Fluid-Saturated Porous Solid. II. Higher Frequency Range. *The Journal of the Acoustical Society of America*, 28(2), 179-191.
- Bird, E. C. F. (1979). Geomorphology of the sea floor around Australia. In J. R. V. Prescott (Ed.), *Australia's Continental Shelf*. Melbourne: Thomas Nelson (Australia) in association with the Australian Institute of International Affairs
- Boyles, C. A. (1984). *Acoustic waveguides: applications to oceanic science*. New York, NY: John Wiley and Sons Inc.

Brekhovskikh, L. M., & Godin, O. A. (1990). *Acoustics of layered media I: plane and quasi-plane waves*. Berlin Heidelberg: Springer-Verlag.

Brekhovskikh, L. M., & Godin, O. A. (1992). *Acoustics of layered media II: point sources and bounded beams*. Berlin Heidelberg: Springer-Verlag.

Brown, J. W., Churchill, R. V., & Lapidus, M. (1996). *Complex variables and applications* (Vol. 7): McGraw-Hill New York.

Bucker, H. P. (1970). Sound Propagation in a Channel with Lossy Boundaries. *The Journal of the Acoustical Society of America*, 48(5B), 1187-1194.

Carey, W. M. (2006). Sound sources and levels in the ocean. *IEEE Journal of Oceanic Engineering*, 31(1), 61-75.

Chapman, N. R., & Chapman, D. M. F. (1993). A coherent ray model of plane-wave reflection from a thin sediment layer. *The Journal of the Acoustical Society of America*, 94(5), 2731-2738.

Chapman, N. R., Chin-Bing, S., King, D., & Evans, R. B. (2003). Benchmarking geoacoustic inversion methods for range-dependent waveguides. *IEEE Journal of Oceanic Engineering*, 28(3), 320-330.

Chin-Bing, S. A., King, D. B., Davis, J. A., & Evans, R. B. (1993). *PE Workshop II. Proceedings of the Second Parabolic Equation Workshop*

Clark, A. C. (2012). Wave Propagation Prediction Over a Thin Elastic Sediment and Rock Basement. *IEEE Journal of Oceanic Engineering*, 37(3), 494-506.

Collins, L. B. (1988). Sediments and history of the Rottnest Shelf, southwest Australia: a swell-dominated, non-tropical carbonate margin. *Sedimentary Geology*, 60(1-4), 15.

Collins, M. D. (1989a). A higher-order parabolic equation for wave propagation in an ocean overlying an elastic bottom. *The Journal of the Acoustical Society of America*, 86(4), 1459-1464.

Collins, M. D. (1989b). A higher-order parabolic equation for wave propagation in an ocean overlying an elastic bottom. *The Journal of the Acoustical Society of America*, 86(4), 1459-1464.

Collins, M. D. (1993a). An energy-conserving parabolic equation for elastic media. *The Journal of the Acoustical Society of America*, 94(2), 975-982.

Collins, M. D. (1993b). A split-step Pade solution for the parabolic equation method. *The Journal of the Acoustical Society of America*, 93(4), 1736-1742.

- Collins, M. D., & Siegmann, W. L. (1999). A complete energy conservation correction for the elastic parabolic equation. *The Journal of the Acoustical Society of America*, 105(2), 687-692.
- Collins, M. D., & Siegmann, W. L. (2015). Treatment of a sloping fluid-solid interface and sediment layering with the seismo-acoustic parabolic equation. *The Journal of the Acoustical Society of America*, 137(1), 492-497.
- Collis, J. M., & Metzler, A. M. (2014). Seismo-acoustic propagation near thin and low-shear speed ocean bottom sediments using a massive elastic interface. *The Journal of the Acoustical Society of America*, 135(1), 115-123.
- Collis, J. M., Siegmann, W. L., Collins, M. D., Simpson, H. J., & Soukup, R. J. (2007). Comparison of simulations and data from a seismo-acoustic tank experiment. *The Journal of the Acoustical Society of America*, 122(4), 1987-1993.
- Collis, J. M., Siegmann, W. L., Jensen, F. B., Zampolli, M., Kusel, E. T., & Collins, M. D. (2008). Parabolic equation solution of seismo-acoustics problems involving variations in bathymetry and sediment thickness. *The Journal of the Acoustical Society of America*, 123(1), 51-55.
- Collis, J. M., Siegmann, W. L., Zampolli, M., & Collins, M. D. (2009). Extension of the Rotated Elastic Parabolic Equation to Beach and Island Propagation. *IEEE Journal of Oceanic Engineering*, 34(4), 617-623.
- Dahl, P. H., Dall'Osto, D. R., & Farrell, D. M. (2015). The underwater sound field from vibratory pile driving. *The Journal of the Acoustical Society of America*, 137(6), 3544-3554.
- Duncan, A., & McCauley, R. (2000). *Characterisation of an air-gun as a sound source for acoustic propagation studies*. Proceedings of UDT Pacific 2000 Conference, Sydney, Australia.
- Duncan, A. J., & Gavrilov, A. (2012, Nov. 21-23). *Low frequency acoustic propagation over calcarenite seabeds with thin, hard caps*. Proceedings of Acoustical Society of Australia, Acoustics 2012, Fremantle, Australia.
- Duncan, A. J., Gavrilov, A., & Fan, L. (2009). *Acoustic propagation over limestone seabeds*. Proceedings of Acoustical Society of Australia, Acoustics 2009, Adelaide, Australia.
- Duncan, A. J., Gavrilov, A., & Hu, T. (2008). *Using offshore seismic surveys as acoustic sources of opportunity for geoacoustic inversion*. Proceedings of Acoustics '08, Paris, France.

- Duncan, A. J., Gavrilov, A. N., McCauley, R. D., Parnum, I. M., & Collis, J. M. (2013). Characteristics of sound propagation in shallow water over an elastic seabed with a thin cap-rock layer. *The Journal of the Acoustical Society of America*, 134(1), 207-215.
- Duncan, A. J., & McCauley, R. D. (2008). *Envrionmetal Impact Assessment of Underwater Sound: Progress and Pitfalls*. Proceedings of Acoustical Society of Australia, Acoustics 2008, Geelong, Victoria, Australia.
- Dunham, R. J. (1962). *Classification of carbonate rocks according to depositional textures*. Tusla: AAPG.
- Ellis, D. D., & Chapman, D. M. F. (1985). A simple shallow water propagation model including shear wave effects. *The Journal of the Acoustical Society of America*, 78(6), 2087-2095.
- Erbe, C. (2013). International regulation of underwater noise. *Acoustics Australia*, 41(1), 5.
- Etter, P. C. (2013). *Underwater acoustic modeling and simulation* (Fourth ed.): CRC Press.
- Evans, R. B. (1983). A coupled mode solution for acoustic propagation in a waveguide with stepwise depth variations of a penetrable bottom. *The Journal of the Acoustical Society of America*, 74(1), 188-195.
- Ewing, W. M., Jardetzky, W. S., & Press, F. (Eds.). (1957). *Elastic waves in layered media*. New York: McGraw-Hill.
- Fan, L., Duncan, A. J., & Gavrilov, A. (2009). *Propagation and Inversion of Airgun Signals in Shallow Water Over a Limestone Seabed*. Paper presented at the 3rd International Conference & Exhibition on " Underwater Acoustic Measurments: Technologies & Results", Nafplion, Greece.
- Feeary, D., Hine, A., & Malone, M. (2000). *Leg 182 summary: Great Australian Bight-Cenozoic cool-water carbonates*. Proceedings of Proceedings of the Ocean Drilling Program, Part A: Initial Reports.
- Feeary, D. A., & James, N. P. (1998). Seismic stratigraphy and geological evolution of the Cenozoic, cool-water Eucla Platform, Great Australian Bight. *AAPG Bulletin*, 82(5A), 792-816.
- Flugel, E., & Munnecke, A. (2010). *Microfacies of carbonate rocks: analysis, interpretation and application*: Springer-Verlag.
- Frisk, G. V. (1994). *Ocean and seabed acoustics: a theory of wave propagation*: Pearson Education.

Fugro. (2004). *Draft geotechnical report, Otway gas project, final platform geotechnical investigation, offshore Victoria Australia* (Fugro Survey Report No. HY 16608, Fugro Engineers BV Report No. N3449/02)

Gavrilov, A., Duncan, A., McCauley, R., & Parnum, I. (2012). *Peculiarities of sound propagation over the continental shelf in Bass Strait*. Proceedings of The 11th European Conference on Underwater Acoustics, Edinburgh.

Godin, O. A. (2002). A 2-D description of sound propagation in a horizontally-inhomogeneous ocean. *Journal of Computational Acoustics*, 10(01), 123-151.

Godin, O. A. (2003). On derivation of differential equations of coupled-mode propagation from the reciprocity principle (L). *The Journal of the Acoustical Society of America*, 114(6), 3016-3019.

Goh, J. T., & Schmidt, H. (1996). A hybrid coupled wave-number integration approach to range-dependent seismoacoustic modeling. *The Journal of the Acoustical Society of America*, 100(3), 1409-1420.

Goh, J. T., Schmidt, H., Gerstoft, P., & Seone, W. (1997). Benchmarks for validating range-dependent seismo-acoustic propagation codes. *IEEE Journal of Oceanic Engineering*, 22(2), 226-236.

Gostin, V. A., Belperio, A. P., & Cann, J. H. (1988). The Holocene non-tropical coastal and shelf carbonate province of southern Australia. *Sedimentary Geology*, 60(1-4), 51-70.

Grabau, A. W. (1903). Paleozoic coral reefs. *Geological Society of America Bulletin*, 14(1), 337-352.

Greene, R. R. (1985). A high-angle one-way wave equation for seismic wave propagation along rough and sloping interfaces. *The Journal of the Acoustical Society of America*, 77(6), 1991-1998.

Hall, M. V. (1995). Acoustic reflectivity of a sandy seabed: A semianalytic model of the effect of coupling due to the shear modulus profile. *The Journal of the Acoustical Society of America*, 98(2), 1075-1089.

Hall, M. V. (2004). Preliminary analysis of the applicability of adiabatic modes to inverting synthetic acoustic data in shallow water over a sloping sea floor. *IEEE Journal of Oceanic Engineering*, 29(1), 51-58.

Hamilton, E. L. (1980). Geoacoustic modeling of the sea floor. *The Journal of the Acoustical Society of America*, 68(5), 1313.

Hamilton, E. L. (1982). Sound velocity and related properties of marine sediments. *The Journal of the Acoustical Society of America*, 72(6), 1891.

Holland, C. W., & Brunson, B. A. (1988). The Biot–Stoll sediment model: An experimental assessment. *The Journal of the Acoustical Society of America*, 84(4), 1437-1443.

Hovem, J. M. (2012). *Marine Acoustics: The Physics of Sound in Underwater Environments*. Los Altos Hills CA: Peninsula Publishing.

Hovem, J. M., & Kristensen, A. (1992). Reflection loss at a bottom with a fluid sediment layer over a hard solid half-space. *The Journal of the Acoustical Society of America*, 92(1), 335-340.

Hughes, S. J., Ellis, D. D., Chapman, D. M. F., & Staal, P. R. (1990). Low-frequency acoustic propagation loss in shallow water over hard-rock seabeds covered by a thin layer of elastic–solid sediment. *The Journal of the Acoustical Society of America*, 88(1), 283-297.

Jackson, D. R., & Richardson, M. D. (2007). *High-Frequency Seafloor Acoustics*. New York, NY: Springer Science+Business Media, LLC.

James, N. P., & Bone, Y. (2011). *Neritic Carbonate Sediments in a Temperate Realm*: Springer Netherlands.

James, N. P., Boreen, T. D., Bone, Y., & Feary, D. A. (1994). Holocene carbonate sedimentation on the west Eucla Shelf, Great Australian Bight: a shaved shelf. *Sedimentary Geology*, 90(3–4), 161-177.

James, N. P., Feary, D. A., Betzler, C., Bone, Y., Holbourn, A. E., Li, Q., . . . Surlyk, F. (2004). Origin of Late Pleistocene Bryozoan Reef Mounds; Great Australian Bight. *Journal of Sedimentary Research*, 74(1), 20-48.

Jensen, F. B. (1982, 20-22 Sept. 1982). *Numerical Models of Sound Propagation in Real Oceans*. Proceedings of OCEANS 82, Washington, D.C., USA.

Jensen, F. B., & Ferla, C. M. (1990). Numerical solutions of range-dependent benchmark problems in ocean acoustics. *The Journal of the Acoustical Society of America*, 87(4), 1499-1510.

Jensen, F. B., Kuperman, W. A., Porter, M. B., & Schmidt, H. (2011a). *Computational Ocean Acoustics*.

Jensen, F. B., Kuperman, W. A., Porter, M. B., & Schmidt, H. (2011b). *Normal Modes Computational Ocean Acoustics*. New York: Springer

Jensen, F. B., Kuperman, W. A., Porter, M. B., & Schmidt, H. (2011c). *Parabolic Equations Computational Ocean Acoustics*. New York: Springer

Katsnelson, B., Petnikov, V., & Lynch, J. (2012). *Fundamentals of shallow water acoustics*: Springer Science & Business Media.

Kennett, B. L. N. (1984a). Guided wave propagation in laterally varying media - I. Theoretical development. *Geophysical Journal of the Royal Astronomical Society*, 79(1), 235-255.

Kennett, B. L. N. (1984b). Guided wave propagation in laterally varying media — I. Theoretical development. *Geophysical Journal International*, 79(1), 235-255.

Koch, R. A., Penland, C., Vidmar, P. J., & Hawker, K. E. (1983). On the calculation of normal mode group velocity and attenuation. *The Journal of the Acoustical Society of America*, 73(3), 820-825.

Kolsky, H. (1963). *Stress Waves in Solids*. New York: Dover.

Küsel, E. T., Siegmann, W. L., & Collins, M. D. (2007). A single-scattering correction for large contrasts in elastic layers. *The Journal of the Acoustical Society of America*, 121(2), 808-813.

Lin, Y.-T., Collis, J. M., & Duda, T. F. (2012). A three-dimensional parabolic equation model of sound propagation using higher-order operator splitting and Padé approximants. *The Journal of the Acoustical Society of America*, 132(5), EL364-EL370.

Maupin, V. (1988). Surface waves across 2-D structures: a method based on coupled local modes. *Geophysical Journal International*, 93(1), 173-185.

Mavko, G., Mukerji, T., & Dvorkin, J. (2009). *The rock physics handbook: Tools for seismic analysis of porous media*: Cambridge University Press.

McCollom, B. A., & Collis, J. M. (2014). Root finding in the complex plane for seismo-acoustic propagation scenarios with Green's function solutions. *The Journal of the Acoustical Society of America*, 136(3), 1036-1045.

Metzler, A. M., Siegmann, W. L., & Collins, M. D. (2012). Single-scattering parabolic equation solutions for elastic media propagation, including Rayleigh waves. *The Journal of the Acoustical Society of America*, 131(2), 1131-1137.

Morse, P. M., & Ingard, K. U. (1968). *Theoretical acoustics*: Princeton University Press.

Odom, R. I., Park, M., Mercer, J. A., Crosson, R. S., & Paik, P. (1996). Effects of transverse isotropy on modes and mode coupling in shallow water. *The Journal of the Acoustical Society of America*, 100(4), 2079-2092.

Officer, C. B. (1958). *Introduction to the theory of sound transmission*. New York: McGraw Hill.

Outing, D. A., Siegmann, W. L., Collins, M. D., & Westwood, E. K. (2006). Generalization of the rotated parabolic equation to variable slopes. *The Journal of the Acoustical Society of America*, 120(6), 3534-3538.

Park, M., & Odom, R. I. (1998). Effects of elastic heterogeneities and anisotropy on mode coupling and signals in shallow water. *The Journal of the Acoustical Society of America*, 104(2), 747-757.

Pekeris, C. L. (1948). Theory of propagation of explosive sound in shallow water. *Geological Society of America Memoir*, 27.

Pierce, A. D. (1965). Extension of the Method of Normal Modes to Sound Propagation in an Almost-Stratified Medium. *The Journal of the Acoustical Society of America*, 37(1), 19-27.

Porter, M. B. (1994). Adiabatic modes for a point source in a plane-geometry ocean. *The Journal of the Acoustical Society of America*, 96(3), 1918-1921.

Porter, M. B. (2007). Acoustics Toolbox. Retrieved from <http://oalib.hlsresearch.com/FFP/index.html>

Porter, M. B., Jensen, F. B., & Ferla, C. M. (1991). The problem of energy conservation in one-way models. *The Journal of the Acoustical Society of America*, 89(3), 1058-1067.

Porter, M. B., & Reiss, E. L. (1985). A numerical method for bottom interacting ocean acoustic normal modes. *The Journal of the Acoustical Society of America*, 77(5), 1760-1767.

Press, F., & Ewing, M. (1950). Propagation of explosive sound in a liquid layer overlying a semi-infinite elastic solid. *GEOPHYSICS*, 15(3), 426-446.

Schmidt, H. (2004). OASES version 3.1 user guide and reference manual. Retrieved from <http://oceana.i.mit.edu/lamss/pmwiki/pmwiki.php?n=Site.Oases>

Schmidt, H., Seong, W., & Goh, J. T. (1995). Spectral super-element approach to range-dependent ocean acoustic modeling. *The Journal of the Acoustical Society of America*, 98(1), 465-472.

Schmidt, H., & Tango, G. (1986). Efficient global matrix approach to the computation of synthetic seismograms. *Geophysical Journal of the Royal Astronomical Society*, 84(2), 331-359.

- Schneiderwind, J. D., Collis, J. M., & Simpson, H. J. (2012). Elastic Pekeris waveguide normal mode solution comparisons against laboratory data. *The Journal of the Acoustical Society of America*, 132(3), EL182-EL188.
- Seibold, E., & Berger, W. H. (1996). *The sea floor: an introduction to marine geology*: Springer.
- Stoll, R. D. (1977). Acoustic waves in ocean sediments. *GEOPHYSICS*, 42(4), 715-725.
- Sturm, F. (2005). Numerical study of broadband sound pulse propagation in three-dimensional oceanic waveguides. *The Journal of the Acoustical Society of America*, 117(3), 1058-1079.
- Tindle, C. T., & Chapman, N. R. (1994). A Phase Function for Finding Normal-Mode Eigenvalues over a Layered Elastic Bottom. *The Journal of the Acoustical Society of America*, 96(3), 1777-1782.
- Tindle, C. T., Hobaek, H., & Muir, T. G. (1987). Downslope propagation of normal modes in a shallow water wedge. *The Journal of the Acoustical Society of America*, 81(2), 275-286.
- Tindle, C. T., O'Driscoll, L. M., & Higham, C. J. (2000). Coupled mode perturbation theory of range dependence. *The Journal of the Acoustical Society of America*, 108(1), 76-83.
- Tindle, C. T., & Zhang, Z. Y. (1997). An adiabatic normal mode solution for the benchmark wedge. *The Journal of the Acoustical Society of America*, 101(1), 606-609.
- Urick, R. J. (1967). *Principles of underwater sound for engineers*: Tata McGraw-Hill Education.
- Vidmar, P. J. (1979). A plane-wave reflection loss model including sediment rigidity. *The Journal of the Acoustical Society of America*, 66(6), 1830.
- Vidmar, P. J. (1980a). The effect of sediment rigidity on bottom reflection loss in a typical deep sea sediment. *The Journal of the Acoustical Society of America*, 68(2), 634-638.
- Vidmar, P. J. (1980b). Ray path analysis of sediment shear wave effects on bottom reflection loss. *The Journal of the Acoustical Society of America*, 68(2), 639-648.
- Vidmar, P. J., & Foreman, T. L. (1979). A plane-wave reflection loss model including sediment rigidity. *The Journal of the Acoustical Society of America*, 66(6), 1830-1835.

Westwood, E. K., & Koch, R. A. (1998). Elimination of branch cuts from the normal mode solution using gradient half-spaces. *The Journal of the Acoustical Society of America*, 103(5), 2857.

Westwood, E. K., Tindle, C. T., & Chapman, N. R. (1996). A normal mode model for acousto-elastic ocean environments. *The Journal of the Acoustical Society of America*, 100(6), 3631-3645.

Wetton, B. T. R., & Brooke, G. H. (1990). One-way wave equations for seismoacoustic propagation in elastic waveguides. *The Journal of the Acoustical Society of America*, 87(2), 624-632.

Whiteway, T. (2009). *Australian bathymetry and topography grid, June 2009*: Geoscience Australia, Department of Industry, Tourism and Resources.

Woodhouse, J. H. (1974). Surface waves in a laterally varying layered structure. *Geophysical Journal International*, 37(3), 461.

Yudichak, T. W., Royal, G. S., Knobles, D. P., Gray, M., Koch, R. A., & Stotts, S. A. (2006). Broadband modeling of downslope propagation in a penetrable wedge. *The Journal of the Acoustical Society of America*, 119(1), 143-152.

Ziolkowski, A., Parkes, G., Hatton, L., & Haugland, T. (1982). The signature of an air gun array: Computation from near-field measurements including interactions. *GEOPHYSICS*, 47(10), 1413-1421.

Every reasonable effort has been made to acknowledge the owners of copyright material. I would be pleased to hear from any copyright owner who has been omitted or incorrectly acknowledged.

Appendix A Functional Form of the Adiabatic Approximation

To begin, translationally invariant symmetry in the y -plane is assumed and a spatial Fourier transform is applied to the Cartesian frequency domain stress-displacement vector $\vec{U}(x, y, z; \omega)$ to reduce the y spatial dimension. The spatial Fourier transform pairs from Porter (1994) are defined as,

$$\vec{U}(x, z; k_y; \omega) = \int \vec{U}(x, y, z) e^{-ik_y y} dy \quad (\text{A.1})$$

and

$$\vec{U}(x, y, z; \omega) = \frac{1}{2\pi} \int \vec{U}(x, z; k_y; \omega) e^{ik_y y} dk_y. \quad (\text{A.2})$$

These spatial Fourier transforms are defined such that if Fourier synthesis were carried out, Fourier integral would be integrating the contributions from plane waves of the form,

$$e^{i(\vec{k} \cdot \vec{r} - \omega t)}. \quad (\text{A.3})$$

A note should be made that the Park and Odom (1998) used a different transform convention such that Fourier synthesis would be and integration over plane waves of the form,

$$e^{-i(\vec{k} \cdot \vec{r} - \omega t)}. \quad (\text{A.4})$$

So there is a sign convention that differs between their article and the equations presented here.

As in Equation (4.1) stress-displacement vector can be written as

$$\vec{U}(x, z; k_y; \omega) = \sum_m C_m^\pm(x) \vec{U}_m(z, x) e^{\pm i \int_0^x k_{x,m}(x') dx'}. \quad (\text{A.5})$$

where $C_m^\pm(x)$ are the modal excitation amplitudes produced mode coupling coefficients. These excitation amplitudes evolve in range continuously via the coupling matrix B_{nm} defined by Maupin (1988), Odom et al. (1996), and Park and Odom (1998) as

$$\partial_x C_n(x) = B_{nm} C_m(x). \quad (\text{A.6})$$

When neglecting modal coupling ($B_{nm} = 0$) and assuming that modes only propagate outwardly from a source, the component of Equation (A.5) that only depends on x can be written as,

$$\zeta_m(x) = C_m^+(x) e^{i \int_0^x k_{x,m}(x') dx'} \quad (\text{A.7})$$

such that, $C_m^+(x)$, evolves in range is subject to the integrated phase variations of each modal wavenumber. The rest of this appendix is devoted to determining the form of $C_m^+(x)$ and to show how this definition of the adiabatic approximation for a stress-displacement vector reduces to a standard form for acoustic waves. Considering local normal modes, modal decomposition of the acoustic field in a fluid or the seismic field in an elastic material implies that the solution to (A.5) is of the form

$$\vec{U}(x, z; k_y; \omega) = \sum_m \eta_m(x) \vec{U}_m(z, x) \quad (\text{A.8})$$

It is assumed that the when neglecting coupling terms that both the compressional and shear potentials both potentials satisfy the same range equation, similar to the range independent case. The inhomogeneous range equation that represents an explosive impulse can be written as,

$$\frac{d\eta_m(x)}{dx^2} + v_m^2(x; k_y) \eta_m(x) = -\delta(x) \quad (\text{A.9})$$

where,

$$v^2(x; k_y) = k_{x,m}^2(x) - k_y^2. \quad (\text{A.10})$$

This form of the source is consistent with the generalised source term proposed by Park and Odom (1998) for acoustic or seismic propagation

$$\vec{f}_s(x, z; k_y; \omega) = [f_x \hat{\mathbf{x}} + f_y \hat{\mathbf{y}} + f_z \hat{\mathbf{z}}] S(\omega) \delta(x) \delta(z - z_s). \quad (\text{A.11})$$

The differential in Equation (A.9) has a WKB solution (Arfken 1970, Jensen et al. 2011c) of the form

$$\eta_m(x) = \frac{i}{2} C_m(0, z_s) \frac{e^{i \int_0^x v_m(x') dx'}}{\sqrt{v(0; k_y) v(x; k_y)}} \quad (\text{A.12})$$

where $C_m(0, z_s)$ is an integration constant that is determined by the type of source excitation in Equation (A.11). Equating the WKB for solution $\eta_m(x)$ to the functional from for $\zeta_m(x)$,

$$\eta_m(x) = \frac{i}{2} C_m(0) \frac{e^{i \int_0^x v_m(x') dx'}}{\sqrt{v(0; k_y) v(x; k_y)}} = \zeta_m(x) = C_m^+(x) e^{i \int_0^x k_{x,m}(x') dx'} \quad (\text{A.13})$$

the result is that $C_m^+(x)$ should be of the form

$$C_m^+(x) = \frac{i}{2} C_m(0, z_s) \frac{1}{\sqrt{\nu_m(0; k_y) \nu_m(x; k_y)}}. \quad (\text{A.14})$$

So the transformed stress-displacement vector potential becomes

$$\vec{U}(x, z; k_y) = \frac{i}{2} \sum_m C_m(0, z_s) \frac{e^{i \int_0^x \nu_m(x') dx'}}{\sqrt{\nu_m(0; k_y) \nu_m(x; k_y)}} \vec{U}_m(z, x) \quad (\text{A.15})$$

however a solution for $\vec{U}(x, y, z)$ is required not $\vec{U}(x, z; k_y)$. Applying the inverse transform (Equation (A.2)) to $\vec{U}(x, z; k_y)$, $\vec{U}(x, y, z)$ can then be written as

$$\vec{U}(x, y, z) = \frac{i}{4\pi} \int \sum_m C_m(0, z_s) \frac{e^{i \int_0^x \nu_m(x') dx'}}{\sqrt{\nu_m(0; k_y) \nu_m(x; k_y)}} \vec{U}_m(z, x) e^{ik_y y} dk_y \quad (\text{A.16})$$

which can be written in the form

$$\vec{U}(x, y, z) = \frac{i}{4\pi} \sum_m C_m(0, z_s) \vec{U}_m(z, x) I_m(x, y) \quad (\text{A.17})$$

where

$$I_m(x, y) = \int \frac{e^{i \int_0^x \nu_m(x') dx'}}{\sqrt{\nu_m(0; k_y) \nu_m(x; k_y)}} e^{ik_y y} dk_y. \quad (\text{A.18})$$

Applying the stationary phase approximation to the integral $I_m(x, y)$ and taking the out of plain horizontal axis $y = 0$ to be the point of stationary phase, the integral in (A.18) reduces to,

$$I_m(x, 0) \approx \frac{\sqrt{2\pi} e^{-i\frac{\pi}{4}} e^{i \int_0^x k_{x,m}(x') dx'}}{\sqrt{k_{x,m}(0) k_{x,m}(x) \int_0^x \frac{1}{k_{x,m}(x')} dx'}} \quad (\text{A.19})$$

See the forms of the stationary phase integral provided by Porter (1994) for a similar result.

The final adiabatic stress-displacement vector can be written as,

$$\vec{U}(x, 0, z) = \frac{i}{\sqrt{8\pi}} e^{-i\frac{\pi}{4}} \sum_m \frac{C_m(0, z_s) \vec{U}_m(x, z) e^{i \int_0^x k_{x,m}(x') dx'}}{\sqrt{k_{x,m}(0) k_{x,m}(x) \int_0^x \frac{1}{k_{x,m}(x')} dx'}} \quad (\text{A.20})$$

This form in Equation (A.20) is almost identical to the plane geometry adiabatic integral proposed by Porter (1994) and Godin (2003) for acoustic pressure, they differ by a multiplicative constant that defines the source strength. For acoustic waves, the stress-displacement vector reduces two terms, the pressure $P(x, 0, z)$ and a term proportional to the horizontal particle velocity, $\frac{1}{i\omega} v_x(x, 0, z)$ (Park & Odom, 1998). Since the adiabatic approximation only considers outgoing waves so a single term is only required, the pressure is a natural choice

$$\vec{U}(x, 0, z) \rightarrow P(x, 0, z). \quad (\text{A.21})$$

Therefore, the product $C_m(0, z_s) \vec{U}_m(x, z)$ should be proportional to the normalised pressure mode functions, i.e.

$$C_m(0, z_s) \vec{U}_m(x, z) \rightarrow C_s \bar{\varphi}_m(z_s) \bar{\varphi}_m(x, z) \quad (\text{A.22})$$

where C_s is a scaling factor. For acoustic propagation from an impulsive source C_s can conveniently be chosen as

$$C_s = \frac{4\pi}{\rho_s} \quad (\text{A.23})$$

which ensures a pressure amplitude of 1 Pa 1 metre from the centre of the source. Since this form of the adiabatic approximation assumes that the environment is translationally invariant in the y direction and that the source and receiver are chosen to lie in the plane where $y = 0$ the x coordinate can be interchanged with the r coordinate for cylindrical geometry (Jensen et al., 2011b) and the pressure can now be written as,

$$P(r, z) = \frac{\sqrt{2\pi} e^{i\frac{\pi}{4}}}{\rho_s} \sum_m \frac{\bar{\varphi}_m(0, z_s) \bar{\varphi}_m(r, z) e^{i \int_0^r k_{r,m}(r') dr'}}{\sqrt{k_{r,m}(0) k_{r,m}(r) \int_0^r \frac{1}{k_{r,m}(r')} dr'}}. \quad (\text{A.24})$$

Appendix B Acoustic Single-Scatter Mode Coupling Algorithm

An acoustic mode coupling algorithm was used in Chapter 5 to explain some differences in transmission loss between an adiabatic mode algorithm and a parabolic equation (PE) algorithm. This appendix outlines the coupling algorithm and provides some examples of its accuracy. The form of this coupling algorithm is an approximate single-scatter mode coupling method and follows very closely that of Porter et al. (1991). The mode shapes and wavenumbers were calculated by ORCA and were used to calculate the transmission loss and coupling coefficients; Tindle et al. (2000) as an example, have used ORCA in a similar way to investigate perturbation methods as applied to range dependent modelling.

The description of the algorithm begins with dividing the range dependent environment into local range independent sections. In the j^{th} segment the acoustic pressure, where the cylindrical spreading term has been removed, can be written as,

$$\hat{P}^j(r, z) = \sum_m (A_m^j H_{1,m}^j(r) + B_m^j H_{2,m}^j(r)) \bar{\varphi}_m^j(z) \quad (\text{B.1})$$

where $\bar{\varphi}_m^j(z)$ are local mode functions, A_m^j and B_m^j are amplitudes in the j^{th} segment that are to be determined through mode coupling. The $H_{1,m}^j(r)$ and $H_{2,m}^j(r)$ terms correspond to the phase of a propagating plane wave and are defined as

$$H_{1,m}^j(r) = e^{ik_{r,m}^j(r-r^{j-1})} \quad (\text{B.2})$$

and

$$H_{2,m}^j(r) = e^{-ik_{r,m}^j(r-r^{j-1})}. \quad (\text{B.3})$$

These terms come from the asymptotic form of the Hankel functions, see (Evans, 1983) or Porter et al. (1991) for a further description.

The purpose of the coupling algorithm is to compute the unknown amplitude coefficients in each segment such that energy is conserved (at least to sufficient approximation) through the vertical plane that divides each segment. For fluid environments this requires the conservation of acoustic pressure and particle velocity through the vertical plane that separates each segment. For far-field propagation the coupling coefficients based on these boundary conditions are

$$C_{mn} = \int \frac{\varphi_m^{j+1}(z)\varphi_n^j(z)}{\rho^{j+1}(z)} dz \quad (\text{B.4})$$

for the conservation of acoustic pressure and

$$\hat{C}_{mn} = \frac{k_{r,n}^j}{k_{r,m}^{j+1}} \int \frac{\varphi_m^{j+1}(z)\varphi_n^j(z)}{\rho^j(z)} dz \quad (\text{B.5})$$

for the conservation of particle velocity.

The coupling coefficients together with the two boundary conditions and unknown amplitude give two recursive equations to determine the amplitudes of forward propagating and reflected waves from a one segment to segment. These can be written in a compact vector form as

$$\vec{A}^{j+1} + \vec{B}^{j+1} = \bar{C}^j(\mathbf{H}_1^j \vec{A}^j + \mathbf{H}_2^j \vec{B}^j) \quad (\text{B.6})$$

and

$$\vec{A}^{j+1} - \vec{B}^{j+1} = \hat{C}^j(\mathbf{H}_1^j \vec{A}^j + \mathbf{H}_2^j \vec{B}^j) \quad (\text{B.7})$$

If M corresponds to the number if modes in segment $j^{th} + 1$ and N corresponds to the number of modes in the j^{th} segment then \vec{A}^{j+1} and \vec{B}^{j+1} are column vectors of size M , \vec{A}^j and \vec{B}^j are column vector of size N , and \mathbf{H}_1^j and \mathbf{H}_2^j are $M \times N$ diagonal matrices with terms $H_{1,m}^j(r_j)$ and $H_{2,m}^j(r_j)$ respectively. The terms \bar{C}^j and \hat{C}^j correspond to matrices that are $M \times N$ in dimension, the entries of which correspond to coupling coefficients in Equation (B.4) and Equation (B.5). These two equations can be written in an even more compact matrix form

$$\begin{bmatrix} \vec{A}^{j+1} \\ \vec{B}^{j+1} \end{bmatrix} = \begin{bmatrix} \mathbf{C}_{11}^j & \mathbf{C}_{12}^j \\ \mathbf{C}_{21}^j & \mathbf{C}_{22}^j \end{bmatrix} \begin{bmatrix} \vec{A}^j \\ \vec{B}^j \end{bmatrix} \quad (\text{B.8})$$

the forms of \mathbf{C}_{11}^j , etc can be found in Evans (1983).

Now the single-scatter approximation is applied. By assuming that the influence of multiple back-scattered reflections is negligible \mathbf{B}^{j+1} is set to zero in this recursion, this produces the single-scatter approximation. By further assuming that the outgoing energy dominates, the forward propagating amplitude can be written as

$$\mathbf{A}^{j+1} \approx \mathbf{C}_{11}^j \mathbf{H}_1^j(r_j) \mathbf{A}^j \quad (\text{B.9})$$

which is the approximate single-scatter form where \mathbf{C}_{11}^j is given by,

$$\mathbf{C}_{11}^j = \frac{\bar{\mathbf{C}}^j + \hat{\mathbf{C}}^j}{2}. \quad (\text{B.10})$$

To evaluate the integrals in Equation (B.4) and Equation (B.5) in order to compute Equation (B.10) efficiently, trapezoid integration via matrix multiplication was used. This was also discussed by Porter et al. (1991). The matrices of the coupling coefficients, $\bar{\mathbf{C}}^j$ and $\hat{\mathbf{C}}^j$ can then be computed from

$$\bar{\mathbf{C}}^j = ((\mathbf{V}^{j+1})^T * \mathbf{U}^j) dz \quad (\text{B.11})$$

and

$$\hat{\mathbf{C}}^j = \mathbf{K}^j \circ ((\mathbf{U}^{j+1})^T * \mathbf{V}^j) dz \quad (\text{B.12})$$

where \mathbf{X}^T denotes the matrix transpose and the elements of \mathbf{V}^j , \mathbf{U}^j , and \mathbf{K}^j are

$$\begin{aligned} V_{z_i n}^j &= \frac{\varphi_n^j(z_i)}{\rho^j(z_i)} \\ U_{z_i n}^j &= \varphi_n^j(z_i). \\ K_{mn}^j &= \frac{k_{r,n}^j}{k_{r,m}^{j+1}} \end{aligned} \quad (\text{B.13})$$

where $*$ defines a matrix product and \circ defines element by element multiplication.

In the segment that contains the source the pressure with no cylindrical spreading is written as,

$$\hat{P}^1(r, z) = \sum_m \left(\frac{\bar{\varphi}_m^1(z_s) e^{ik_{r,m}^1(r)}}{\sqrt{k_{r,m}}} \right) \bar{\varphi}_m^1(z) \quad r \leq r^1 \quad (\text{B.14})$$

With the coupling coefficients from Equation (B.10) and mode function from ORCA, reduced pressure can be marched out in range using Equation (B.1), subject to the approximations discussed above. The acoustic pressure then can be calculated by multiply in the by a scaling term and dividing by \sqrt{r} to account for cylindrical spreading.

$$P(r, z) = \sqrt{\frac{2\pi}{r}} e^{-i\frac{\pi}{4}} \hat{P}(r, z). \quad (\text{B.15})$$

To test and validate this coupled mode algorithm the ASA's fluid wedge environment (Jensen & Ferla, 1990) was considered for benchmarking purposes. The parabolic equation model RAMGEO (Collins, 1993b) was used for comparison

and validation of the coupled mode method. The geoacoustic parameters and environment geometry are given in Table B1 and Table B2.

Table B.1: Geoacoustic properties for the ASA Fluid Wedge proposed by Jensen and Ferla (1990)

Layer Type	ρ (g/cm ³)	c_p (m/s)	α_p (dB/λ)
Water	1.0	1500	0.0
Sediment	1.5	1700	0.5

Table B.2: Propagation model parameters for two benchmark cases

Case	Frequency (Hz)	H (r = 0 km) (m)	H (r = 3.5 km) (m)	z_s (m)	z_{rx} (m)
UP	25.0 50.0 100.0	200.0	25.0	100.0	30.0
DOWN		50.0	225.0	25.0	30.0

The results of this benchmarking exercise are shown below in Figure B.1, B.2, and B.3. All these figures show an excellent agreement between the coupled mode transmission loss and the transmission loss from the acoustic PE for the different frequencies and receiver locations. Both models were run with a false bottom that consisted of a 15 wavelength layer with the same sediment parameters in Table B1, a 10 wavelength attenuating layer (10 dB/λ) on top of a pressure release surface.

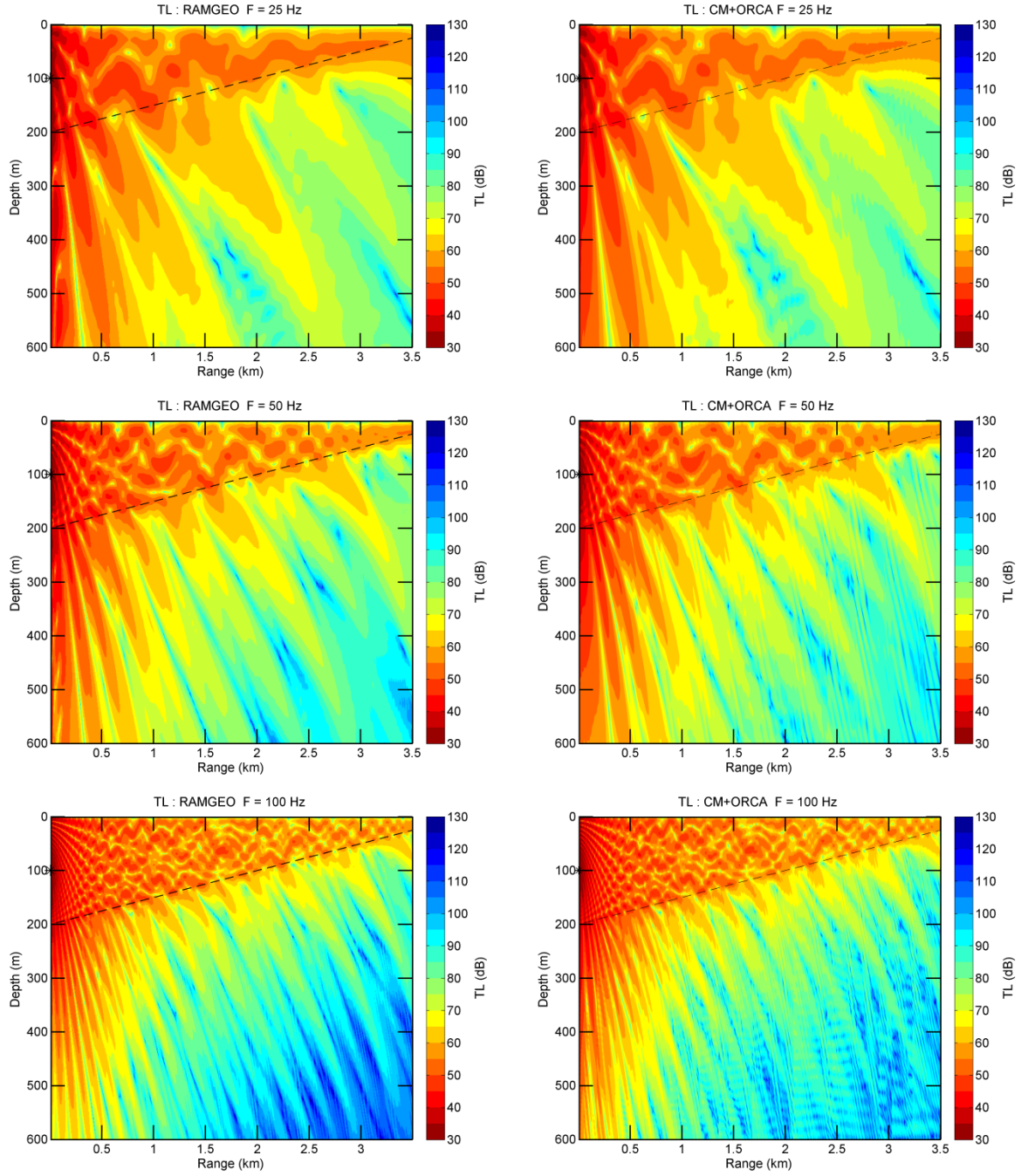


Figure B.1: TL for benchmark case ASA UP. *Left Panels:* TL at 25Hz, 50Hz, and 100Hz from RAMGEO. *Right Panels:* TL at 25Hz, 50Hz, ad 100Hz from ORCA with coupled modes

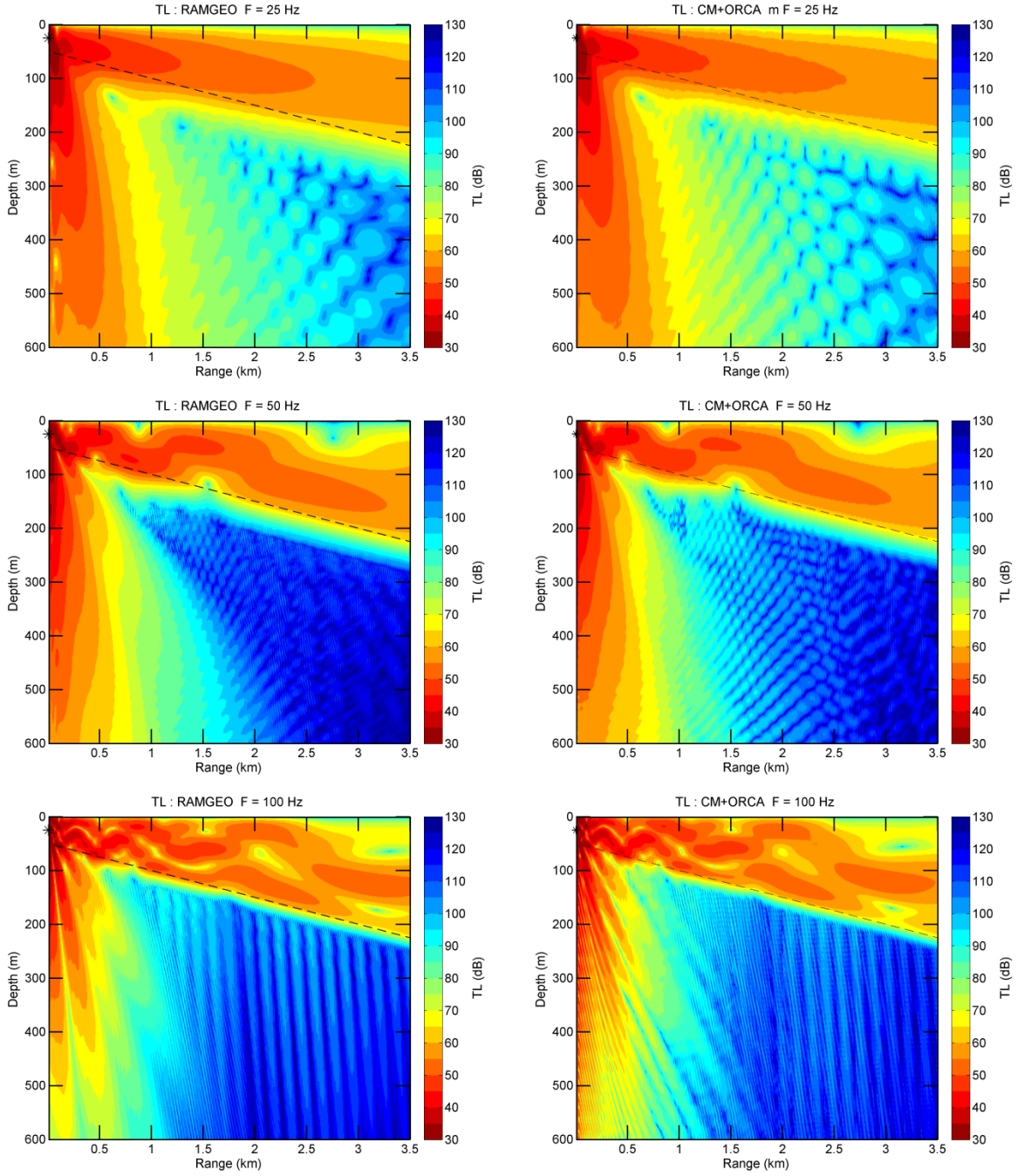


Figure B.2: TL for benchmark case ASA DOWN. *Left Panels:* TL at 25Hz, 50Hz, and 100Hz from RAMGEO. *Right Panels:* TL at 25Hz, 50Hz, and 100Hz from ORCA with coupled modes

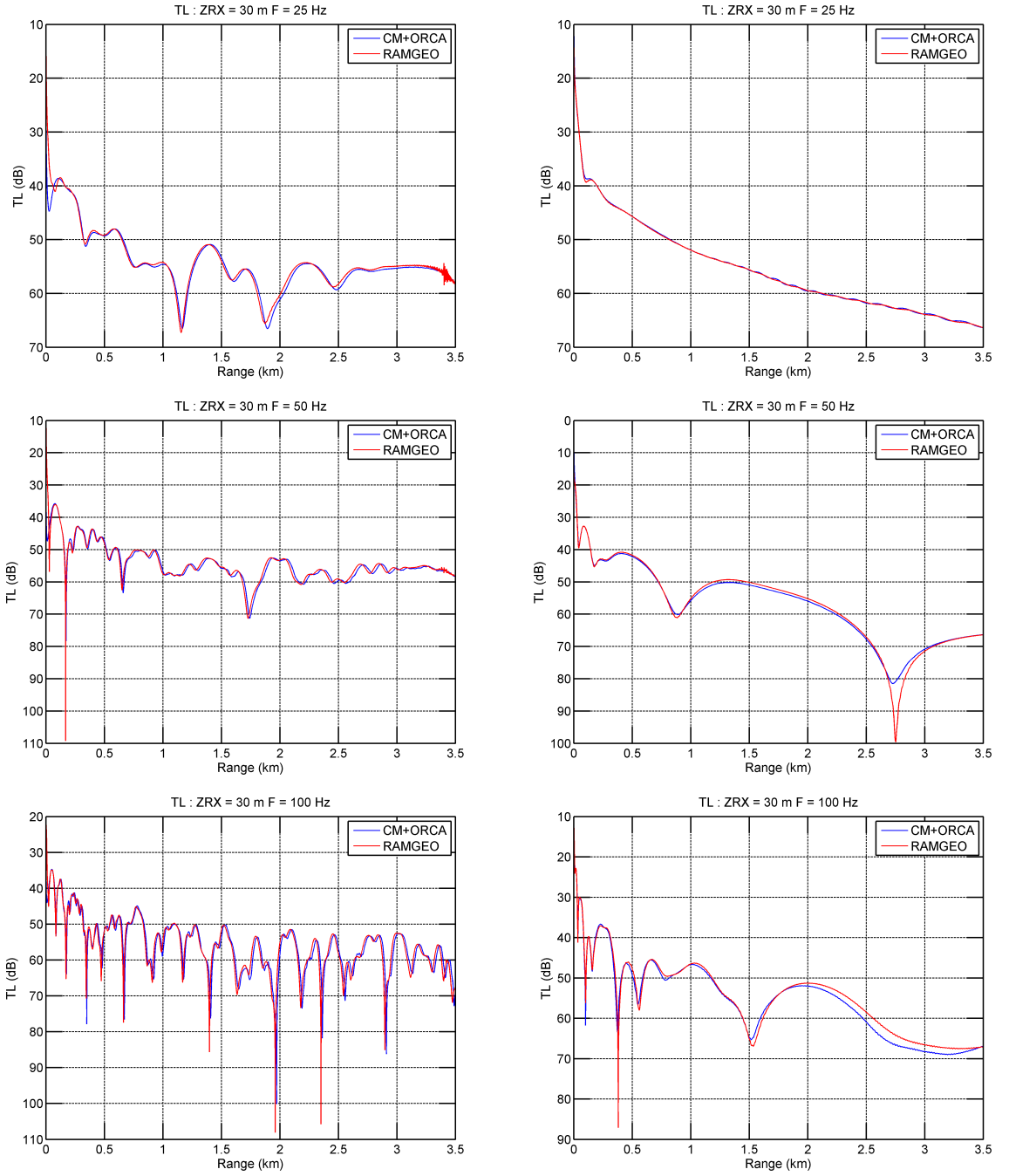


Figure B.3: Transmission loss (TL) slice at a receiver depth of 30 metres for the upslope and downslope validation scenarios *Left Panels:* TL at 25Hz, 50Hz, and 100Hz for the upslope scenario from ORCA with coupled modes (blue curve) and RAMGEO (red curve). *Right Panels:* TL at 25Hz, 50Hz, and 100Hz for downslope scenario from ORCA with coupled modes (blue curve) and RAMGEO (red curve).